I. Applications of Double-Exposure Holography to the Measurement of In Situ Stress and the Elastic Moduli of Rock from Boreholes

II. Shock Temperature Measurements in Fused Quartz and Crystalline NaCl to 35 GPa

Thesis by
Douglas Ray Schmitt

In Partial Fulfillment of the Requirements
for the Degree of
Doctor of Philosophy

California Institute of Technology
Pasadena, California

1987

(submitted May 22, 1987)

To my wife Cheryl,

and

my parents Jean and Ray.

ACKNOWLEDGEMENTS

I would like to thank Thomas J. Ahrens for his support and guidance during my graduate student carreer at Caltech and for giving me the freedom to make a few of my own mistakes along the way. I also worked closely with Jay Bass and Cathy Smither on the holographic *in situ* stressmeter and with Bob Svendsen on the measurement of shock temperatures in minerals; I found these collaborations to be productive and rewarding.

I would also like to thank my wife, Cheryl Schmitt, for her continued support and patience during our stay in Pasadena and for her help in the production of this thesis. Others which helped me immensely to finish the thesis in time for graduation are Lucianna Astiz, John Louie, Pat Scanlon, and Bob Svendsen.

I was fortunate to have the office mates in room 364 of Ed Garnero, Olafur Gudmundsson, Thomas Hearn, John Louie, Ronan LeBras, and Mark Richards; I thank them for their support and especially for their good humour. Mark Boslough, Steve Cohn, Terry Wallace, Marius Vassiliou, and Marianne Walck gave much early aid and encouragement. Association with Jim Tyburczy, Greg Miller, John Smith, Sally Rigden, William Anderson, Phil Ihinger, George Rossman, James Westphal, and Manfred Lange has been particularly instructive. Much thanks goes to Tom Nolan and Brigette Jensen for assistance with the holographic stressmeter in the Mojave Desert (in August) and in Colorado (in January).

This work would not have been possible without the technical aid of Epapradito Gelle, Mike Long, Chuck Manning (whose coffee-break saxaphone playing added some class to the sub-basement), Leon Young, Bill Barber,

Wayne Miller, Gunther Haehn, Bob Taylor, Dave Osborne, Richard Wickes, and Bart Pelsue. Sue Yamada must also be acknowledged for her tireless patience in keeping track of most of the details of the shock wave laboratory.

I would also thank Chris Brennan, Master of Student Houses, and the undergraduates of Page House at Caltech for definately giving me something other than my research to worry about. Cheryl and I have many happy memories and new friends from our four years of living with the Caltech undergraduates (DEI-FEIF).

I thank Dave Hemmings for getting me my first job as a Geophysicist at Texaco Canada Resources Ltd. and for getting me interested in geophysics. I also thank Joe Rood, Arvid Schultz, Sam Kounousu, and Jim O'Shea at the University of Lethbridge for having enough faith in me to encourage me to attend graduate school.

I sincerely appreciate the financial support of this research by the Department of Energy, the National Science Foundation, Sun Oil Corporation, and Schlumberger Technology Corporation. I would also like to thank the People of Alberta for awarding me the Sir James Lougheed Fellowship for part of my tenure at Caltech.

ABSTRACT

Part I.

The application of a new borehole technique using holographic interferometry to measure the in situ state of stress and the modulus of elasticity of rock is discussed. The apparatus exposes two holograms which are taken both before and after micron scale displacements are induced by (1) drilling a small stress-relieving hole in the wall of a borehole, and (2) applying a normal point force to the borehole wall. Maximum induced displacements are approximately 10 microns; the holograms are sensitive to movements on the order of 0.1 micron. Raw data take the form of a series interference holograms which have dark fringes superimposed on the three dimensional holographic borehole wall image. Synthetic fringe patterns are used to forward model the observed in the present method of data analysis. Calibrations of the normal force method of measuring the elastic moduli is carried out on metals with well defined elastic properties. Typically each test yields elastic (Young's) moduli for brass and aluminum of 100 $\pm$ 10 GPa and 70 $\pm$ 5 GPa, respectively, which are in close agreement with standard tests. Laboratory holographic measurements of the Young's modulus on a sample of keragenaceous dolomitic marlstone (taken from the same mine as which the in situ experiments were conducted) yielded 16.8 $\pm$ 2.8 GPa in agreement with the predicted modulus of 17.2 $\pm$ 2.0 GPa based upon published density-modulus relationships. Sonic velocity determinations of the dynamic Young's modulus on cores taken from the rock sample give values consistent with the holographic measurements of 13.5 to 19.1 GPa for assumed

values of Poisson's ratio of 0.35 to 0.25. The results of field tests in a horizontal borehole in a mine pillar in the Mahogany formation of Garfield County, Colorado, are presented for both experiments. The elastic modulus was found to vary with position in the borehole from 26.9 to 36.0 GPa. The farfield stresses for a borehole station 4 m from the mine pillar free surface were found from analysis of several stress-relief holograms; the determined vertical stress within the mine pillar was -10.2 MPa (compressive) close to the predicted magnitude of -11.2 MPa.

Part II.

Greybody temperatures and emittances of fused quartz under shock compression between 10 and 30 GPa are determined. Observed radiative temperatures are higher than computed continuum temperatures for shock compressed fused quartz, however; below $\sim$ 26 GPa observed emittances are $<$ 0.02. This suggests that fused quartz deforms heterogeneously in this shock pressure range, as has been observed in other minerals. Between 10 and 16 GPa, radiative temperatures decrease from 4400 K to 3200 K, above 16 GPa to 30 GPa greybody temperatures of $\sim$ 3000 K with low emittances are observed. The emittances increase with pressure from 0.02 to 0.9. The pressure range from 10 to 16 GPa coincides with the permanent densification region while the 16 to 30 GPa range coincides with the mixed phase region along the fused quartz Hugoniot. The differing radiative behaviors relate to these modes of deformation. Based upon shock recovery experiments and a proposed model of heterogeneous deformation under shock compression, the temperatures associated with low emittances in the

mixed phase region probably represents the melting temperature of the high pressure phase. Above 20 GPa to 30 GPa the melting temperature of stishovite would therefore be approximately 3000 K and almost independent of pressure. The effect of pressure on melting relations for the phase system SiO_2-Mg_2SiO_4 are considered together with the proposed melting curve of stishovite and suggest that maximum solidus temperatures within the mantle of $\sim$ 2370 K at 12.5 GPa and $\sim$ 2520 K at 20.0 GPa. Using the proposed stishovite melting temperatures (T_m) and reasonable upper mantle temperatures (T), the effective viscosity (which is a function of the homologous temperature (T_m / T)) appears to remain nearly constant from 600 to 200 km depth in the Earth.

Radiative color temperatures were measured in single crystal sodium chloride under shock compression parallel to [100] over a pressure range from 20 to 35 GPa. Color temperatures from 2500 to 4500 K and emittances from 0.003 to 0.3 were determined by fitting observed spectra (450 to 850 nm) to the Planck greybody radiation law. These data support a heterogeneous shock deformation model of shocked halite in this pressure range. A 2500 K temperature rise is observed over the B1-B2 mixed phase region from 25 to 30 GPa. Assuming that shock deformation occurs via yielding in localized planar zones which become melt and the melting temperature at high pressure controls the temperature, we infer that the temperature of the B2 fusion curve from 30 to 35 GPa rises from 3200 to 3300 K. The B1-B2-liquid triple point is predicted at a temperature of 2250 K and 23.5 GPa.

Table of Contents

Part II: Shock Temperature Measurements in Fused Quartz and Crystalline NaCl to 35 GPa

Chapter 2: Shock Temperatures in Fused Silica

Chapter 3: Shock Induced Melting and Microfracturing in Single Crystal NaCl

Introduction

The research presented in this thesis is concerned with two different experimental problems, one dealing with the state of stress in the crust of the Earth and the other with the properties of minerals at high temperatures and pressures. At first glance these subjects appear unrelated, and for practical purposes they are. However, in the big picture, crustal stresses, especially in tectonically active regions of the Earth, are a manifestation of dynamic processes occurring at depth within the mantle. Thus, better understanding of one problem aids in constraint of the other.

The first topic is the application of double-exposure holography to the measurement of the in situ state of stress in the Earth. As the holographic *in situ* stressmeter is a developmental project, the present study builds on the earlier work of Bass et al., (1986), Schmitt et al., (1986a), Schmitt et al., (1986b), and Smither et al., (1987).

Optical holograms have been popularized by their ability to recreate three-dimensional images. A double-exposure hologram is created on a single piece of film by taking a holographic exposure of an object (in our case a portion of the borehole wall is the object) and then taking a second exposure after the surface of the object has been displaced or deformed. Interference of the two holograms records the object displacement field, the data appear as a series of dark fringes superimposed upon the three-dimensional holographic image. Here, we exploit the process of double-exposure holography to record either a stress-relief induced or a known normal point force induced displacement field on the borehole wall for the determination of the *in situ* borehole wall stresses and elastic moduli. Since stress measurements which rely on

stress-relief displacements are dependent on the *in situ* elastic moduli, the two experiments are complementary, especially when it is noted that the displacements induced are similar for both.

Although the concept behind double-exposure holograms is simple in principle, application of the holographic technique in a borehole is technically difficult. A high degree of stability must be maintained to create a double exposure hologram. Any displacements of the optics between the two holographic exposures appears as translational fringes in the final holographic image and is considered noise in the data. These additional fringes must be accounted for in any data analysis.

The present data analysis relied upon a spatial forward modelling of the observed fringe patterns which are dependent upon the magnitude and direction of the induced displacements on the borehole wall.

New results presented in this study include a measurement of the complete stress tensor from several holograms at a single depth within a horizontal borehole in an oil shale mine pillar in Garfield County, Colorado. The *in situ* modulus of elasticity was also measured at four locations within the same borehole. Laboratory calibrations of the normal point force method of elastic modulus determination were conducted on metals with well-known elastic properties and show that the technique, with the forward modelling data analysis, may successfully measure the modulus of elasticity of a material despite large translational displacements.

Shock temperature measurements in fused silica and crystalline NaCl at shock pressures below 35 GPa are reported in the second part of the thesis. The present studies have a higher resolution of pressure than the earlier

exploratory work of Kondo and Ahrens (1983), Schmitt and Ahrens (1983) and Schmitt et al., (1986c). Temperatures much higher than those expected for a shocked continuum are observed and are indicative of heterogeneous deformation of these materials under shock compression. The new results are particularly interesting in that near a the B1-B2 phase transition in NaCl and the fused quartz to stishovite phase transition the shock temperatures increase by as much as 2000 K and decrease past the phase transitions. These anomalous results may be related to an effective activation energy for the phase transition on the time scale of the rise of the shock. Additionally, a model of heterogeneous deformation explaining many features of shock compression in brittle material (e.g., existence of glass in shock recovered crystals and the loss of strength above the Hugoniot elastic limit) is proposed. The model suggests that the observed temperatures may be those of the melting curve of silica and NaCl with pressure.

References

Bass, J., Schmitt, D.R., and Ahrens, T.J., Holographic In Situ Stress Measurements, *Geophys. J. R. astr. Soc.*, **85**, pp. 13-41, 1986.

Kondo, K. and Ahrens, T.J., Heterogeneous Shock Induced Thermal Radiation in Minerals, *Phys.Chem.Minerals*, **9**, pp. 173-181, 1983.

Schmitt, D.R., Smither, C.L., Ahrens, T.J. and Jensen, B.L., Holographic Measurements of Elastic Moduli, *Proc. 27th U.S. Symp. on Rock Mechanics, The University of Alabama, Tuscaloosa*, pp. 185-191, 1986a.

Schmitt, D.R., Smither, C.L., Ahrens, T.J. and Jensen, B.L., Borehole *In-situ* Holographic Stress and Elastic Moduli Measurements, *Proc., The Society*

of Exploration Geophysicists, 56th Annual Meeting, Houston, pp. 9-12, 1986b.

Schmitt, D.R., Svendsen, B., and Ahrens, T.J., Shock Induced Radiation from Minerals, in *Shock Wave in Condensed Matter*, ed. Y.M. Gupta, pp. 261-265, 1986c.

Schmitt, D.R. and Ahrens, T.J., Temperatures of Shock Induced Shear Instabilities and Their Relationship to Fusion Curves, *Geoph.Res. Lett.*, **10**, pp. 1077-1080, 1983.

Smither, C., Schmitt, D.R., Ahrens, T.J., Analysis and Modelling of Holographic Measurements of In Situ Stress, Submitted to *Int.J.Rock. Mech.Min.Sci.*, 1987.

Chapter 1.

IN SITU HOLOGRAPHIC ELASTIC MODULI AND STRESS MEASUREMENTS FROM BOREHOLES

ABSTRACT

The application of a new borehole technique using holographic interferometry to measure the *in situ* state of stress and the modulus of elasticity of rock is discussed. The apparatus exposes two holograms which are taken both before and after micron scale displacements are induced by (1) drilling a small stress-relieving hole in the wall of a borehole, and (2) applying a normal point force to the borehole wall. Maximum induced displacements are approximately 10 microns; the holograms are sensitive to movements on the order of 0.1 micron. Raw data take the form of a series interference holograms which have dark fringes superimposed on the three-dimensional holographic borehole wall image. Synthetic fringe patterns are used to forward model the observed in the present method of data analysis. Calibrations of the normal force method of measuring the elastic moduli is carried out on metals with well-defined elastic properties. Typically each test yields elastic (Young's) moduli for brass and aluminum of 100 $\pm$ 10 GPa and 70 $\pm$ 5 GPa, respectively, which are in close agreement with standard tests. Laboratory holographic measurements of the Young's modulus on a sample of keragenaceous dolomitic marlstone (taken from the same mine as which the *in situ* experiments were conducted) yielded 16.8 $\pm$ 2.8 GPa in agreement with the predicted modulus of 17.2 $\pm$ 2.0 GPa based upon

published density-modulus relationships. Sonic velocity determinations of the dynamic Young's modulus on cores taken from the rock sample give values, consistent with the holographic measurements, of 13.5 to 19.1 GPa for assumed values of Poisson's ratio fo 0.35 to 0.25. The results of field tests in a horizontal borehole in a mine pillar in the Mahogany formation of Garfield County, Colorado, are presented for both experiments. The Young's modulus was found to vary with position in the borehole from 26.9 to 36.0 GPa. The farfield stresses for a borehole station 4 m from the mine pillar free surface were found from analysis of several stress-relief holograms; the determined vertical stress within the mine pillar was -10.2 MPa (compressive) close to the predicted magnitude of -11.2 MPa.

INTRODUCTION

Knowledge of the state of stress in the Earth is an essential component of the solution to many geotechnical and geophysical problems. Stresses within the Earth affect underground repository design and safe mine construction. The in situ stresses present in the lithosphere constrain the plate tectonic driving forces. Application of the hydrofracture technique to stimulate petroleum and geothermal energy recovery requires knowledge of the orientation and magnitude of the principal stresses (Haimson and Fairhurst (1967), Hubbert and Willis (1957)). Moreover, it has recently been recognized how in situ stress controls seismic anisotropy of rock due to preferential orientation of microfracture opening (Thomsen (1986), Crampin et al., (1978, 1980), Nur (1971), Stesky (1985)).

The objective of the our research is to determine the state of stress in the Earth from a borehole. However, the borehole concentrates regional stresses, additionally the stressmeter observes only the surface of the borehole wall. Therefore, to find the farfield ($\sim$ 10 times the borehole radius away) stress tensor at a given station within the borehole, the three nontrivial borehole wall stresses: $\sigma_{\theta\theta}$, σ_{hh}, and $\tau_{\theta h}$ (see figure 14) must be determined at at least three independent azimuths within the borehole (Hiramatsu and Oka (1962), Leeman and Hayes (1966), Cohn (1982), Bass et al., (1986)).

We have previously described the holographic *in situ* stressmeter (Bass et al., (1986)) and the methodology of reducing interference holograms taken in different orientations (Smither et al., (1987)). The present paper is concerned with measurement of the six components of the stress tensor and the *in situ* elastic (Young's) modulus: E.

The present stressmeter is capable of conducting two separate experiments, both necessary for determination of the *in situ* stress, from an uncased clean borehole. In the first experiment, a known normal point force applied to the borehole wall rock induces a displacement field which is proportional to E. A small hole is drilled into the borehole wall to locally produce stress-relief displacements dependent upon the *in situ* stresses for the second experiment. The feasibility of using double exposure holography to measure stresses has recently been independently confirmed in the engineering community (Nelson and McCrickerd (1987)). Since stress determinations via a stress relief methods are critically dependent upon accurate knowledge of the elastic moduli, the two experiments are complementary.

The value of performing both experiments with the holographic technique is further reinforced by the fact that induced point force and stress-relief displacements and strains are similar. The double-exposure holograms are capable of resolving displacements as small as 0.1 microns or approximately 1/6 the wavelength of the laser radiation used. Calibration of the optics module with known translational displacements have been previously discussed (Bass et al., (1986)). Maximum displacement magnitudes for both experiments are $<$ 10 microns and strains encountered are approximately 100 microstrains measured over a 10 cm square region. In contrast, conventional *in situ* static elastic modulus testing methods - compression tests, plate bearing tests, flat jack tests, dilatometer tests, and the N-X borehole jack tests (Bieniawski (1978), Jaeger (1979)) - measure the rock elastic moduli on varying length scales, force levels, and strain magnitudes. For example, the N-X borehole jack applies up to 700 KNewtons of force via 20.3 cm long platens to a 7.62 cm diameter borehole (Goodman, Van, and Heuze (1970)) producing typical displacements of 0.2 mm (Meyer and McVey (1974)) with strain magnitudes near 1 mstrain. Forces up to 11.8 MNewtons are applied to areas on the order of 1 m^2 in the plate bearing experiment, displacements up to 2.5 mm and strains of 1 mstrain are induced (Jeager (1979)).

Although the measured rock modulus is affected by the scale of the experiment and the density of discontinuities in the rock mass (Bieniawski and Van Heerden (1975)), the holographic elastic modulus test, which supplies small scale values of E, would also benefit other stress measurement techniques such as the the C.S.I.R. doorstopper cell (Leeman (1969)), the

triaxial strain cell (Leeman and Hayes (1966)), the direct strain gauge technique (Swolfs, Handin, and Pratt (1974)), and the borehole slotter stressmeter (Bock et al., (1984)).

Although application of normal forces and stress-relief by drilling have been used previously, the present application with double exposure holography is new. The blind-hole drilling technique (Rendler and Vigness (1966)) uses strain gauges to measure residual stresses in metal machinery components. The plate bearing method of determining elastic moduli in rock (Jeager and Cook (1979)) shares an identical theoretical basis with the present method. The present raw data consists of a series of dark interference fringes superimposed upon the reconstructed image of the borehole wall. The fringe pattern depends uniquely on the magnitudes and directions of the induced displacement fields which in turn are dependent on the *in situ* stresses and rock elastic moduli.

In the present paper, the theory behind the holographic measurements and the forward modelling of the data, with particular emphasis on the normal force experiment, are outlined. The results of laboratory normal force experiments on brass and aluminum alloys, as well as a sample of dolomitic marlstone (oil shale) taken from the Mahogany formation, Garfield County, Colorado, are discussed. Results of recent *in situ* deployment of the stressmeter in a borehole in a mine pillar of the dolomitic marlstone for both the normal force and stress-relief experiments are also presented.

--

DOUBLE EXPOSURE HOLOGRAPHY

Double-exposure holography (Vest (1979), Schumann and Dubas (1979), Jones and Wykes (1983)) is an optical interferometric technique to record a three-dimensional displacement field which occurs between two holographic exposures of a single emulsion. The off-axis holograms are created with monochromatic laser radiation (figure 1) and produce the characteristic three- dimensional effect when viewed (Leith and Upatnieks (1962,1964)). A double-exposure hologram is, in effect, two off-axis holograms on the same film. It is produced by first taking a holographic exposure of an object, then translating or deforming the surface of the object, and taking a second holographic exposure. In the present experiments, a portion of the borehole wall surface (approximately 10 cm square) is the object; the displacements induced by force application (figure 1) or drilling (figure 2) occur between two exposures of the film. The result is a three-dimensional image of the borehole wall with a superimposed fringe pattern (figure 3).

An optical hologram is a diffraction pattern produced by the interference of a reference beam and light nonspecularly reflected from the object, referred to as an object beam, within the emulsion of the holographic film (figure 1). Reconstruction of the hologram occurs when a replica of the reference beam is passed through the hologram to diffract and recreate the object beam. In this way both the amplitude and the phase of the original object wavefield are reproduced, resulting in the three dimensional image. Within a double exposure hologram, two slightly different object wavefields are reconstructed which in turn interfere to

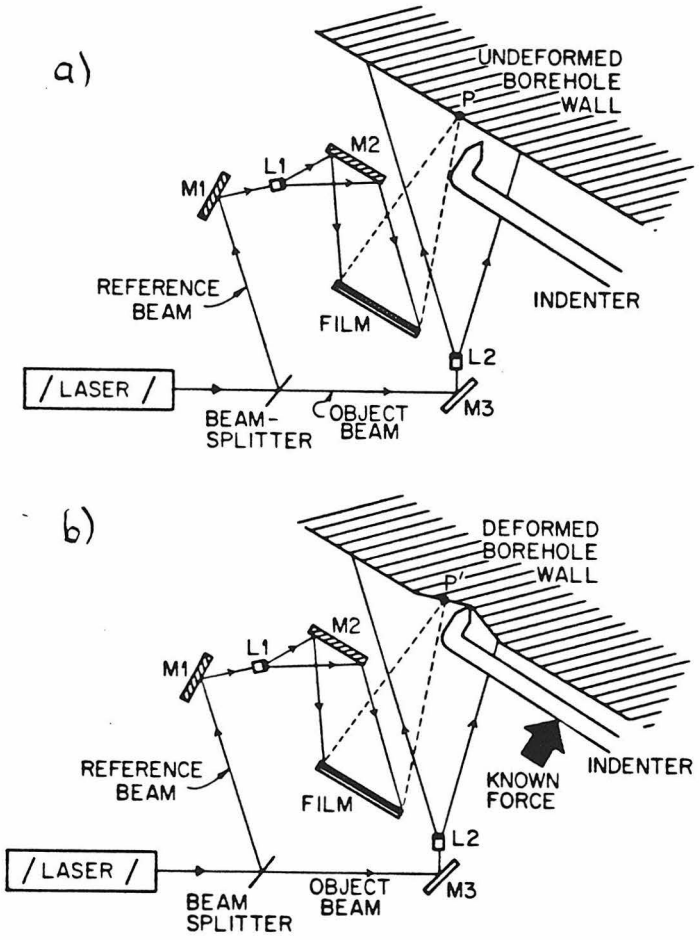

Figure 1). Method of Producing a Double Exposure Hologram for Elastic Modulus Measurement Experiment. To create an off-axis hologram, monochromatic laser radiation is separated into two paths by a beam splitter. The reference beam is diverted by mirrors M1 and M2 and expanded by lens L1 to illuminate only the film emulsion. The object beam is diverted by mirror M3 and expanded by lens L2 to illuminate the borehole wall which scatters the light back to the film. The object and reference beams interfere in the emulsion and produce a diffraction pattern which is the hologram. **1a)** Schematic of elastic moduli experiment during first holgrphic exposure, P is a point on the borehole wall within the field of view of the hologram. **1b)** Known force is applied by the steel indenter to the borehole wall and induces a three dimensional displacement field, P' represents the new displaced position of P. While the displacement field is maintained, the second exposure is taken on the same film.

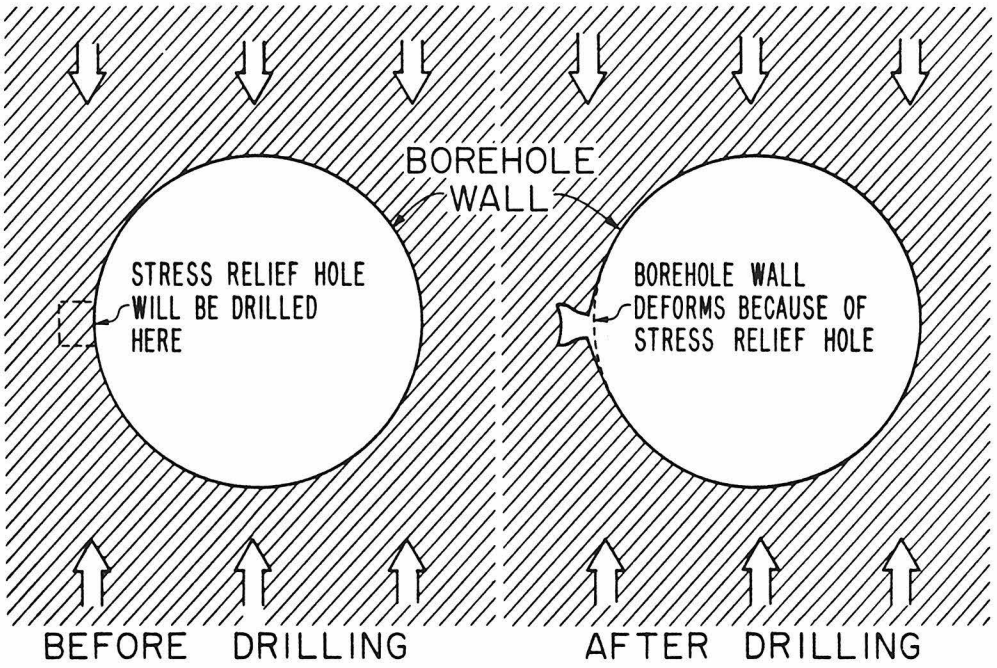

Figure 2). Plan view of borehole and displacement field induced by drilling of stress-relief hole in borehole wall for stress measurement experiment. Holographic exposures are taken before and after drilling record the three-dimensional displacement field.

Figure 3). Example of a Stress-Relief Double Exposure Hologram. Stress relief hole is seen near center of photograph. Long, subparallel fringes across photograph are due to translations of the optics module between holographic exposures. Rounded, semicircular fringes near drilled hole are from the induced stress-relief displacements and are the data for this experiment. Source of laser radiation (S) is to left of photograph, bottom of photograph is towards the South, and hologram taken at $\theta = +225$ deg (figure 14c). Matching forward modelled fringe pattern is #4 of figure 26.

produce the displacement dependent fringe patterns.

A fringe on a double-exposure holographic image occurs when a ray of light from the first exposure (S-P-H) with (figure 4) and its corresponding ray from the second exposure (S-P'-H) are out of phase by an odd number of half wavelengths of the monochromatic light used to make the holograms. Thus, in addition to the displacement (L) between exposures, the existence of a fringe at a given point on the object is also dependent upon the relative positions of the object beam source (S), the point on the object beneath the fringe (P to P'), and the point on the holographic emulsion (H) from which the image is viewed (figure 4) and represented by the position vectors: R ,r_1, and r_3 as illustrated in figure 4. The wave vectors k_1, k_2, k_3, and k_4 have magnitude of $2\pi/\lambda$; the projection of a wave vector upon its corresponding position vector yields the phase of the light when it arrives at the end of the position vector. The phases of the light reaching H after being reflected from P for the first exposure and P' for the second exposure are given by (Sollid (1969a, 1969b), Vest (1978)):

$$(1)\quad \Phi = k_1 \cdot r_1 + k_2 \cdot (R - r_1)$$

and

$$(2)\quad \Phi' = k_3 \cdot r_3 + k_4 \cdot (R - r_3).$$

The phase difference: $\delta = \Phi' - \Phi$, between the ray paths for the first and second exposures may then be given as

$$(3)\quad \delta = (k_2 - k_1) \cdot (r_1 - r_3) + \Delta k_1 \cdot r_3 + \Delta k_2 \cdot (R - r_3)$$

where $\Delta k_1 = k_3 - k_1$ and $\Delta k_2 = k_4 - k_2$. Note the displacement occurring between the exposures in the movement of P to P' is given by

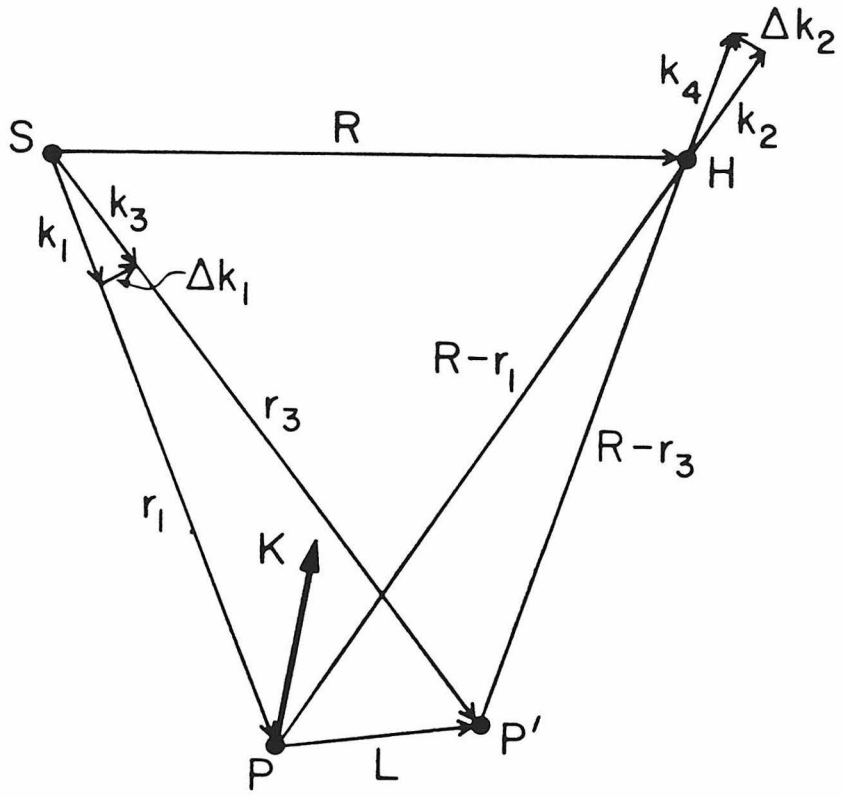

Figure 4). Ray Path Diagram Illustrating Double Exposure Process. Object beam laser light propagates from the source point (S) to a point (P) on the borehole wall and is reflected to a point on the holographic emulsion (H) for the first exposure. The point P is displaced to P' a distance given by L and the second exposure with the new ray path: S-P'-H, is taken. R, r_1, and r_3 are the distances as defined in the figure. The ray propagation vectors, of magnitude $2\pi/\lambda$, are k_1,k_2, k_3, and k_4. $K = (k_2 - k_1)$ is the sensitivity vector. A dark fringe is produced when the light propagating along the S-P-H ray path and the light along the S-P'-H ray path destructively interfere. The magnitude of L is on the order of microns in contrast to r_1 and r_3 which are several cm allowing the approximation of equation (4) to be valid (Sollid (1969a.1969b)).

$L = r_1 - r_3$ (figure 4) with a magnitude of microns in contrast to the several centimeter magnitudes of the postion vectors. As a result, the vectors $(k_3 - k_1)$ and $(k_4 - k_2)$ are nearly perpendicular to the position vectors r_3 and $(R - r_3)$, respectively, and their projection upon the position vectors vanish to simplify equation (3) to:

$$(4) \quad \delta = (k_2 - k_1) \cdot L.$$

A dark fringe order: N is thus given by:

$$(5) \quad N = 1/2(\frac{\delta}{\pi} - 1)$$

and a dark fringe exists when N is any integer.

To reconstruct holograms for purposes of data analysis, the two dimensional real image is created by propagating a laser beam through the developed emulsion (figure 5). The advantages of this technique are twofold. The position on the hologram (H) (figure 4) from which the image is reconstructed, necessary for determining ray paths during data analysis, is easily determined to an accuracy of $\pm$ 1.0 mm, and the diffracted real image may be directly projected onto sheet film with a minimum of spatial image distortion.

DATA ANALYSIS AND THEORY OF DISPLACEMENTS

FORWARD MODELLING PROCEDURE

In an ideal analysis of a double-exposure hologram, the observed fringe pattern is inverted to determine the three-dimensional displacement vector L for a given point P on the borehole wall. Rigorous methods require at least

--

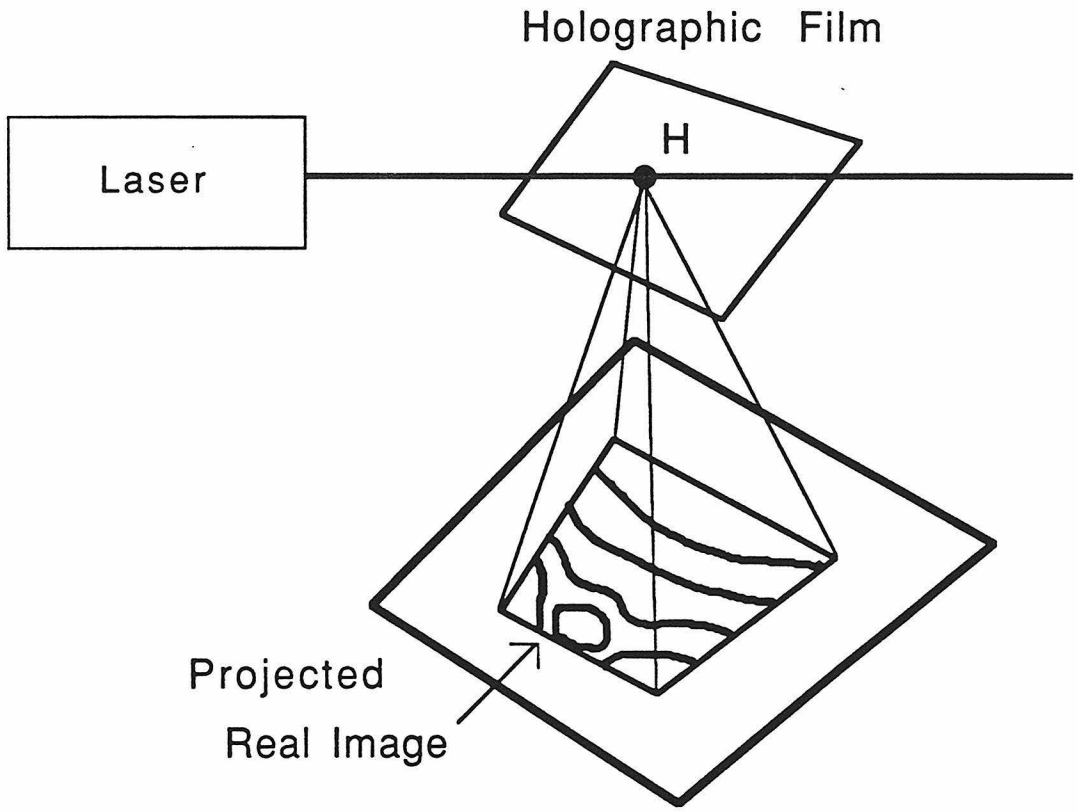

Figure 5). Two-dimensional reconstruction of real image in order to make photographs for analysis of fringe patterns. Laser beam propagates through film emulsion at hologram point H (figure 4), a portion of the beam

three observations of L, either from multiple holograms at different locations about an object (Ennos (1968)) or from several points on a single large hologram (Aleksandrov and Bonch-Bruevich (1967), Dhir and Sikora (1974)). This is due to the fact that, by equation 4, one observation of the fringe order for a given object point P yields only the component of the displacement vector L projected onto the sensitivity wavevector: $K = (k_2 - k_1)$ (Vest (1979)). Three phase measurements for an object point P: δ_1, δ_2, and δ_3 are therefore required to find the three independent components of L. Since the relative positions of the source point (S) and a defined object point (P) (figure 4) do not change, an independent sensitivity vector K demands that a new hologram point be selected (figure 6). k_1, $k_2{}^1$, $k_2{}^2$, and $k_2{}^3$ are the wave vectors of magnitude $2\pi/\lambda$ as shown, H_1, H_2, and H_3 are three separate points on the hologram, $K_1 = (k_2{}^1 - k_1)$, $K_2 = (k_2{}^2 - k_1)$, and $K_3 = (k_2{}^3 - k_1)$ are the sensitivity vectors for the independent ray paths $(S-P-H_1)$, $(S-P-H_2)$, and $(S-P-H_3)$, respectively. The unknown displacement vector L may then be determined by the system of equations of equation (4) (Vest (1979)):

$$(6a)\quad \delta_1 = K_1 \cdot L$$

$$(6b)\quad \delta_2 = K_2 \cdot L$$

$$(6c)\quad \delta_3 + K_3 \cdot L$$

since δ_1, δ_2, and δ_3 are found from the fringe pattern and K_1, K_2, and K_3 are known given the positions of S and P and H_1, H_2, and H_3, respectively. The displacement field of the object surface may thus be determined by finding the displacement vector L for a number of surface points P to the

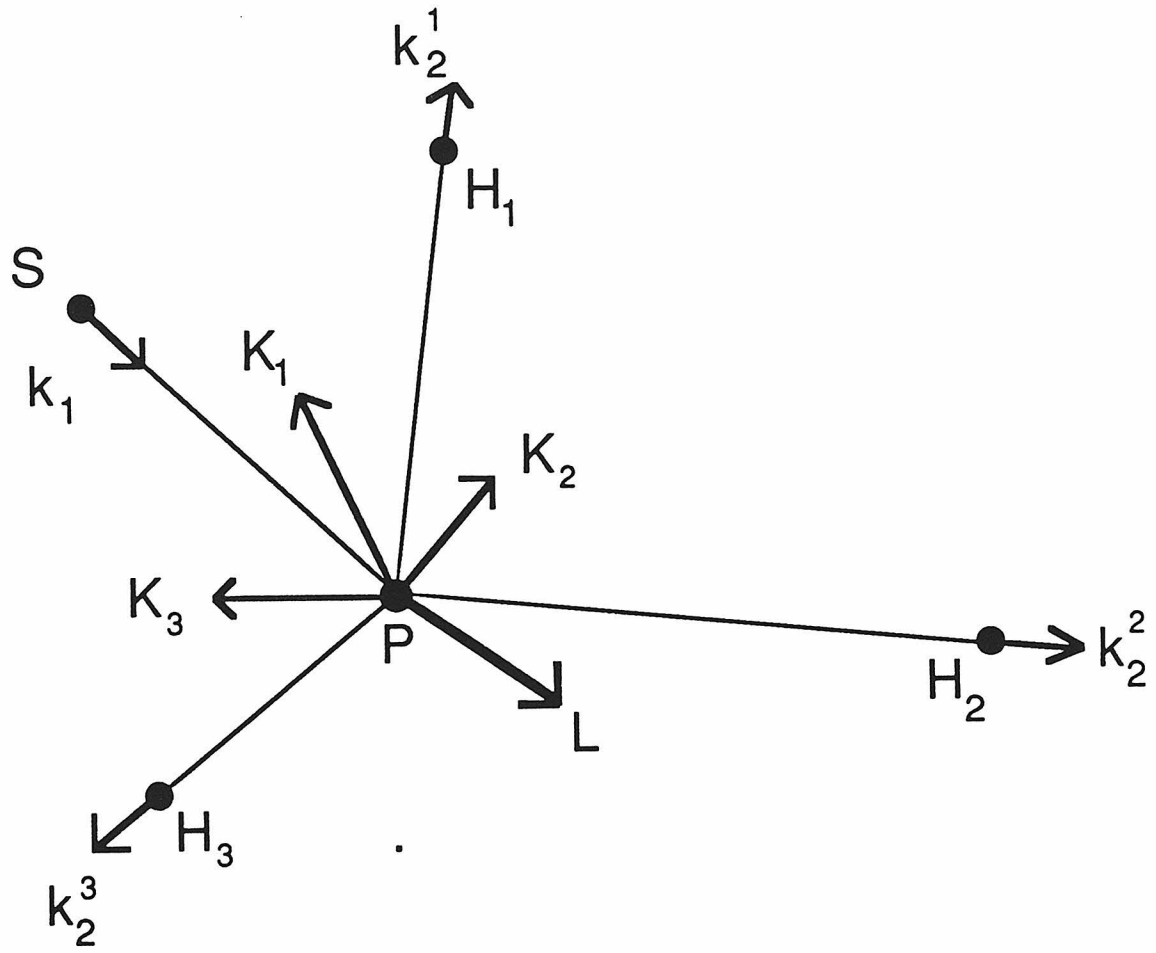

Figure 6). The use of three different hologram points to find the displacement vector L of point P between holographic exposures. See text for details.

desired spatial resolution.

The present experiments are conducted within the confines of a borehole; the luxury of multiple or large holograms for the determination of the borehole wall displacement field is not available due to experimental constraints. For these reasons, a forward modelling data analysis method has been developed. Instead of finding L for a number points on the borehole wall, the desired parameters (borehole wall stresses or elastic moduli) are input directly into an algorithm which computes a synthetic double-exposure fringe pattern. The unknown parameters are varied until the synthetic fringe pattern and the observed fringe pattern spatially match.

The first step of the forward modelling algorithm selects a grid of borehole wall object points (P_{ij}) with positions relative to a stressmeter instrumental cartesian co-ordinate system x, y, z (figure 7). Note that the x-z plane through the origin includes the source point (S) and is perpendicular to the borehole axis. The x-y plane and the y axis are tangent to the borehole wall and parallel to the borehole axis. For each point P_{ij} a displacement vector L_{ij} is found by:

$$(7) \quad L_{ij} = T + I_{ij}$$

where T is the optics module translational displacement vector (constant for all P_{ij}) and I_{ij} (dependent upon P_{ij}) is the induced (i.e., stress-relief or normal force) displacement vector discussed in more detail below. The sensitivity vector K_{ij} for the ray path $S-P_{ij}-H$ is then calculated and combined with L via equation (4) to find the phase difference δ_{ij}. The dark fringe order: N_{ij}, for the point P_{ij} is then found using the criteria for a dark fringe

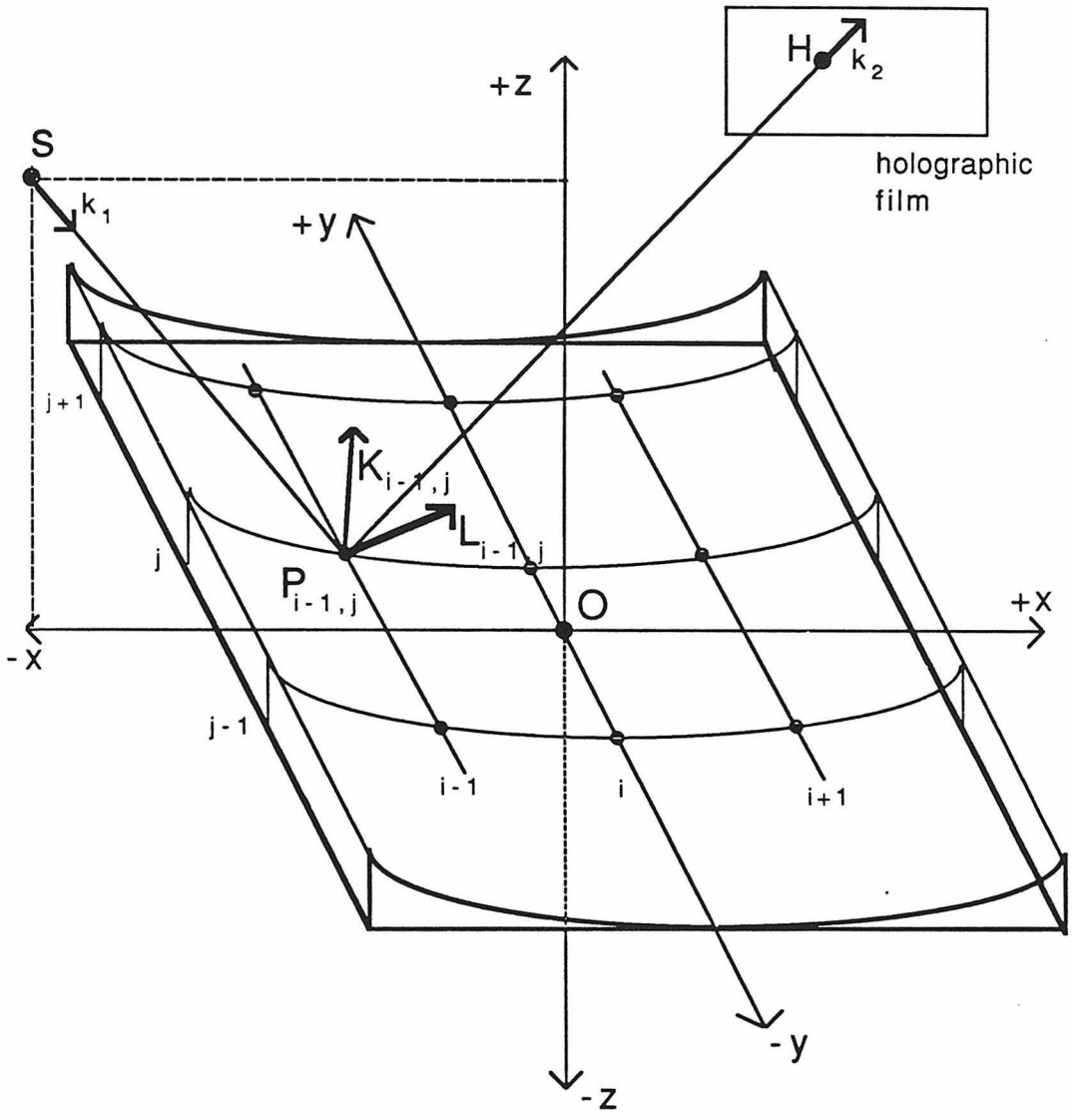

Figure 7). x-y-z co-ordinate system with respect to the borehole wall and source point S and hologram point H for purposes of calculating a forward modelled fringe pattern. O is origin of cartesian co-ordinate system x-y-z with the x-y plane tangent to the borehole and the x-z plane containing the source point S. In the forward modelling, for each grid point P_{ij} on the borehole wall a displacement vector L_{ij} and sensitivity vector K_{ij} are found, and when combined via equations 8 and 9 determine fringe existence at P_{ij}.

that the phase difference be a odd number of half wavelengths of the laser light used and, as in equation (5), expressed as:

$$(8)\quad N_{ij} = \frac{1}{2}\left[\frac{\delta_{ij}}{\pi} - 1\right]$$

Let M be an the closest integer to the real number N_{ij}, then the algorithm declares the existence of a dark fringe of order M at P_{ij} if:

$$(9)\quad |\, M - N_{ij} \,| < b$$

where b is the maximum dark fringe order limit and typically has a value of 0.15 determined upon the basis of experience with forward modelling of holograms. Upon declaration of a dark fringe, a black mark is plotted over the position on the synthetic fringe pattern corresponding to P_{ij}. Nothing is plotted if a dark fringe is not declared.

Input values to the algorithm are of two types: those premeasured and initialized during the forward modelling procedure and those varied in order to determine the desired parameters (Table 1).

ELASTIC MODULUS DISPLACEMENT MODEL

To find the induced displacements I_{ij} the elastic moduli measurement experiment relies upon the theory of surface displacements on an infinite, isotropic, elastic halfspace subjected to a normal point load: the Boussinesq problem given by (Timoshenko and Goodier (1970)):

$$(10)\quad U_{\varsigma} = \frac{F(1-\nu)}{\pi E \rho}$$

$$(11)\quad U_{\rho} = \frac{-F(1-2\nu)(1+\nu)}{2\pi E \rho}$$

Table 1) Initialized and Varied Parameters for Forward Modelling

	INITIALIZED	VARIED
Elastic Modulus Experiment	S = Source Position H = Hologram Position F = Applied Normal Force	E = Modulus of Elasticity ν = Poisson's Ratio T = Translational Displacements
Stress Measurement Experiment	S = Source Position H = Hologram Position a = Drilled Hole Radius t = Analytic Plate Thickness E = Modulus of Elasticity ν = Poisson's Ratio	$\sigma_{\theta\theta}$, σ_{hh}, $\tau_{\theta h}$ Borehole Wall Stresses T = Translational Displacements

where U_ς is the displacement normal to the surface, U_ρ is the radial displacement from the point of indention, F is the applied normal force, ρ is the radial distance from the point of indention, E is the modulus of elasticity, and ν is Poisson's ratio. The relationship of the cylindrical co-ordinate system ρ, ϕ, ς with origin O' at the point of force application to the x-y-z Cartesian co-ordinate sytem described above is illustrated in figure 8. Anisotropy of the rock has not been considered in this study. For rock, E commonly ranges from 10 to 100 GPa; point forces of 50 to 500 N are required to achieve sufficient displacements (0.5 to 5μm) for holographic measurement. Typical Boussinesq displacements (figure 9) are plotted for an applied normal force of 5000 N on an elastic halfspace E = 50 GPa and $\nu = 0.3$.

The Boussinesq solution is an approximation of the true response of the material to the force; for example, the displacement equations (10) and (11) are singular at the point of force application. In reality, a finite area exists at the indenter-rock contact in which nonelastic processes (plastic deformation and fracturing) may dominate the induced displacements near the force application point. Therefore, the solution for an elastic halfspace subjected to a distributed load is more appropriate. The steel indenter typically leaves marks on the borehole wall which are < 1 mm in diameter providing a conservative estimate of the area of contact. The solution for the response of an elastic halfspace to a circular distributed load (Timoshenko and Goodier (1970)) is found by superposition of an infinite number of point loads over the area of contact. A comparison of the point and distributed load solutions with the parameters of figure 9 (table 2) indicates rapid convergence past 0.2 cm from the point of force application; i.e., the distributed

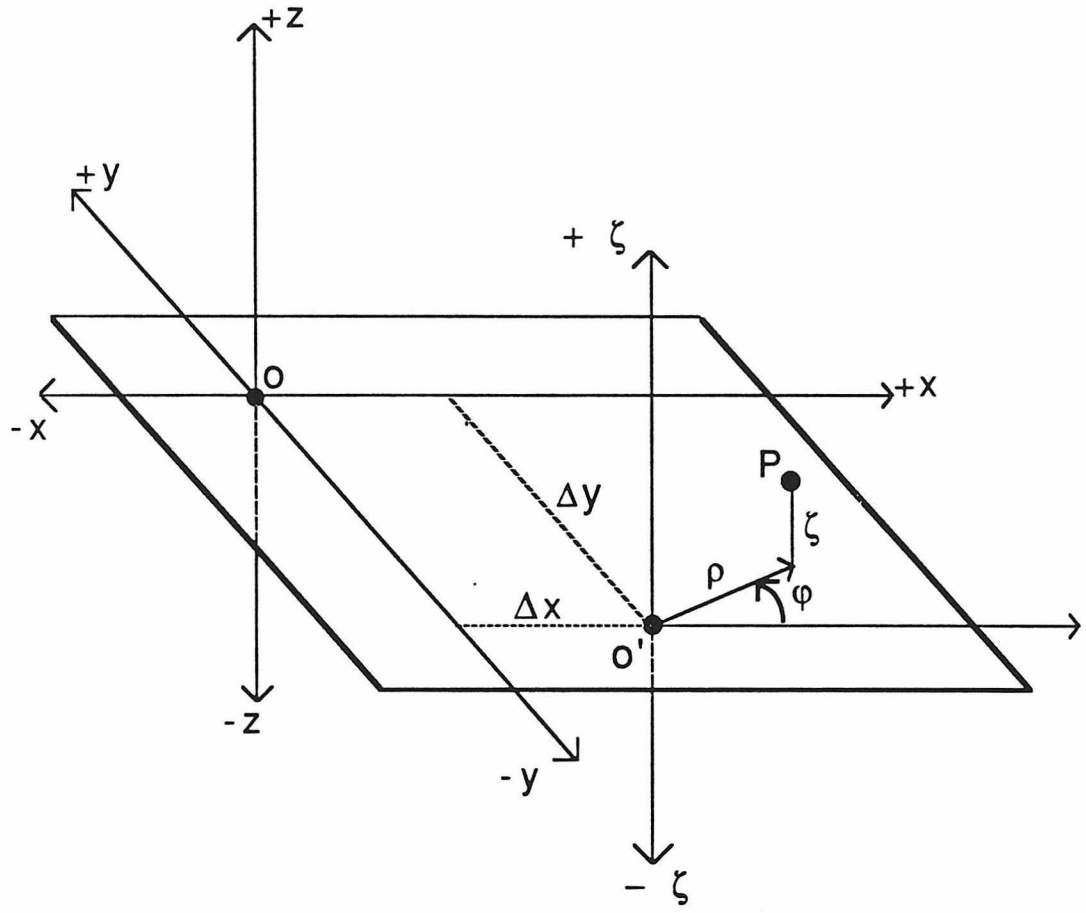

Figure 8). Relationship of cylindrical induced displacement co-ordinate system ρ, ϕ, and ς to hologram Cartesian co-ordinate system x-y-z.

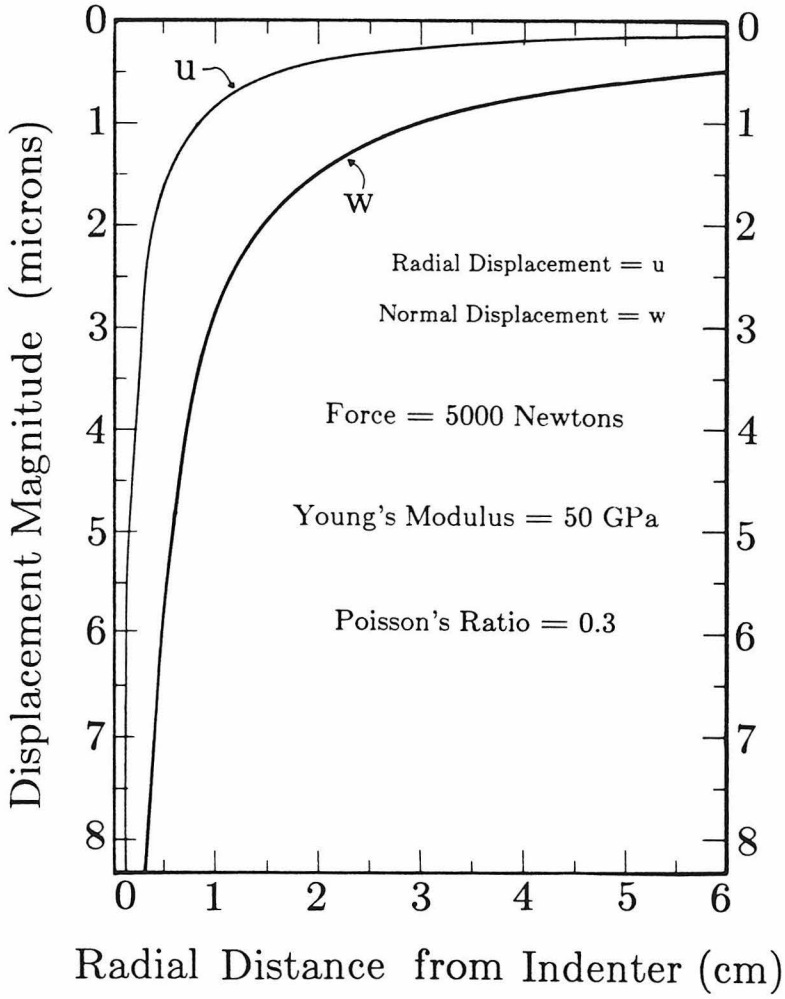

Figure 9). Typical Boussinesq surface displacements due to indention on an elastic material

Table 2) Comparison of Point and Distributed Load Displacements

Force of 5000 Newtons applied to a material of E = 50 GPa and $\nu = 0.3$.

Radial Distance from Force Application (cm)	Point Load Normal Displacement (μm)	Distributed Load Normal Displacement (μm)
0.25	11.58	11.83
0.50	5.79	5.82
1.00	2.896	2.898
1.50	1.9307	1.9309

load values fall within the thickness of the lines drawn for the point load in figure 9. The region less than 0.5 cm from the force application point is blocked by the steel indenter in the reconstructed holographic image; therefore use of the simpler point load solution is justified in holographic determinations of E.

In principle, both E and ν may be found with the holographic technique. In practice, however, the force induced displacements are only weakly dependent upon the value of ν, the number and size of the fringes are strongly controlled by the magnitude of E (figure 10a) whereas variations in ν over the range commonly encountered in rocks (0.25 to 0.35) produce minimal change in the fringe patterns (figure 10b). Figure 11 illustrates quantitatively the differing effect of E and ν on the normal force displacements calculated by equations 10 and 11 as a function of radial distance from the point of force application. U_T is the magnitude of the displacement vector with the components of U_ς and U_ρ:

$$(12) U_T = [U_\varsigma^2 + U_\rho^2]^{\frac{1}{2}}.$$

Values U_T for a constant ν of 0.3 are plotted as a function of radial distance from the point of force application for normal force-modulus of elasticity ratios (F/E) of 10, 5, 3.33, and 2.5 N/GPa (figure 11a) , e.g., for a force of -100 N the value of the modulus of elasticity would be 10, 20, 30, and 40 GPa, respectively, typical for many rocks. For comparison, U_T, for a constant F/E of 4 N/GPa, is plotted for values of ν of 0.15, 0.25, 0.35, and 0.45 (figure 11b). These plots illustrate that the displacements induced by application of a normal point force to the borehole wall surface are

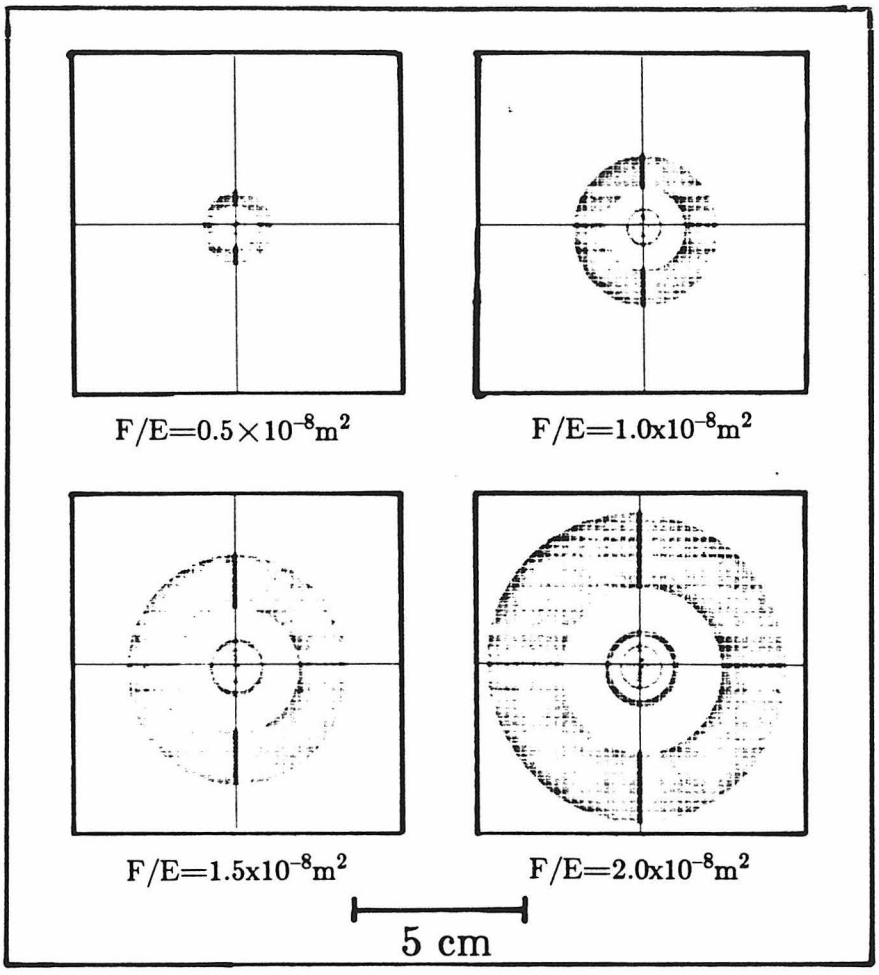

Figure 10a). Sensitivity of the Boussinesq holographic fringe pattern to variations in the modulus of elasticity: E.

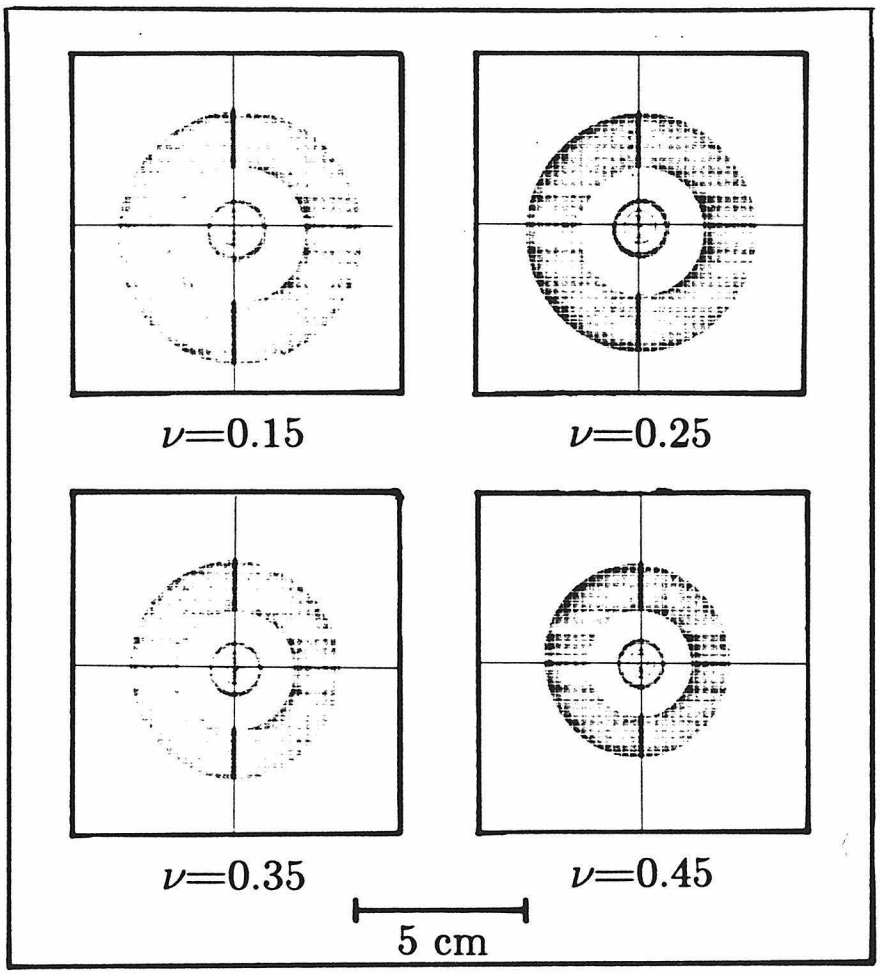

Figure 10b). Sensitivity of the Boussinesq holographic fringe pattern to variations in Poisson's ratio: ν.

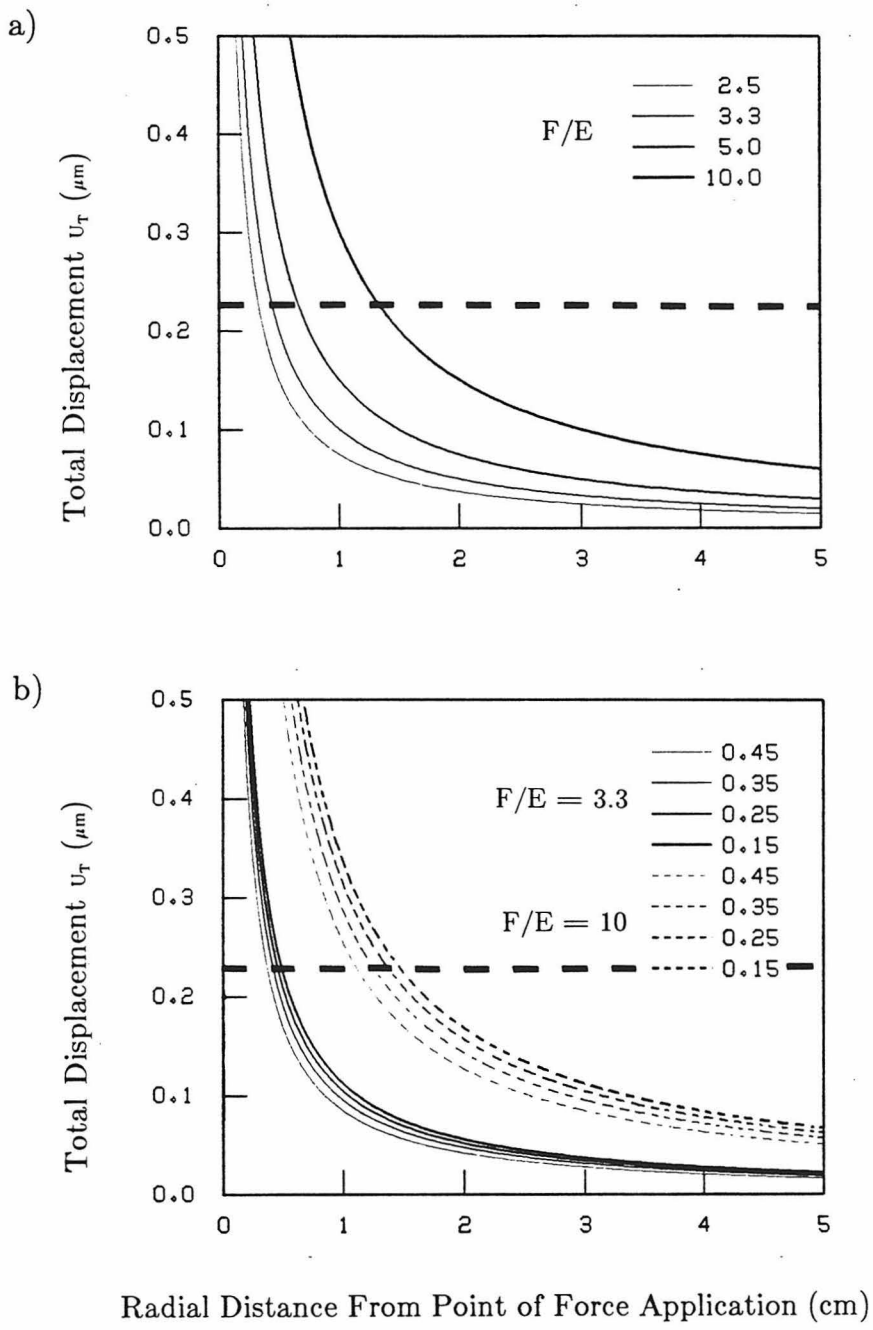

Figure 11). U_T as a function of distance from point of force application for value of F/E of 10, 5, 3.3, and 2.5 N/GPa. Thick horizontal line represents displacements required to produce zeroth order fringe with present optical arrangement. **11b.** U_T as a function of distance from point of force application for changes of Poisson's ratio for two cases of F/E of 10 and 3.3 N/GPa. Thick line same as in 10a.

more dependent upon E than upon ν. The position of the center of the zeroth or first fringe, as determined by forward modelling of fringe patterns, occurs when the magnitude of the induced displacements are $0.230 \pm 0.005\ \mu m$ given the present geometry of the optical recording system; for example, for a typical applied normal force of -100 N on a material of E = 10 GPa (F/E = 10 N/GPa), a change in ν from 0.45 to 0.15 results in a shift of the zeroth fringe center by 0.9 cm; with the same force on a material of ν = 0.25 an increase of E of 3.5 GPa is required to effect the same change in postion. This effect is more graphically illustrated in figure 12 a and b in which the position of the zeroth and first order fringes, determined by forward modelling of fringe patterns, with respect to the point of force application are plotted, in figure 12a the F/E ratio is held constant and ν is the independent variable whereas in figure 12b ν is held constant and F/E is varied. The plot quantitatively illustrates that although the position of the fringes are affected by both E and ν the effect of E is much larger, i.e., small changes in E produce fringe postion shifts larger than those due to extreme changes in ν.

The fringes of an actual reconstructed holographic image have finite width on the order of 1 cm for the zeroth order fringe with poorly defined edges (see figures 18 and 19) making impossible sufficiently accurate determination of the center of a fringe by visual observation. The present forward modelling of fringe patterns is unable to resolve differences in the fringe patterns due to small changes in ν at present; the technique is applied to the determination of E only and a reasonable value of ν for the material under study is initialized in the algorithm.

--

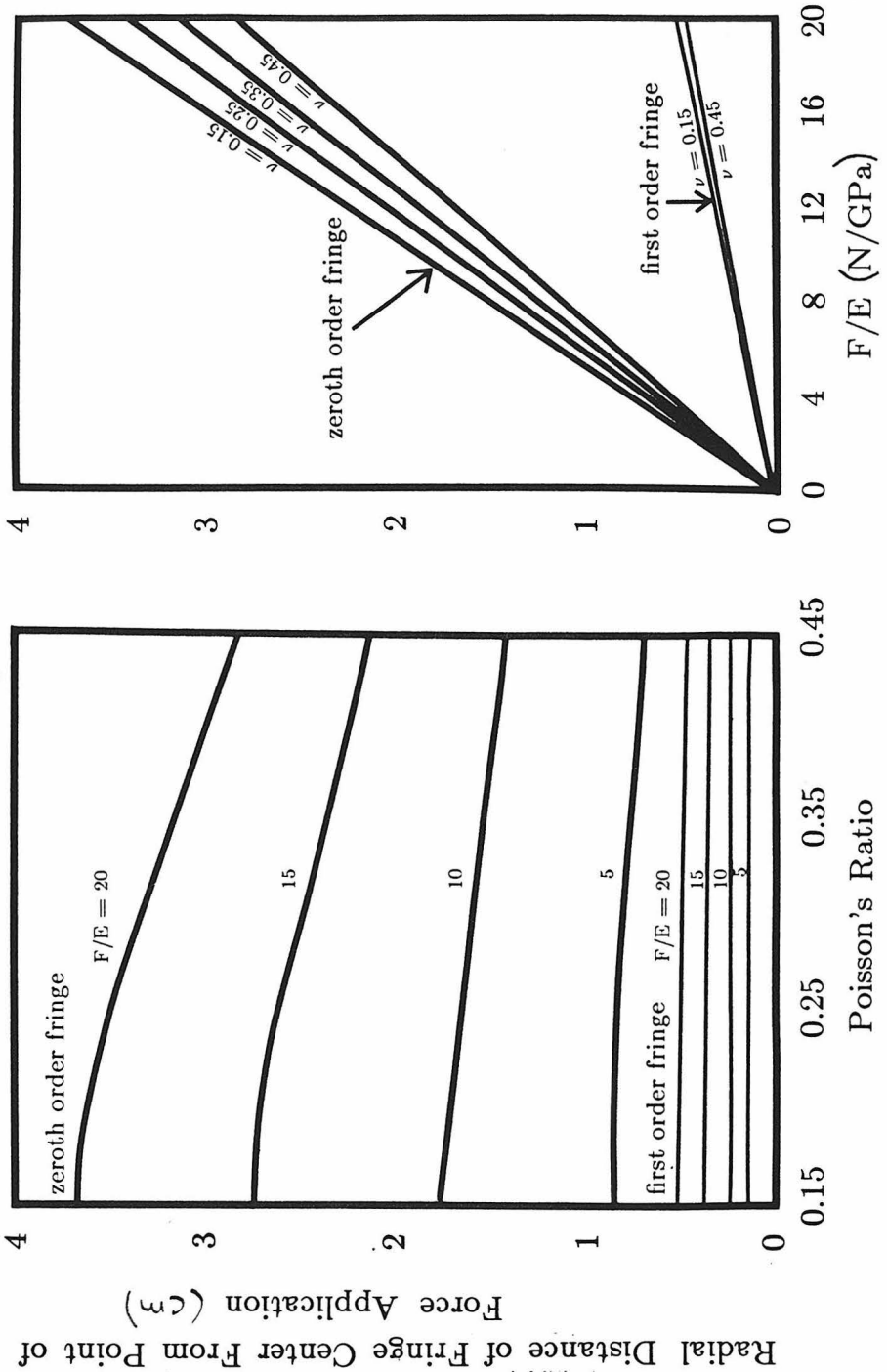

Figure 12). Position of zeroth and first order fringes from point of force application. **12a.** Postion of fringe center versus Poisson's ratio: ν. **12b** Position of fringe center versus force/elastic modulus ratio: F/E.

STRESS MEASUREMENT DISPLACEMENT MODEL

The analytic stress-relief displacement model is based upon the response of an infinite, isotropic, elastic plate with a throughgoing hole and with a thickness dependent upon the stress-relief hole depth (figure 13). The displacement equations (Bass et al. (1986)), are given in terms of the three nontrivial borehole wall stresses:

$$(13)\quad U_\rho = \frac{1}{2E}\left\{(\sigma_{\theta\theta} + \sigma_{hh})(1+\nu)\frac{a^2}{\rho} + (\sigma_{\theta\theta} - \sigma_{hh})\left[\frac{4a^2}{\rho} - (1+\nu)\frac{a^4}{\rho^3}\right]\cos 2\phi + 2\tau_{\theta h}\left[\frac{4a^2}{\rho} - (1+\nu)\frac{a^4}{\rho^3}\right]\sin 2\phi\right\}$$

$$(14)\quad U_\phi = -\frac{1}{2E}\left\{\left[(1-\nu)\frac{2a^2}{\rho} + (1+\nu)\frac{a^4}{\rho^3}\right]\left[(\sigma_{\theta\theta} - \sigma_{hh})\sin 2\phi - 2\tau_{\theta h}\cos 2\phi\right]\right\}$$

$$(15)\quad U_\varsigma = \frac{\nu a^2 t}{E\rho^2}\left[(\sigma_{\theta\theta} - \sigma_{hh})\cos 2\phi + 2\tau_{\theta h}\sin 2\phi\right]$$

where U_ρ, U_ϕ, and U_ς are the displacements relative to the cylindrical co-ordinate system ρ, ϕ, ς centered on the stress-relief hole of radius a and depth $t/2$ (figure 13). In the forward modelling procedure, the three borehole wall stresses: $\sigma_{\theta\theta}$, σ_{hh}, and $\tau_{\theta h}$ are varied until a suitable match is found.

The stress-relief displacement model is not as well understood as simpler normal point force Boussinesq model above. Displacement models commonly applied to blind hole drilling with strain gauges consider only displacements parallel to a surface (Flaman and Manning (1987), Rendler and

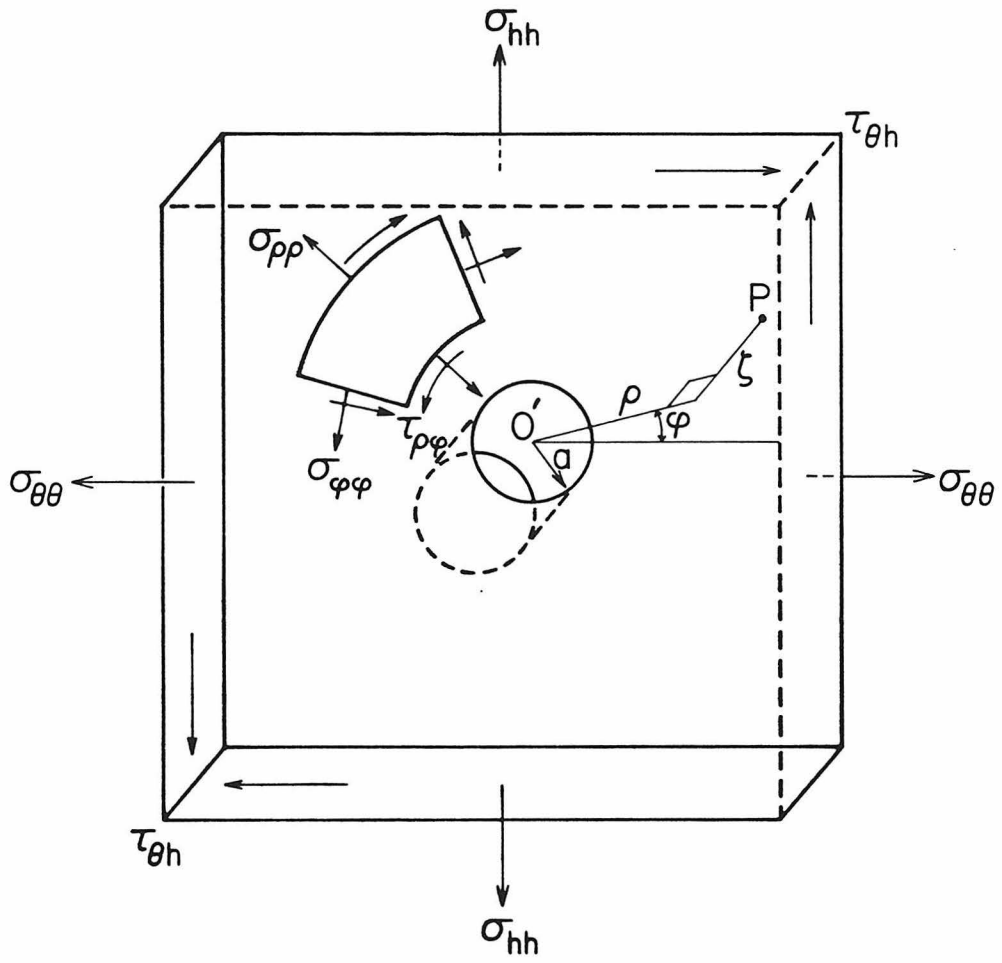

Figure 13). Isotropic, homogeneous, infinite, elasitic plate which forms basis of analytic stress-relief displacement model. Stress-relief hole of radius a and centered on origin of co-ordinate system ρ, ϕ, andς. Plate subjected to nontrivial borehole wall stresses: $\sigma_{\theta\theta}$,σ_{hh} ,$\tau_{\theta h}$. See figure 14b and equations 13, 14, and 15.

Vigness (1966)). Since the holographic technique records a three-dimensional displacement field, motions perpendicular to the borehole surface must also be considered. The model presented must be considered preliminary, however, calibrations of the double-exposure stress-relief experiment indicate the model is a good approximation to the actual displacements (Bass et al., (1986)). For example, in an aluminum block under an uniaxial compressive stress of -120 MPa, the holographically determined stress was -80 MPa suggesting an uncertainty of 35% with the analytic displacement model. Recent two dimensional finite element analysis of the problem suggests that the analytic model underestimates stress-relief displacements resulting in overestimated borehole wall stresses by up to 10% (Smither et al., (1987)).

These three borehole wall stresses: $\sigma_{\theta\theta}$, σ_{hh}, and $\tau_{\theta h}$, are concentrations of farfield stresses (with respect to the X, Y, Z co-ordinate frame (figure 14a,b) by the borehole defined by ((Hiramatsu and Oka (1962), Leeman and Hayes (1966)):

$$(16)\quad \sigma_{\theta\theta}(\theta) = \sigma_{XX} + \sigma_{YY} - 2(\sigma_{XX} - \sigma_{YY})cos\,2\theta - \tau_{XY}\,sin\,2\theta$$

$$(17)\quad \sigma_{hh}(\theta) = -\nu[2(\sigma_{XX} - \sigma_{YY})cos\,2\theta + 4\tau_{XY}\,sin\,2\theta] + \sigma_{ZZ}$$

$$(18)\quad \tau_{\theta h}(\theta) = 2(\tau_{YZ}\cos\theta - \tau_{XZ}\sin\theta)$$

where θ is the azimuth of the hologram in the borehole. Inspection of equations 16, 17, and 18 reveals that at least three observations of the borehole wall stresses:: $\sigma_{\theta\theta}$, σ_{hh}, and $\tau_{\theta h}$ at independent azimuths around the borehole (figure 14b) are necessary to determine the complete farfield stress tensor with normal components : σ_{XX}, σ_{YY}, and σ_{ZZ} and shear components τ_{XY}, τ_{XZ}, and τ_{YZ}. If data from more than three holograms are available

--

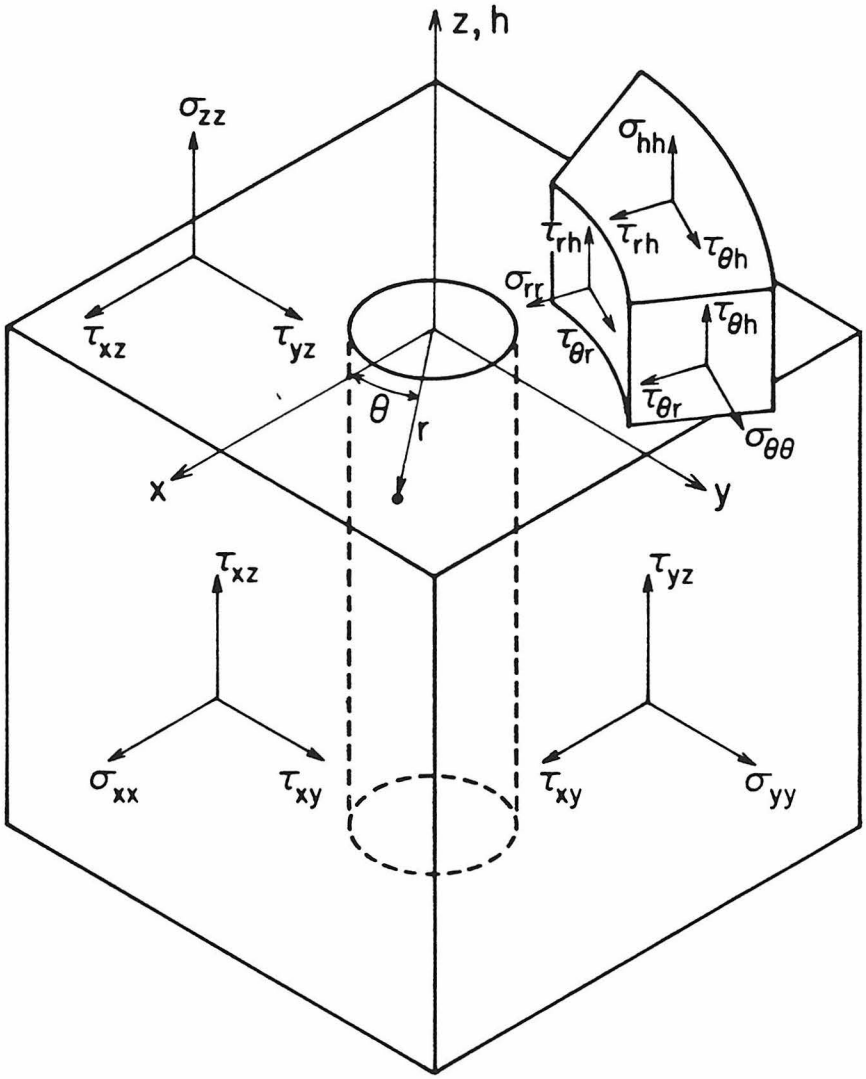

Figure 14a Relationship of borehole and borehole wall stresses to farfield stresses and X-Y-Z Cartesian co-ordinate system.

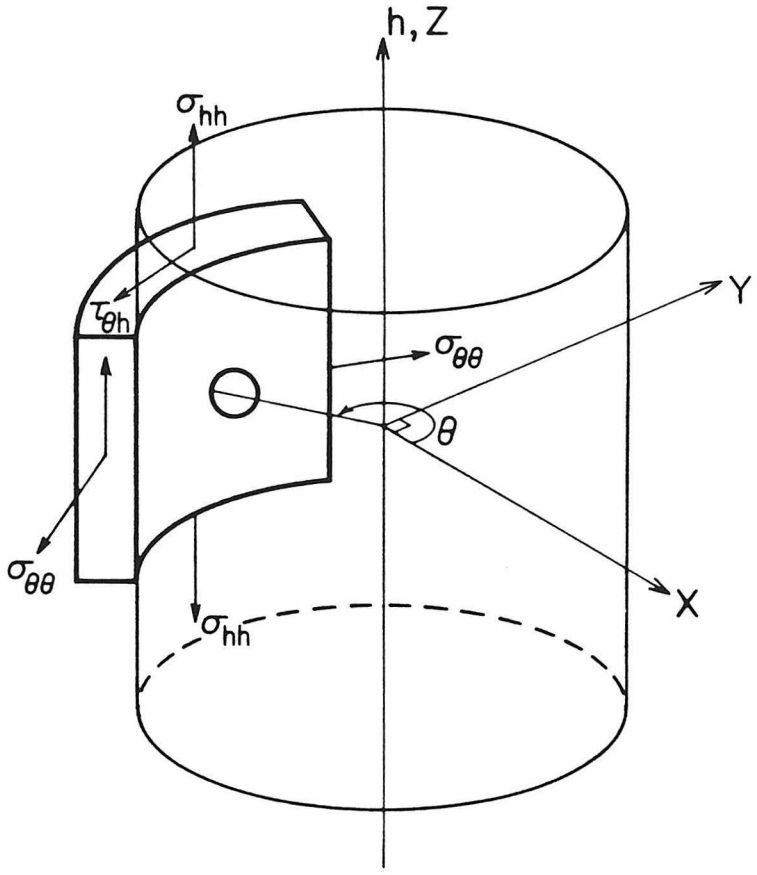

Figure 14b). Placement of model plate in borehole and relationship of cylindrical borehole co-ordinate system: $r-\theta-h$, to borehole Cartesian co-ordinate system: X-Y-Z.

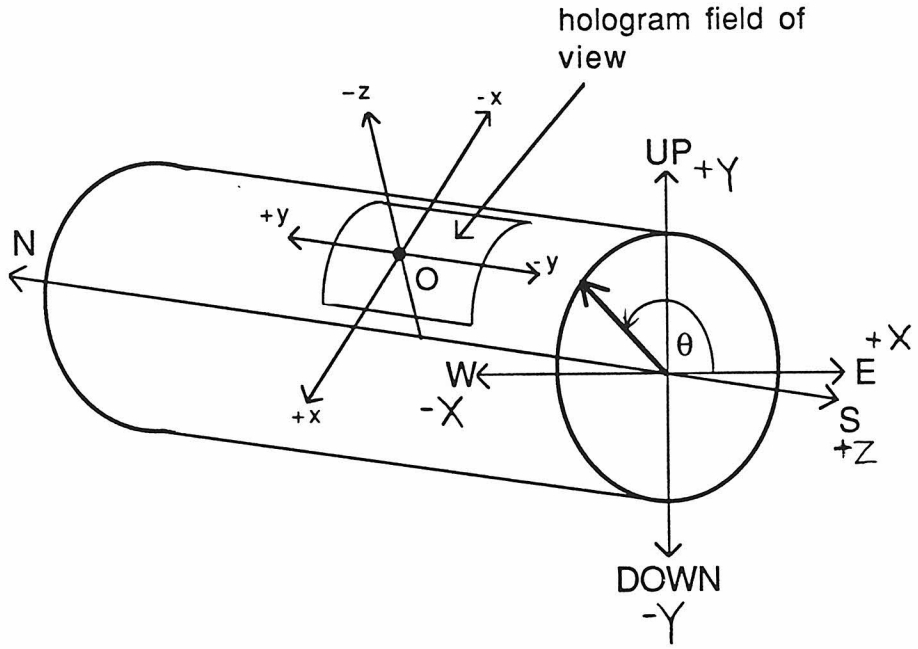

Figure 14c). Relationship of borehole of present field experiments to directions North-South (Z axis), East-West (X axis), and Up-Down (Y axis). Hologram field of view with hologram co-ordinate system: x-y-z, at azimuth: θ.

the farfield stresses may be determined via the method of least squares (Smither et al., (1987)). The relationship of the X-Y-Z co-ordinate system to the North-South horizontal borehole in which the field experiments were conducted is shown in figure 14c.

FIELD EXPERIMENTS

In the prototype borehole instrument which has been constructed (Bass et al., (1986)), stability is a critical consideration. Motion of the optical recording system between holographic exposures yields additional rigid body displacement fringes in the final image. To minimize this problem, the instrument is composed of two mechanically separated modules. The drill/force module drills the stress-relief hole for the stress experiment or applies a known normal point force to the borehole wall for the elastic modulus experiment. The second, or optics module, contains a He-Ne laser (632.8 nm), holographic film, and the optics required to create an off-axis hologram. To maintain stability, the two modules are mechanically separated to reduce vibrations experienced by the module during drilling or force application and are separately locked via rams into the borehole.

During a stress measurement experiment, after the instrument is locked into place an initial holographic exposure is made of the borehole wall. A drill is lowered into the view of the hologram and a small (approximately 1 cm diameter) stress-relieving hole is drilled into the wall. In response to the new boundary conditions, the rock elastically deforms (figure 2). The drill is removed from the field of view and the second holographic exposure is made. The film is then advanced and the instrument moved to another

location within the borehole for another experiment.

The elastic moduli experiment differs only in that, instead of drilling the stress-relief hole, a known force is applied perpendicularly to the borehole wall by a steel indenter and maintained through the second exposure (figure 1). Conversely, the force may be applied during the first exposure and released prior to the second exposure.

During a field experiment, the amount of force applied is proportional to nitrogen cylinder supplied air pressure of 70 to 790 kPa supplied to two air pistons (Bimba #FO-31-1.5) and measured to an accuracy of 0.25% by air pressure gauges (Glasco). In a horizontal borehole the amount of force applied the the borehole wall is dependent upon the instrument azimuth (θ) as the air pistons must lift the mass of the steel indenter against gravity. Additionally, there are frictional losses. Calibration of the applied force was carried out in the laboratory in a concrete tube mock borehole using a cantilever beam load cell (figure 15a) consisting of four strain gauges (Measurements Group, #CEA-06-500UW-350) bonded with epoxy (Devcon "Super Glue") to a steel strip (0.47 cm thick) and configured in a Wheatstone bridge (figure 15b). Care is taken to account for and reduce hysterisis and temperature effects. The load cell was activated with a potential of 10 volts provided by a regulated DC power supply (Lambda #LH-124 FM) and can measure loads up to 2000 N without permanent deformation. Voltage imbalances of 2.55 to 41.30 mV across the strain gauge wheatstone bridge were monitored by a digital voltmeter (Keithly #173 DMM) with a resolution of 0.01 mV which corresponds to a sensitivity of 0.5 N/mV. Force as a function of cylinder air pressure determined by comparing load cell response during

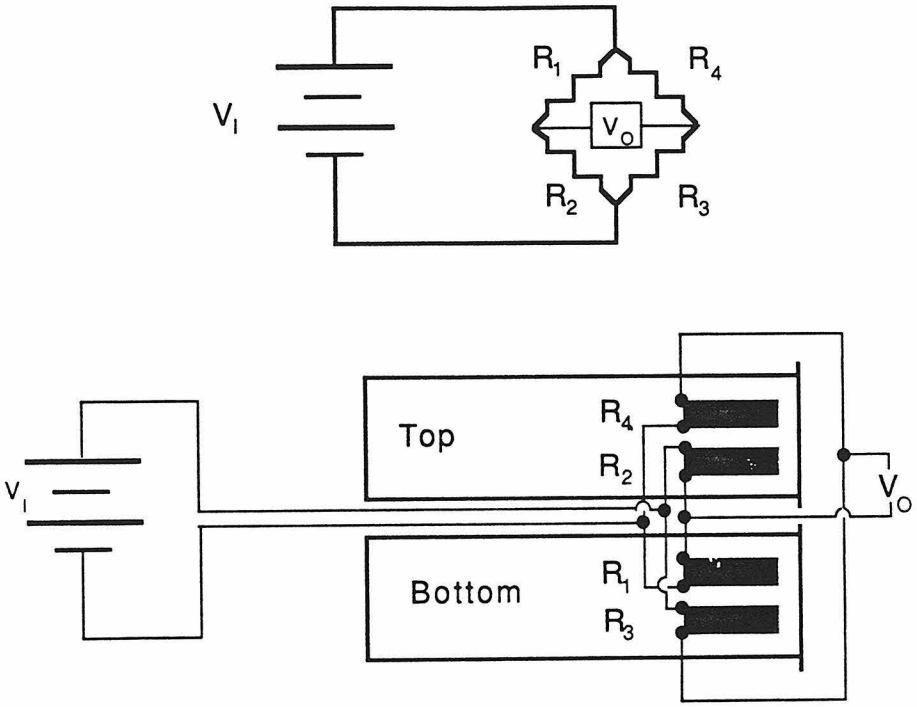

Figure 15b). Schematic diagram of Wheatstone bridge configuration of strain gages, V_1 is the input or activation voltage and V_O is the output voltage of the bridge. Small change in the resistances R_1, R_2, R_3, and R_4 due to the deformation of the load cell result in a change in V_O for constant V_I. Wiring diagram illustrates strain gage configuration which obtains maximun sensitivity.

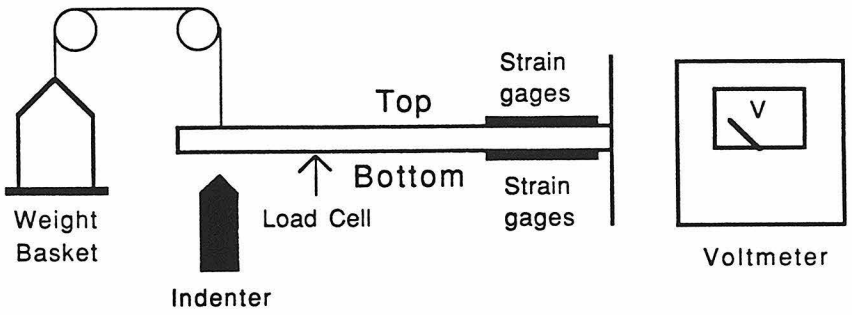

Figure 15a). Schematic of load cell for calibration of forces applied to borehole wall showing position of strain gages on steel cantilver beam.

force application at a variety of air pressures from 70 to 760 kPa and borehole azimuths: θ, (figure 14c) to the response of the system to a series of known masses from 6.0 kg to 88.5 kg (figure 16) via a sytem of pulleys with no mechanical advantage. The results of this calibration of the *in situ* applied forces at $\theta = 0$ and 90 degrees (figure 17) yields the following formula for the field experiments:

$$(19) \quad F = g\,(C \cdot P - (W sin\,(\theta) + f\,))$$

where F is the applied force in N, g is the acceleration of gravity (9.8 m/s^2), P is the air pressure supplied to the cylinders in kPa, C is a constant related to the area of the pistons (0.30 kg/kPa), W is the mass of the steel indenter which must be lifted against gravity in a horizontal borehole (5.2 kg), f is a mass equivalent of the frictional forces within the pistons (3.0 kg), and θ is the azimuth within the borehole. In figure 17, data collected at $\theta = 0$ ° are represented by error bars centered on black dots and data collected at $\theta = 90$ ° are simple error bars. The error bars represent the range of the maximum and minimum masses which were applied to the load cell to obtain the same response as the normal force supplied by the pistons for several tests at a given air pressure. Comparison of the lines lines of $\theta = 0$ ° and $\theta = 90$ ° calculated using equation 19 and the observed force-air pressure relationship of the data points suggest that the uncertainty in the determination of the force when equation 19 is applied is 10 %. The datum at θ=90 °, F = 600 to 700 N, and P = 300 kPa deviates significantly from the line calculated for $\theta = 90$ ° and is believed to be an error in the measurement of the mass applied to the load cell.

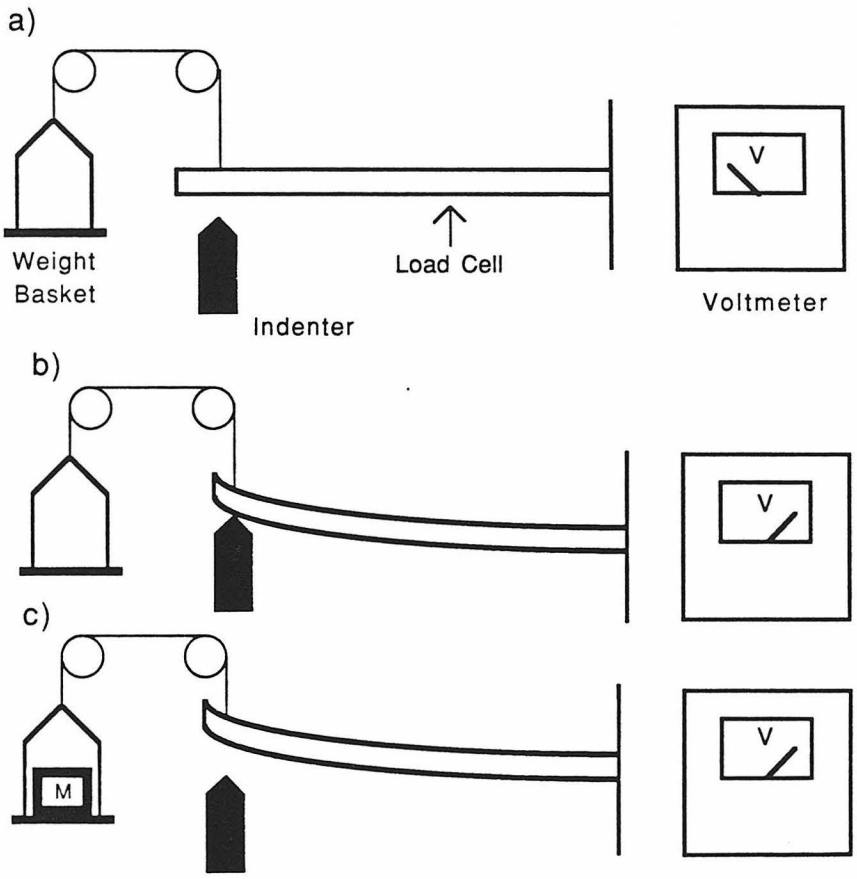

Figure 16 a. Schematic of load cell with no normal force or masses applied yielding low voltage. **b.** Load cell after application of normal force with indenter, voltage is noted. **c.** Normal force removed and sufficient mass applied to achieve same response and give force supplied by indenter in **b.**

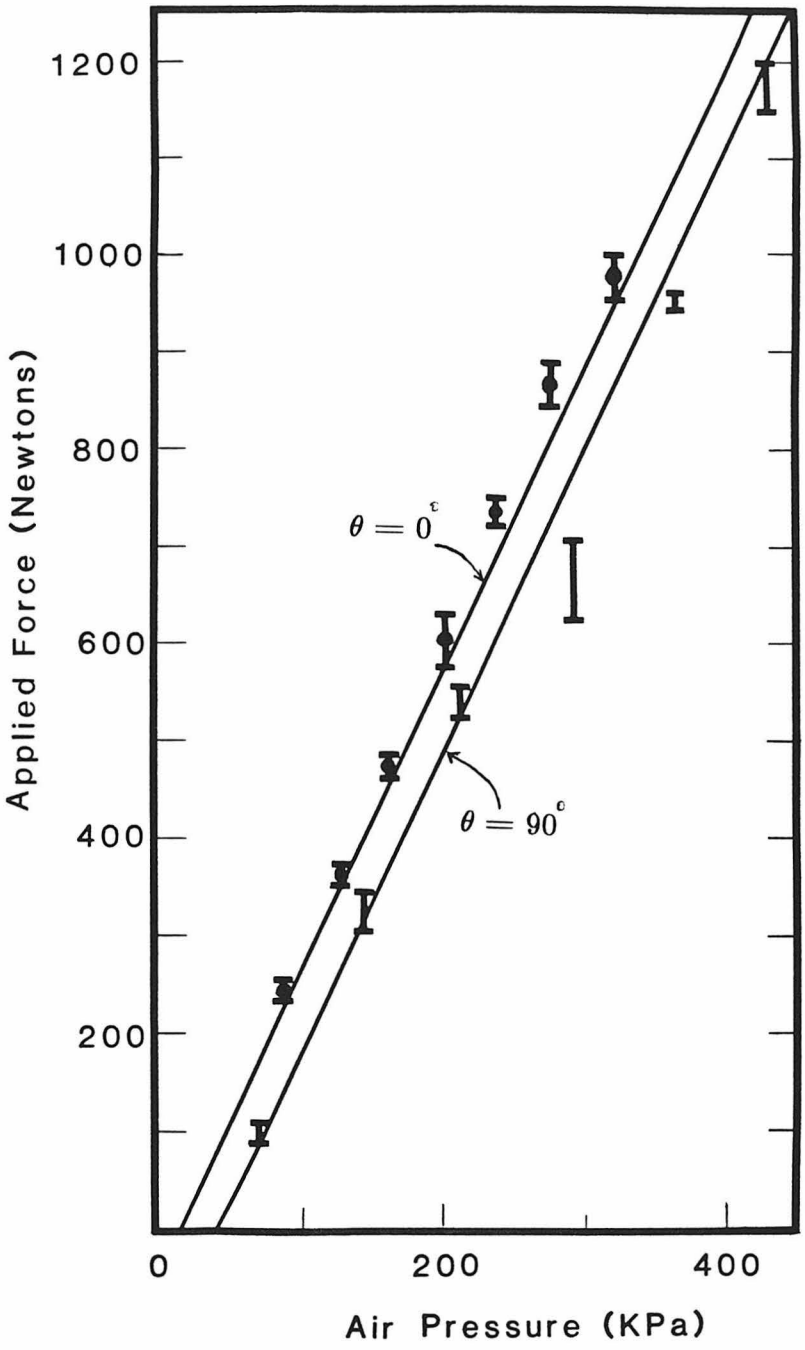

Figure 17). Calibration curves of normal force applied by steel indenter to borehole wall at azimuthes of $\theta = 0$ (error bars centered on dots) and $\theta =$ 90 degrees (simple error bars) vs. air pressure supplied to pistons which drive steel indenter. Lines calculated at constant θ of 0 and 90 degrees using equation 19 derived from this data.

LABORATORY EXPERIMENTS

Elastic modulus measurement holographic experiments were conducted in the laboratory to evaluate the applicability of the method and to gain experience with the data analysis procedures. Briefly, well-known normal forces from 50 to 2000 N were applied to aluminum and brass blocks (2.54 cm thick, 25.4 cm square). In these bench tests, the indenter was a specially built steel lever with adjustable mechanical advantages of 0.5, 1.0 and 2.0 which magnified the force supplied at one end by a compressed air piston (Bimba #FO-125-4-EE2) (figure 18). The optics module was placed over, but not in contact with, the apparatus in order to make holographic exposures for the tests. Force magnitudes during a test were monitored by a Wheatstone bridge configuration of strain gauges (Measurements Group, #CEA-06-500UW-350) in a manner similar to those of figure 15 allowing resolution of forces to better than 2%: the resolution accuracy of the hydraulic load cell (Enerpac model LC-102 with a Enerpac series L-1 gauge with a resolution of $\pm$ 10 N is used to calibrate the system.

RESULTS and DISCUSSION

Forces from 206 to 1576 N were applied to yellow brass (Muntz metal, 59.5% copper, 40% zinc, 0.25% tin, 0.25% lead, ASTM B171, alloy #365) (figure 19, table 3) the modulus of elasticity was determined at 100 $\pm$ 10 GPa near a published value of 103 GPa for a composition of 60% copper and 40% zinc (Gray (1963)). The change in the fringe pattern with increasing force is apparent. The large circular outer fringe is of zeroth order, fringe order increases as the point of force application is approached. In general, the

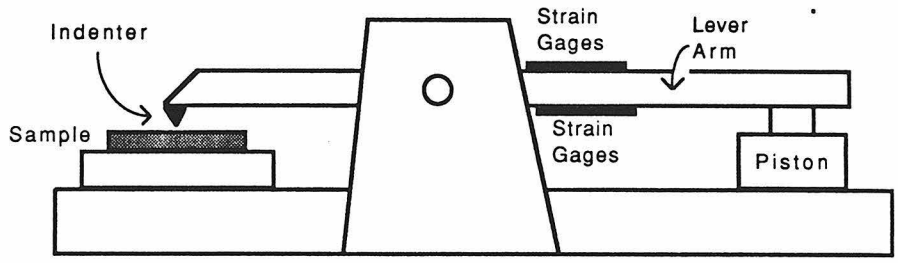

Figure 18 Schematic drawing of bench apparatus for testing of elastic modulus experiment. Metal or rock sample is securely mounted on apparatus and a normal force applied by a lever powered by an air piston. Applied force is measured by strain gauges in a manner similar to figure 15.

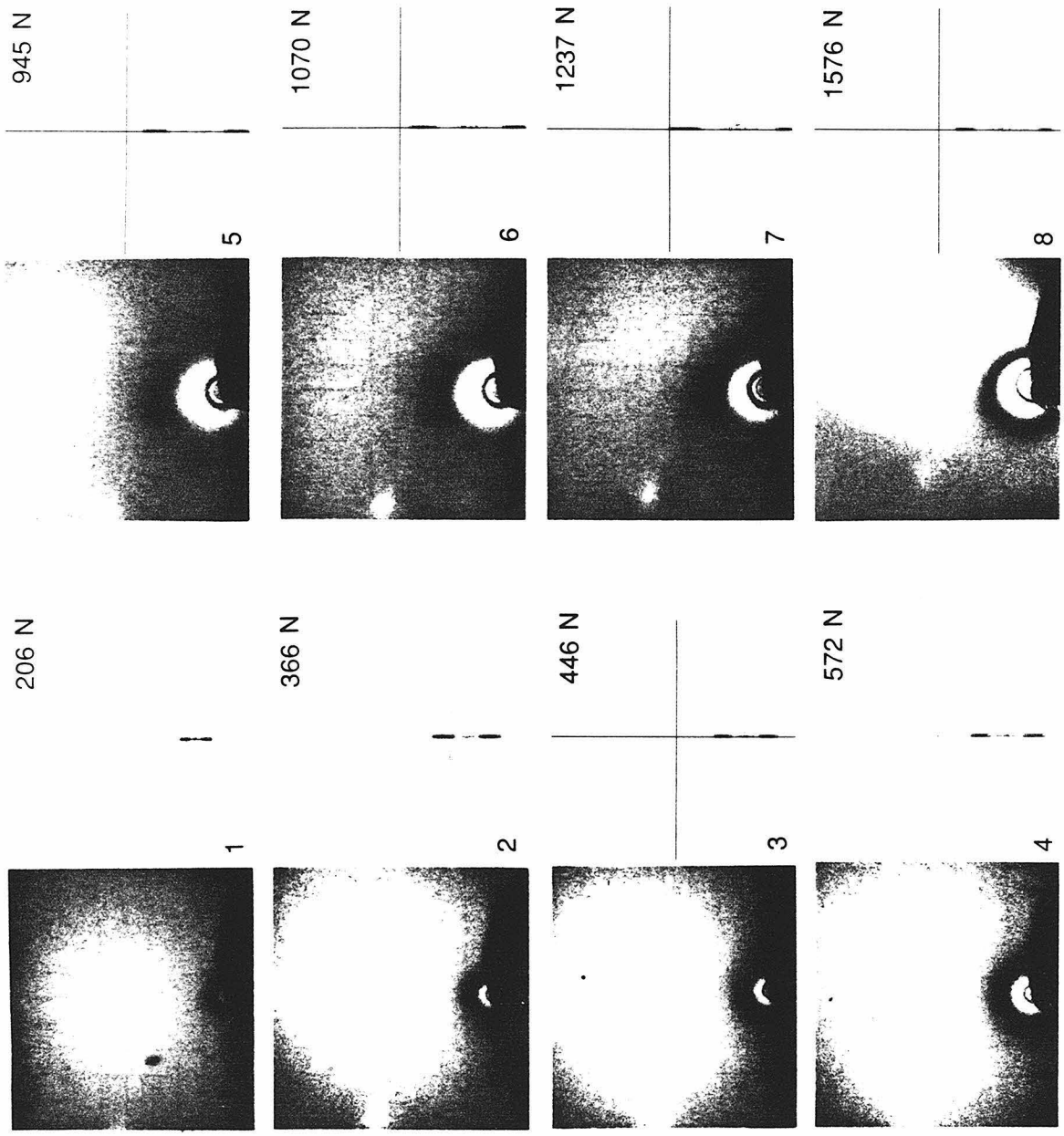

Figure 19). Laboratory Observed and Corrsponding Synthetic Fringe Patterns for Elastic Modulus Experiment. Centimeter grid scribed in brass is seen in photographs. Circular point force induced fringes are centered on steel indenter in photograph foreground.

Table 3) Laboratory Calibration on Brass

Test Number	Hologram Co-ordinates (cm)			Applied Force (N)	Translations (μm)			Elastic Modulus (GPa)
	x	y	z		x	y	z	
1	-2.675	5.800	18.56	206	0.000	0.000	0.025	100 ± 10
2	-0.450	5.650	18.56	366	0.000	0.000	0.050	100 ± 10
3	0.200	5.650	18.56	446	0.000	0.000	0.025	100 ± 10
4	0.175	5.700	18.56	572	0.000	0.000	0.025	95 ± 5
5	-0.450	5.450	18.56	945	0.000	0.000	0.000	100 ± 5
6	0.300	5.450	18.56	1070	0.000	0.000	0.000	100 ± 5
7	2.000	6.050	18.56	1237	0.000	0.000	0.000	100 ± 5
8	3.250	4.700	18.56	1576	0.200	-0.200	0.000	100 ± 5

Note: Force Application Point: x = 0.00, y = -2.75 cm, z = 0.00.

Source co-ordinates: x = -6.19 cm, y = 0.00, z = 8.20 cm.

diameter of the zeroth order fringe increases with force, however, there are anomalous cases in which this fringe is larger for smaller applied forces. These situations are a result of small translations (table 3) of either the optics module taking the holograms or the brass block to which the force is applied. The translations affect the zeroth order fringe more than higher order fringes because the latter are a result of larger displacements, i.e., the signal (Boussinesq displacement magnitude) to noise (translational displacement magnitude) ratio increases with fringe order. This is further apparent in the uncertainty inferred from fitting fringe patterns to obtain E which appears to slightly decrease with increasing force; this uncertainty reflects the resolution of the forward modelling technique.

Similar results are observed in tests on aluminum (alloy 2024, 3.8-4.9 % copper, 0.5 % max silicon, 0.5 % max iron, 0.3-0.9 % manganese, 1.2-1.8 % magnesium) (figure 20, table 4) with applied forces from 525 to 1989 N. These holograms are of particular interest in that the larger applied forces produced sizable translations which are evidenced by the long subhorizontal parallel fringes across the photographs. Despite the addition of these additional fringes to the hologram, the modulus of elasticity of the aluminum block was found to be 70 $\pm$ 5 GPa in close agreement with the published value of 73.1 GPa for an aluminum alloy with similar composition (4.5 % copper, 1.5 % magnesium, and 0.6% manganese, Gray (1963)). Unexpectedly, the translational fringes allow a greater confidence in the result due to the fact that if these fringes are readily observable (as in the last three photographs of figure 20) they may easily be modelled and accounted for and directly yield the dark fringe order. In contrast, the accuracy of

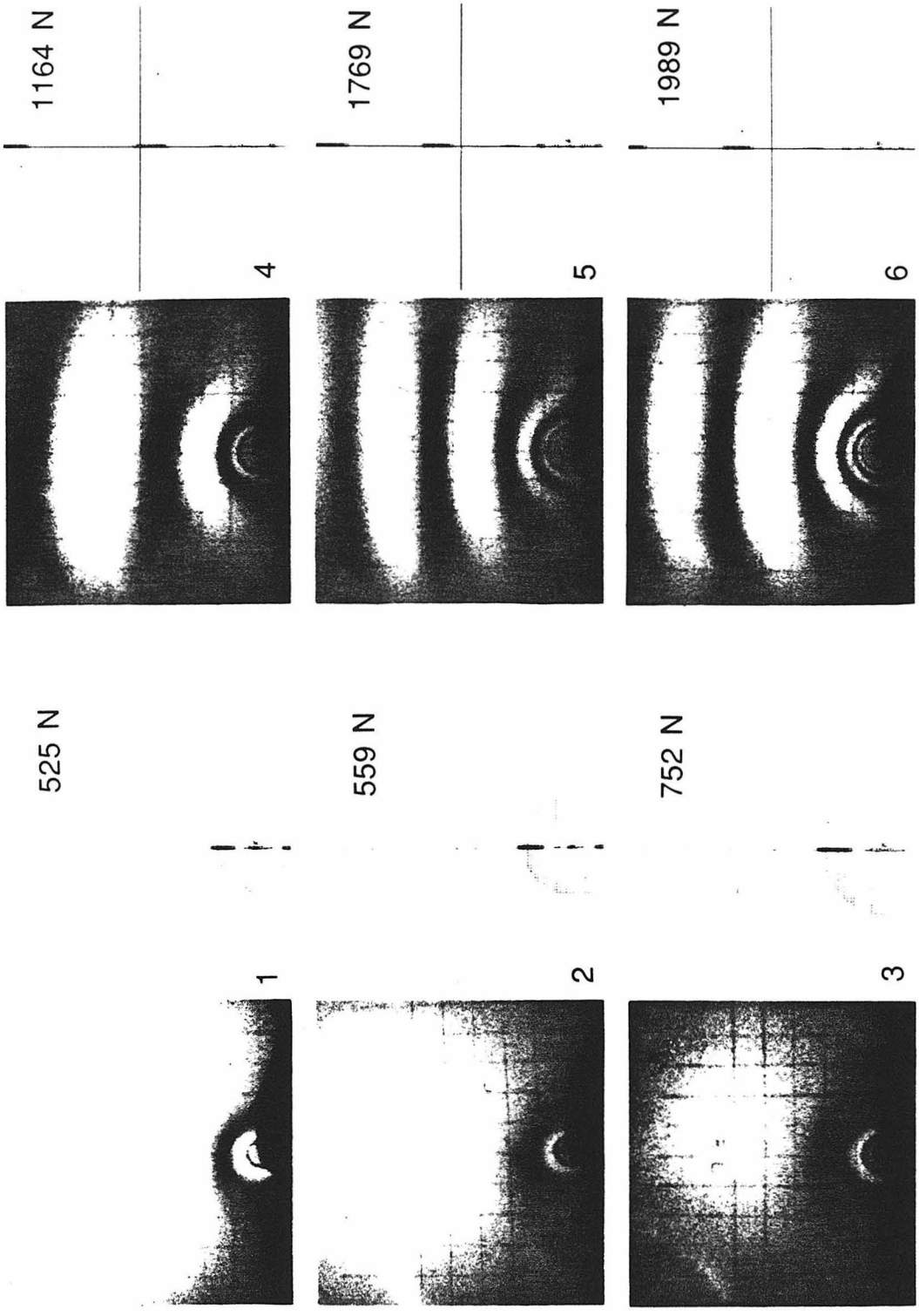

Figure 20). Laboratory Observed and Corresponding Synthetic Fringe Patterns for Elastic Modulus Experiment in Aluminum. Circular fringes are due to displacements by known point force. Translational fringes are apparent in last three holograms and were successfully accounted for in the data analysis.

Table 4) Laboratory Calibration on Aluminum

Test Number	Hologram Co-ordinates (cm)			Applied Force (N)	Translations (μm)			Elastic Modulus (GPa)
	x	y	z		x	y	z	
1	0.075	5.500	18.56	525	0.000	0.000	0.000	67.5 ± 2.5
2	0.900	5.400	18.56	559	0.000	0.000	0.000	70 ± 5
3	0.075	5.550	18.56	752	0.000	0.000	0.000	70 ± 5
4	3.175	4.700	18.56	1164	0.000	0.700	-0.080	70 ± 5
5	2.275	5.500	18.56	1769	0.000	1.000	-0.060	70 ± 5
6	1.900	5.500	18.56	1989	0.000	1.000	-0.080	70 ± 5

Note: Force Application Point: x = 0.00, y = -3.75 cm, z = 0.00.

Source Co-ordinates: x = -6.19 cm, y = 0.00, z = 8.20 cm.

the measurement on some of the brass holograms was low due to the fact that the size of the zeroth order fringe was slightly changed by translational displacements of insufficient magnitude to produce a fringe over the viewing area of the hologram.

LABORATORY RESULTS ON ROCK

Laboratory holographic experiments were also conducted on a block of dolomitic marlstone (figure 21, table 5) taken from the same mine in the Mahogany formation in Garfield County, Colorado, in which earlier (Bass et al., (1986), Schmitt et al., (1986)) and present field experiments have been carried out. The rock is a keragenaceous dolomitic marlstone (oil shale); density of our sample was measured to range from 2.24 $\pm$ 0.01 g/cm^3 to 2.31 $\pm$ 0.01 g/cm^3 for three cores with axii perpendicular to the bedding plane of the rock taken from the block for ultrasonic measurements (table 6). Reported porosities of the rock are < 2 % as found by comparison of wet and dry sample weights (Blair (1955)). Ultrasonic (1 MHz) compressional wave velocities (V_p) together with the measured densities (d) and assumed values of ν (table 6) via the formula:

$$(20) \quad E_D = \frac{V_p \, d \, (1 - \nu)}{(1 + \nu)(1 - 2\nu)}$$

yield dynamic modulus of elasticity: E_D, values for the rock of 13.5 to 19.1 GPa. Values measured by the holographic technique are static compressional determinations.

In the holographic test, normal forces, applied perpendicular to the bedding plane, ranged from 79.8 to 455 Newtons. The values of E were

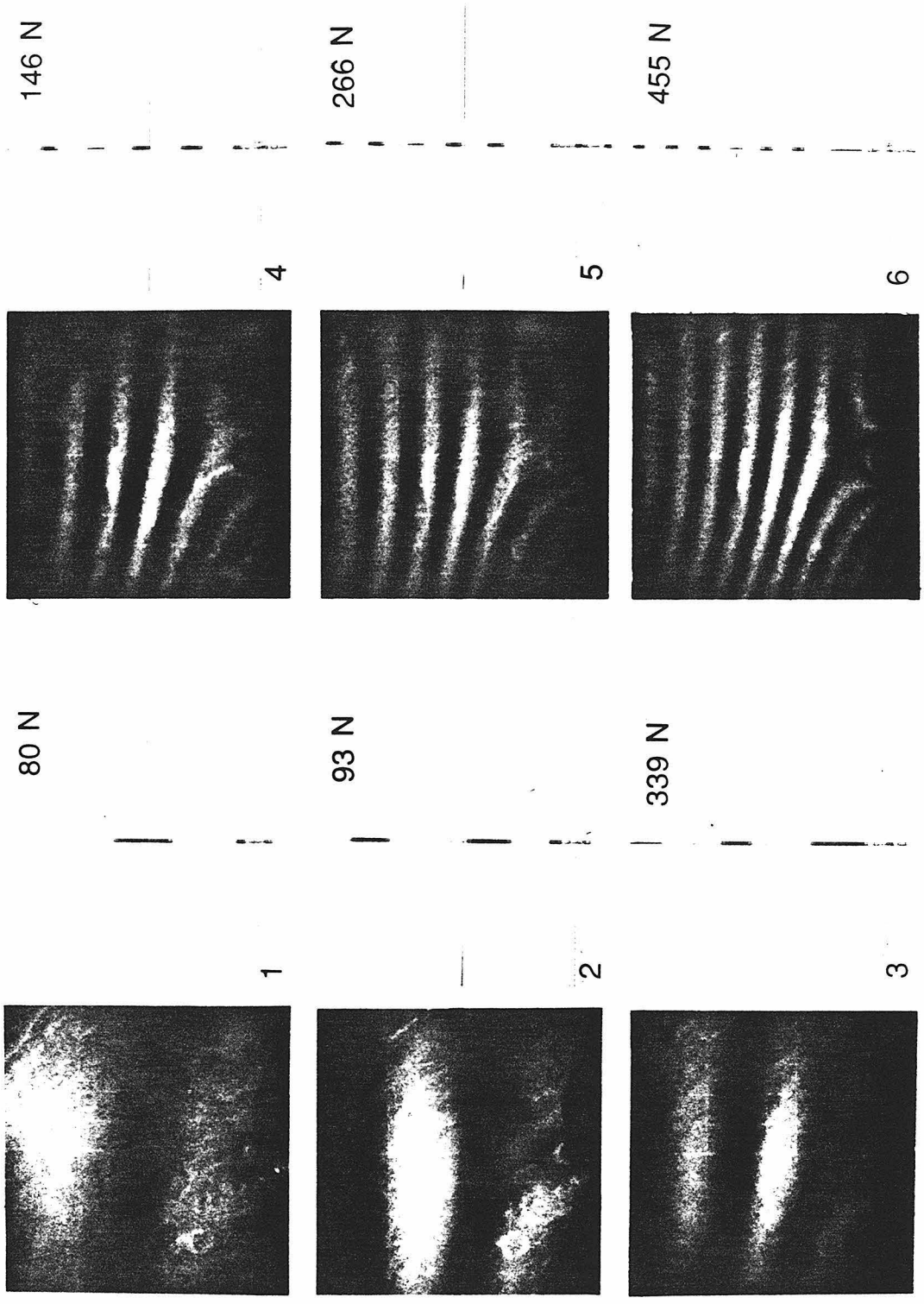

Figure 21. Laboratory Observed and Corresponding Synthetic Fringe Patterns in Dolomitic Marlstone.

Table 5) Laboratory Calibration on Dolomitic Marlstone

Test Number	Hologram Co-ordinates (cm)			Applied Force (N)	Translations (μm)			Elastic Modulus (GPa)
	x	y	z		x	y	z	
1	1.675	5.100	18.56	80	0.275	0.800	-0.180	16.5 ± 2.5
2	0.225	4.500	18.56	93	0.050	1.200	0.000	16.25 ± 1.75
3	1.725	4.100	18.56	146	0.300	1.600	-0.070	18.25 ± 1.25
4	0.800	4.800	18.56	266	0.800	3.050	-0.200	17.5 ± 1.0
5	0.575	4.050	18.56	339	0.600	3.600	-0.200	17.0 ± 1.0
6	0.000	5.050	18.56	455	1.000	4.550	-0.225	17.5 ± 1.0

Note: Force Application Point: x = 0.00, y = -3.75 cm, z = 0.00.

Source Co-ordinates: x = -6.19 cm, y = 0.00, z = 8.20 cm.

Table 6) Parameters of Ultrasonic Experiments on Dolomitic Marlstone

Sample	Core Density g/cm^3	Core Length cm	Transit Time μs	Longitudinal Velocity km/s	Dynamic Modulus ν=0.25 GPa	Dynamic Modulus ν=0.35 GPa
1	2.28±0.01	1.912±0.001	6.25±0.11	3.08±0.05	18.0	13.5
2	2.31±0.01	2.921±0.001	9.50±0.11	3.08±0.04	18.2	13.6
3	2.24±0.01	2.271±0.001	7.10±0.07	3.20±0.04	19.1	14.3

determined by forward modelling of the observed fringe patterns (figure 21, table 5) to be 16.8 ± 2.8 GPa. Good matches between the observed fringe patterns in the photographs and the calculated fringe patterns in the synthetics were obtained. The holographically determined E is in excellent agreement with a value of 17.2 ± 2.0 GPa for a static compressive E predicted on the basis of the density of our ultrasonically tested samples (Blair (1955)).

The ratio of the static E to dynamic (E_D) modulus for a Colorado oil shale is reported to be $\sim$ 0.7 and decrease slightly with increasing confining pressure to 220 MPa (Cheng and Johnston (1981)), this is anomalous behavior as, for most rocks, the ratio approaches unity with increasing pressure due to closing of microcracks within the rock mass. Although lack of knowledge of ν precludes an accurate determination of E/E_D in the present study, the above data yields a value for the ratio of 0.88 ± 0.15 which is consistent with the results of Cheng and Johnston (1981).

FIELD RESULTS

Field tests of both the elastic modulus measurement experiment and the stress measurement were made with the stressmeter in a 30.5 cm diameter , north-south, horizontal borehole drilled into a mine pillar composed of the marlstone used in the above laboratory experiment.

ELASTIC MODULI EXPERIMENT

Twelve elastic modulus holograms from four different positions within a horizontal borehole in an oil shale mine pillar in the Mahogany formation of Garfield County, Colorado, and with a variation of applied forces have been analyzed (figures 22, 23, 24, and 25 and table 7). The novelty of the present technique dictates that a complete presentation of the data be given including the observed and synthetic fringe patterns. The in situ values of E, averaged at each of the four test postions within the borehole, ranged from 26.9 $\pm$ 2.9 GPa to 34.0 $\pm$ 2.0 GPa with a maximum uncertainty of $\pm$ 5.8 GPa or approximately 20 %. An independent measurement of these in situ values is not available, however earlier laboratory static compression tests yielded values which range from 8 to 39 GPa (Blair (1955), Windes (1950)).

Although the present data set is small, a dependence of E on azimuth (θ) within the horizontal borehole cannot be precluded (figure 26). The four data points in figure 26 represent the extremum values (i.e., the top and bottom of each error bar are the maximum and minimum values, respectively, when uncertainties are considered) of the holographically determined *in situ* Young's modulus at each of the four locations within the borehole studied (table 7). Fitting a straight line through the data of figure 26 yields a Young's modulus azimuth relation (a linear relationship is not suggested between θ and Young's modulus, data quality does not warrant, however, a more complicated relationship and the fits were made to illustrate only that Young's modulus appears to depend upon θ):

$$(21)\quad E(\theta) = (41.1 \pm 7.7\, GPa) - (0.077 \pm 0.032 \frac{GPa}{degree})\theta.$$

Table 7) Borehole Field Measurements of Elastic Modulus

Test Number	Depth (m)	Azimuth (degrees)	Hologram Co-ordinates (cm)			Force Position (cm)		Applied Force (N)	Translations (μm)			Elastic Modulus (GPa)
			x	y	z	Δx	Δy		x	y	z	
3-5	3.25	90	1.200	2.800	18.90	0.50	-2.75	197	-0.100	0.850	-0.055	30.5 ± 2.5
3-7	3.25	90	-0.825	4.300	18.90	0.60	-2.40	440	0.000	1.500	1.800	35.0 ± 2.5
3-8	3.25	90	0.500	3.300	18.90	0.65	-2.55	752	0.000	3.400	3.415	36.0 ± 3.0
8-1	2.20	135	0.050	4.250	18.90	1.15	-2.45	207	-0.700	1.200	0.000	27.0 ± 1.0
8-3	2.20	135	0.000	5.050	18.90	1.00	-2.55	317	-0.650	2.200	-0.050	29.5 ± 1.5
8-8	1.63	180	0.750	4.800	18.90	1.05	-2.40	146	-0.500	1.000	0.700	25.3 ± 1.3
8-5	1.63	180	0.400	3.150	18.90	0.80	-2.55	182	-2.100	-0.500	-0.010	26.0 ± 1.5
8-6	1.63	180	0.750	4.450	18.90	0.80	-2.40	232	-1.250	0.040	0.000	28.0 ± 1.5
8-7	1.63	180	0.900	4.450	18.90	0.85	-2.50	319	-0.070	1.300	0.000	28.3 ± 1.3
8-9	1.63	135	0.700	4.800	18.90	0.50	-2.40	186	-0.200	0.550	0.000	34.0 ± 2.0
8-10	1.63	135	-1.050	3.200	18.90	0.55	-2.60	136	-0.160	0.700	0.000	34.0 ± 2.0
8-11	1.63	135	1.450	3.200	18.90	0.70	-2.60	327	-0.300	1.100	-0.040	34.0 ± 2.0

Source Co-ordinates: x = -6.19 cm, y = 0.00, z = 8.50 cm. Vertical Component of Force Position is z = 0.00 For All Experiments.

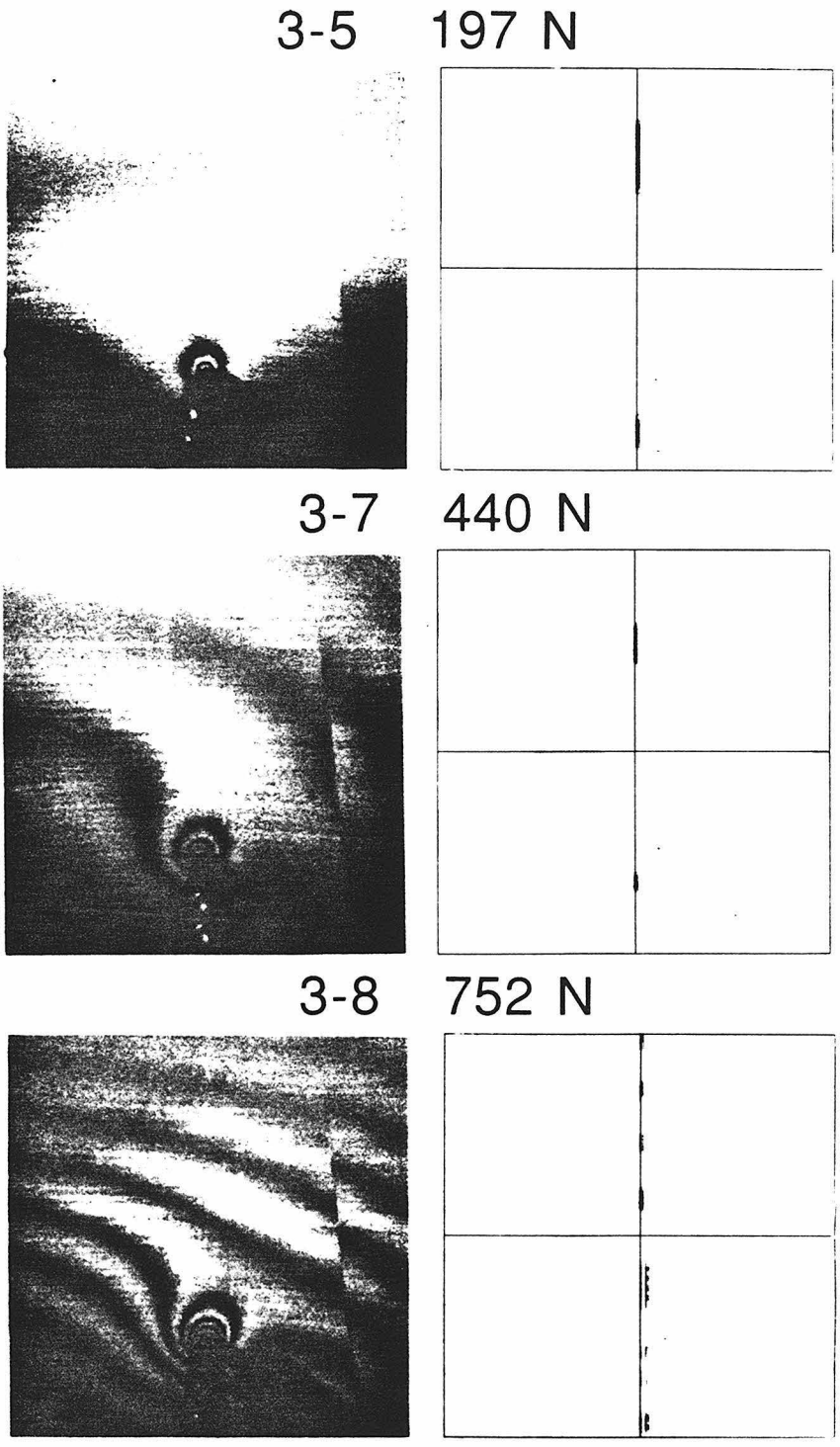

Figure 22). Field Results of Elastic Modulus Experiment in Horizontal Borehole in Mine Pillar. Existence of crack seen by discontinuous fringe pattern. Experiment at depth of 3.25 m and azimuth: θ of 90 ° from a horizontal vector pointing East (figure 14c).

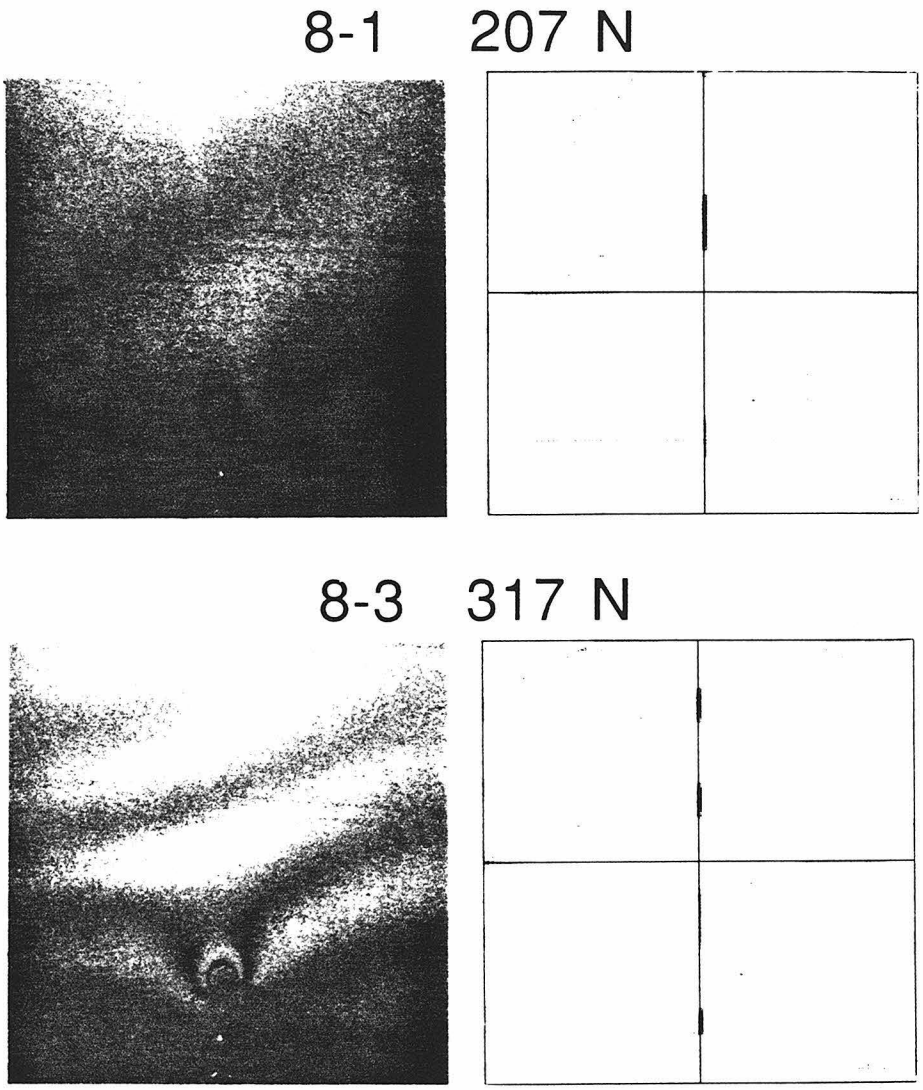

Figure 23). Borehole Elastic Modulus Experiment Results. Taken at a depth of 2.20 m and an azimuth of 135 °.

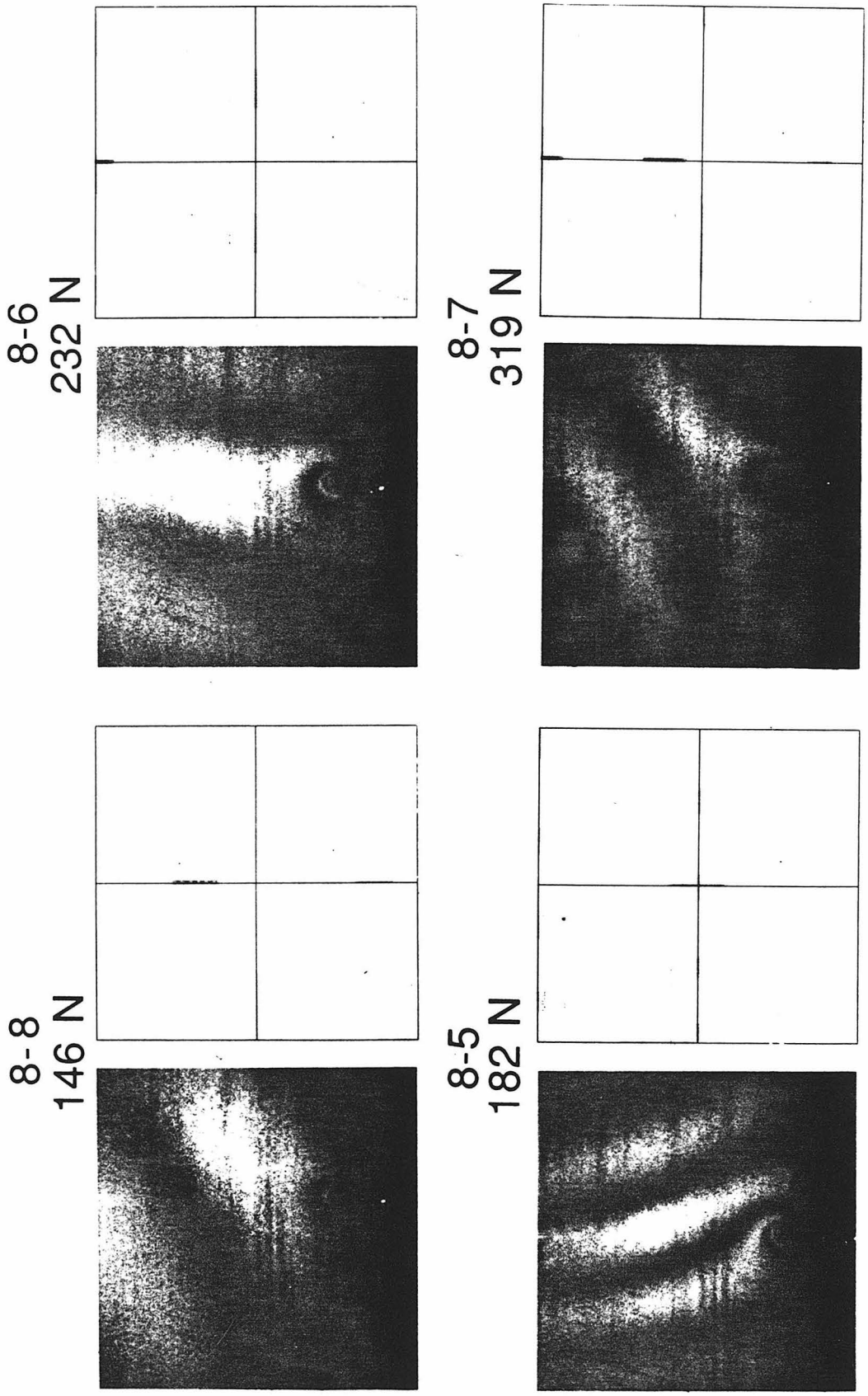

Figure 24). Borehole Elastic Modulus Experiment Results. Taken at a depth of 1.625 m and an azimuth of 180 °.

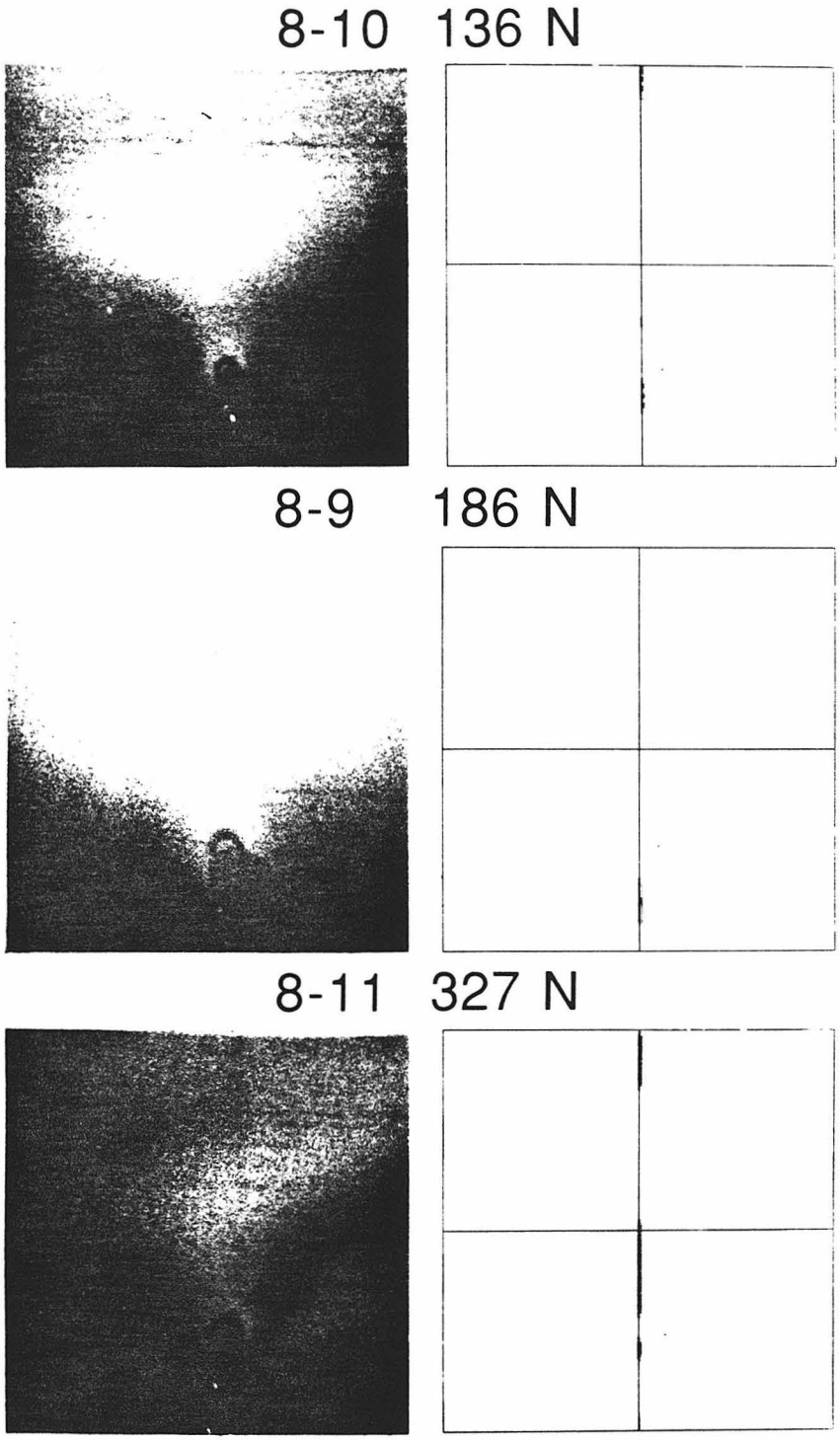

Figure 25). Borehole Elastic Modulus Experiment Results. Taken at a depth of 1.625 m and an azimuth of 135 °.

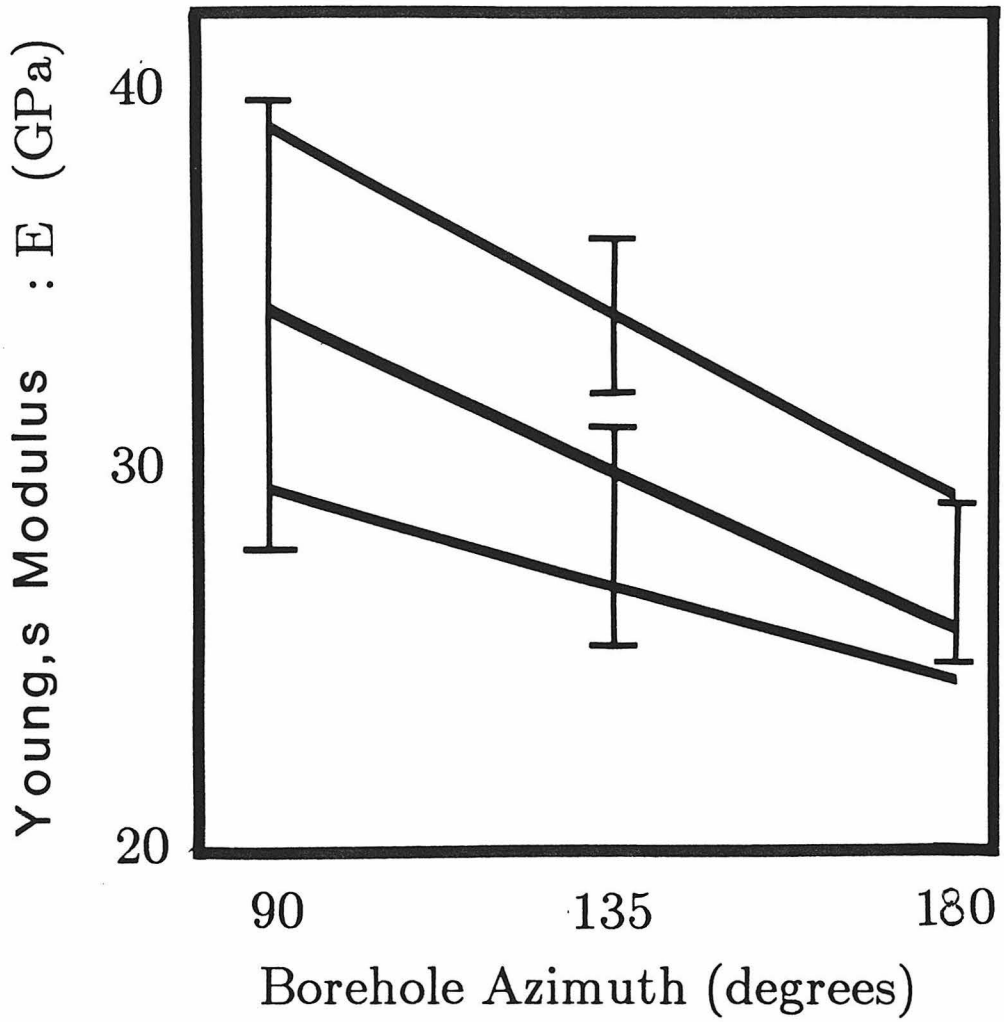

Figure 26). Borehole azimuthal dependence (θ) of holographically determined *in situ* Young's modulus.

where the uncertainties are determined from the extremum values. Equation 21 and its maximum and minimum values (plotted as lines in figure 26) suggests that the rock is less compressible normal to the bedding planes than parallel to them, in contrast to laboratory measurements in a calcareous, dolomitic marlstone of low kerogen content which give 41.0 GPa parallel and 25.2 GPa perpendicular to the bedding planes (Blair (1955)). A dependence of E on θ is not unexpected as the rock is visually anisotropic with well defined bedding planes.

A small crack in the rock mass is seen in the holograms taken at a depth of 3.25 meters into the borehole (Figure 22). Borehole television logging did not to find any cracks at this position. The crack is seen only by the discontinuous fringes in the hologram photographs; the borehole wall displacement field is disrupted across the crack. Although the applied force activates motion across the crack, it is sufficiently removed from the force application point to have little impact upon the induced Boussinesq displacements. These holograms point out an important advantage of the optical holographic technique over more conventional methods; the entire displacement field is recorded and data quality, is easily assessed by inspection of the holographic image. Defects in the rock mass may not be as readily apparent in methods which require the application of strain gauges to the material and could seriously affect results.

IN SITU STRESS TENSOR DETERMINATION

The complete farfield stress tensor (six components) was determined from five stress-relief holographic experiments taken at a single station 4 m within the borehole (figure 26). Although the in situ elastic modulus measurement above indicates that E should be independently determined for each stress-relief experiment, the fringe patterns were calculated (Smither et al., (1987)) assuming a value of E for the rock of 25 GPa (Schmitt et al., (1986)), a ν of 0.345 (Horino et al., (1982), and using the analytic theory presented above for stress-relief displacements. The determined nontrivial borehole wall stresses (table 8) are of unequal uncertainty due to the relative position of S with respect to P (figure 4) resulting in greater sensitivity of the fringe pattern to displacements parallel to the borehole circumference. Thus the magnitude of the hoop stress ($\sigma_{\theta\theta}$), which provides a significant fraction of the stress-relief borehole circumference displacements, is the best resolved; the borehole axial stress (σ_{hh}) with the greatest stress relief displacements parallel to the borehole axis has the largest uncertainty. Again, the uncertainties are estimated on the basis of the range of forward modelled synthetics which best match the observed fringe patterns.

Although only three holograms are needed at a given station, the present data at five azimuths (Table 8) have been combined via least squares for an overdetermined problem (Smither et al., (1987)) to find the complete stress tensor (Table 9). The vertical stress found was in agreement with earlier results of - 9.75 MPa (Schmitt et al., (1986b)) and a value of -11.2 MPa, predicted on the basis of the lithostatic pressure and

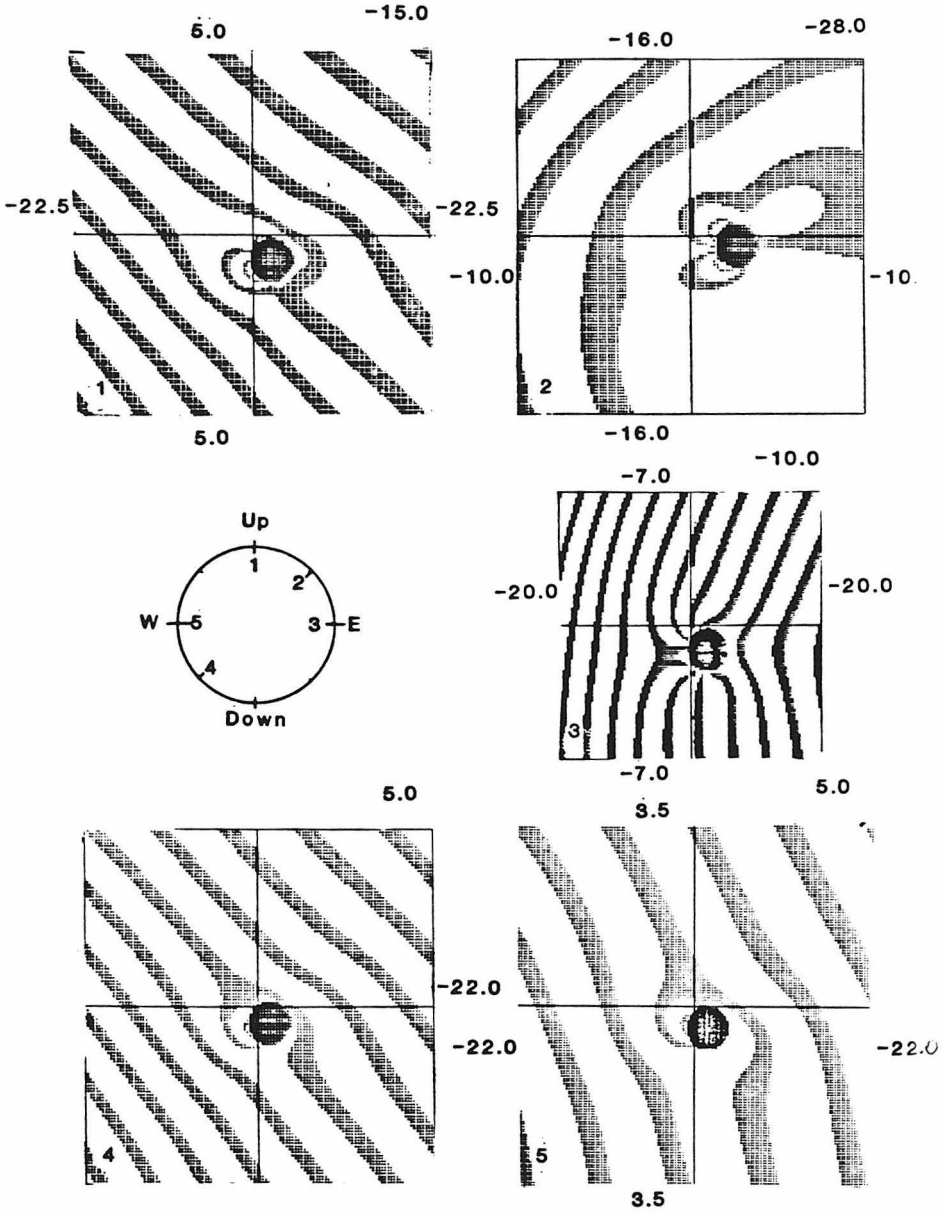

Figure 27). Best Forward Modelled Synthetic Holograms for Five Stress-Relief Experiments at a Single Station within the Borehole. Depth of experiments was 4 m, borehole azimuth of each hologram, numbered 1-5, shown for an observer facing North into the borehole. Determined borehole wall stresses (in MPa) and directions are indicated for each synthetic fringe pattern.

Table 8) Borehole Wall Stresses (in MPa)

Hologram	Azimuth	$\sigma_{\theta\theta}$	σ_{hh}	$\tau_{\theta h}$
1	90 °	-22.5 ± 2.5	5.0 ± 5.0	-15.0 ± 5.0
2	45 °	-10.0 ± 5.0	-16.0 ± 8.0	-28.0 ± 2.0
3	0 °	-20.0 ± 4.0	-7.0 ± 5.0	-10.0 ± 2.5
4	180 °	-22.0 ± 4.0	0.0 ± 4.5	5.0 ± 5.0
5	225 °	-22.0 ± 4.0	3.5 ± 6.5	5.0 ± 5.0

Table 9) Pillar Stesses (in MPa)

σ_{EW}	-10.06 $\pm$ 0.765
σ_{Vert}	-10.23 $\pm$ 0.996
σ_{NS}	-2.51 $\pm$ 2.48
$\tau_{EW-Vert}$	-0.64 $\pm$ 0.54
τ_{EW-NS}	7.76 $\pm$ 1.05
$\tau_{NS-Vert}$	-3.64 $\pm$ 0.713

Note: Negative stresses are compressive, positive stresses are tensile.

mine geometry by the relation:

$$(22)\quad \sigma_v = (dgh)A$$

where σ_v is the vertical compressive stress within the mine pillar, d is the average density of the rock above the mine pillar to the surface, g is the acceleration of gravity, h is the depth of the pillar, and A is the mine pillar stress concentration factor equal to the ratio of the area of mine roof supported by the pillar to the pillar area.

CONCLUSION

1) Laboratory tests of the holographic Young's modulus measurement by application of known normal forces to well defined metal samples confirmed the validity of the holographic method. Additionally, these tests demonstrated that translational displacements, introduced between holographic exposures and considered as noise, may readily be accounted in the forward modelling of fringe patterns based upon the Boussinesq theory of surface displacements. An advantage of the present technique is the straightforward data quality control obtained via viewing of the hologram; discontinuities in rock mass which have the potential of adversely affecting the results are easily seen in the fringe patterns.

2) Both elastic modulus and stress-relief field experiments have been conducted with a holographic borehole instrument deployed in a horizontal borehole in a mine pillar in the Mahogany formation of Garfield County, Colorado. Measured values of the in situ Young's modulus of the borehole wall rock are from 26.9 $\pm$ 2.9 GPa to 34.0 $\pm$ 2.0 GPa with a maximum uncertainty of 20 %. Laboratory holographic measurements on a

sample of rock taken from the same mine yielded a Young's modulus of 16.8 ± 2.8 GPa consistent with ultrasonic velocity measurements which gave values for the dynamic Young's modulus of 13.5 to 19.1 GPa for values of Poisson's ratio from 0.35 to 0.25. The complete farfield stress tensor was found from analysis of five holograms taken at different azimuths at a single hole depth of 4 m. The measured vertical stress of -10.2 MPa is in agreement with the predicted value of - 11.2 MPa obtained from the mine depth and geometry and rock density.

SYMBOLS USED IN STUDY

Symbol	Definition
x - y - z	Hologram cartesian co-ordinate system
O	Origin of x - y - z co-ordinate system
$\rho - \phi - \varsigma$	Induced displacements cylindrical co-ordinate system
O'	Origin of $\rho - \phi - \varsigma$ co-ordinate system
X - Y - Z	Borehole cartesian co-ordinate system
$r - \theta - h$	Borehole cylindrical co-ordinate system
E	Static compressive modulus of elasticity
E_D	Dynamic modulus of elasticity
ν	Poisson's ratio
$\sigma_{\theta\theta}$, σ_{hh} , $\tau_{\theta h}$	Borehole wall stresses
σ_{XX} , σ_{YY} , σ_{ZZ}	Farfield in situ stresses
τ_{XY} , τ_{XZ} , τ_{ZZ}	

--

σ_{EW} , σ_v , σ_{NS}	Farfield in situ stresses referred to east-west,
τ_{EW-v} , τ_{EW-NS} , τ_{v-NS}	vertical, and north-south directions
λ	Wavelength of laser light used in holograms
S	Source point of laser radiation
P	Object point (point on borehole wall)
P'	New position of object point P after displacement
P_{ij}	Grid point "P" for forward modelling algorithm
H	Viewing point on hologram
H_1, H_2, H_3	Hologram points required for inversion of
	fringe patterns to find displacement fields
k_1, k_2, k_3, k_4	Wave propagation vectors of magnitude $2\pi/\lambda$
Δk_1	$k_3 - k_1$
Δk_2	$k_4 - k_2$
$k_2{}^1$, $k_2{}^2$, $k_2{}^3$	Wave propagation vectors for inversion of
	fringe pattern to find displacement fields
K	Wave propagation sensitivity vector
K_1, K_2, K_3	Sensitivity vectors for inversion of
-	fringe pattern to find displacement fields
R	Position vector between S and H
r_1	Position vector between S and P
r_3	Position vector between P and H
Φ	Phase change for ray path (S-P-H) of first exposure
Φ'	Phase change for ray path (S-P'-H) of second exposure
L	Displacement vector of point P to P'
-	between holographic exposures

--

L_{ij}	Displacement vector of grid point P_{ij}
T	Translational displacement component of L
I_{ij}	Induced (stress-relief or normal force)
-	displacement component of L
N	Dark fringe order
N_{ij}	Dark fringe order for point P_{ij}
M	Closest integer value to N or N_{ij}
U_ρ, U_ϕ, U_ς	Induced displacement components of I_{ij}
U_T	Magnitude of I_{ij}
F	Normal applied force
F/E	Ratio of normal applied force to modulus of elasticity
V_p	Ultrasonic compressional wave velocity
d	Density
g	Acceleration of gravity
h	Depth of mine pillar
A	Stress concentration factor of mine pillar

REFERENCES

Aleksandrov, E.B., and Bonch-Bruevich, A.M., Investigation of Surface Strains by the Hologram Technique, *Sov. Phys. Tech. Phys.*, **12**, pp. 258-265, 1967.

Bass, J.D., Schmitt, D.R., and Ahrens, T.J., Holographic In Situ Stress Measurements, *Geophys.J.R.astr.Soc.*, **85**, pp. 13-41, 1986.

Bieniawski, Z.T., Determining Rock Mass Deformability: Experience from Case Histories, *Int.J.Rock Mech.Mining Sci. & Geomech. Abst.*, **15**, pp. 237-247, 1978.

Bieniawski, Z.T. and Van Heerden, W.L., The Significance of In Situ Tests on Large Rock Specimens, *Int.J.Rock Mech.Mining Sci. & Geomech.Abst.*, **12**, pp. 101-113, 1975.

Blair, B.E., Physical Properties of Mine Rock: Part III, *U.S.Bur.Mines, Invest.Rept.*, **5130**, pp. 69, 1955.

Bock, H., Foruria, V., and Lequerica, R., A New Stress Relief Concept for In-situ Stress Measurements in Rock and Its Implementation in two Recoverable Stressmeters, in *Proc., Fourth Australia - New Zealand Conference on Geomechanics, Perth*, 1984.

Carmichael, R.S., *Handbook of Physical Properties of Rocks, Volume II*, CRC Press,Inc., pp. 345, 1982.

Cohn, S.N., *Holographic In-Situ Stress Measurement in Geophysics, Ph.D. thesis*, California Institute of Technology, pg. 159, 1983.

Crampin, S., Seismic-wave propagation through a cracked solid: polarization as a possible dilatancy diagnostic, *Geoph.J.Roy. astr.Soc.*, **53**, pp. 467-496, 1978.

Crampin, S., McGonie, R., and Bamford, D., Estimating Crack Parameters from Observations of P-wave Velocity Anisotropy, *Geophysics*, **45**, pp. 345-360, 1980.

Ennos, A.E., Measurements of In-Plane Surface Strain by Hologram Interferometry, *J.Sci.Instrum., Ser. II*, **1**, pp. 731-746, 1968.

Dhir, S.K., and Sikora, J.P., An Improved Method for Obtaining the General Displacement Field from a Holographic Interferogram, *Exp.Mech.*, **12**, pp. 323-327, 1972.

Flaman, M.T., and Manning, B.H., Determination of Residual-Stress Variation with Depth by the Hole-Drilling Method, *Exp.Mech.*, **26**, pp. 205-207, 1986.

Goodman, R.E., Van, T.K., and Heuze, F.E., The Measurement of Rock Deformability in Boreholes, *Proc.10th Symp.Rock Mech., AIME*, pp. 523-555, 1970.

Haimson, B.C., and Fairhurst, C., *In-situ* Stress Determination at Great Depth by Means of Hydraulic Fracturing, in *Rock Mechanics - Theory and Practice, Proceedings, 11 th Symposium on Rock Mechanics, Berkeley*, ed. Somerton,W.H., pp. 559-584, Soc.Mining Engr. of AIME, New York, 1970.

Hiramatsu, Y. and Oka, Y., Stress Around a Shaft or Level Excavated in Ground with a Three-Dimensional Stress State, *Mem.Fac.Engng., Kyoto*, **24**, pp. 56-76, 1962.

Horino, F.G. and Hooker, V.E., Mechanical Properties of Cores Obtained from the Unleached Saline Zone, Piceance Creek Basin, Rio Blanco County, Colorado, *U.S.Bur.Mines, Invest.Rept.*, **8297**, pp. 21, 1978.

Hubbert, M.K. and Willis, D.G., Mechanics of Hydraulic Fracture, *AIME Trans.*, **210**, pp. 153-168, 1957.

Jaeger, J.C., *Rock Mechanics and Engineering, 2nd Edition*, Cambridge University Press, Cambridge, 1979.

Jaeger, J.C. and Cook, N.G.W., *Fundamentals of Rock Mechanics*, Chapman and Hall, London, pp. 593, 1979.

Jones, R. and Wykes, C., *Holographic and Speckle Interferometry*, Cambridge University Press, Cambridge, pp. 330, 1983.

Leeman, E.R., The 'Doorstopper' and Triaxial Rock Stress Measuring Instruments Developed by the C.S.I.R., *J.South.African Inst.Min.Met.*, **69**, pp. 82-114, 1969.

Leeman, E.R. and Hayes, D.J., A Technique for Determining the Complete State of Stress in Rock Using a Single Borehole, *Proc. 1st Cong.Int.Soc.Rock.Mech., Lisbon*, **2**, pp. 17-24, 1966.

Leith, E.M and Upatnieks, J., Reconstructed Wavefronts and Communication Theory, *J.Opt.Soc.Am.*, **52**, pp. 1123-1130, 1962.

Leith, E.M. and Upatnieks, J., Wavefront Reconstruction with Diffused Illumination and Three-Dimensional Objects, *J.Opt.Soc. Am.*, **54**,

pp. 1295-1301, 1964.

McGarr, A. and Gay, N.C., State of Stress in the Earth's Crust, *Ann.Rev.Earth Planet.Sci.*, **6**, pp. 405-436, 1978.

Meyer, T.O. and McVey, J.R., NX Borehole Jack Modulus Determination in Homogeneous, Isotropic, Elastic Materials, *U.S.Bur.Mines, Rept.ofInvest.*, **7855**, pg. 50, 1974.

Nelson, D.V. and McCrickerd, J.T., Residual-Stress Determination Through Combined Use of Hologaphic Interferometry and Blind- Hole Drilling, *Exp.Mech.*, **26**, pp. 371-378, 1986.

Nur, A., Effects of Stress on Velocity Anisotropy in Rocks with Cracks, *J.Geophy.Res.*, **76**, pp. 2022-2034, 1971.

Rendler, N.J. and Vigness, I., Hole Drilling Strain-gage Method of Measuring Residual Stresses, *Exp.Mech.*, **6**, pp. 577-586, 1966.

Schmitt, D.R., Smither, C.L, Ahrens, T.J., and Jensen, B.L., Holographic Measurement of Elastic Moduli, *Proc. 27 th U.S. Symp. on Rock Mechanics, The University of Alabama, Tuscaloosa*, pp. 185-191, 1986a.

Schmitt, D.R., Smither, C.L., Ahrens, T.J., and Jensen, B.L., Borehole In-situ Holographic Stress and Elastic Moduli Measurements, *Proc., The Society of Exploration Geophysicists, 56 th Annual Meeting, Houston*, pp. 9-12, 1986b.

Schuman, W. and Dubas, M., *Holographic Interferometry*, Springer-Verlag, Berlin, pp. 194, 1979.

Smither, C., Schmitt, D.R., and Ahrens, T.J., Analysis and Modeling of Holographic Measurements of *In Situ* Stress, Submitted to *Int.J.Rock Mech. Min.Sci. & Geomech.Abstr.*, 1987.

Sollid, J.E., Translational Displacements vs Deformational Displacements in Double Exposure Holographic Interferometry, *Opt.Communs.*, **2**, pp. 282-288, 1969a.

Sollid, J.E., Holographic Interferometry Applied to Measurements of Small Static Displacements of Diffusely Reflecting Surfaces, *Appl.Opt.*, **8**, pp. 1587-1595, 1969b.

Stesky, R.M., Compressional and Shear Velocities of Dry and Saturated Jointed Rock: A Laboratory Study, *Geophy.J.Roy.astr. Soc.*, **83**, pp. 239-262, 1985.

Swolfs, H.S., Handin, J., and Pratt, H.R., Field Measurements of Residual Strain in Granitic Rock Masses, In *Advances in Rock Mechanics, Proc. 3rd Cong.Int.Soc.Rock.Mech.*, **2a**, pp. 563-568, 1974.

Thomsen, L., Weak Anisotropic Anisotropy, *Geophysics*, **51**, pp. 1954-1966, 1986.

Timoshenko, S.P. and Goodier, J.N., *Theory of Elasticity, 3rd Edition*, McGraw-Hill Book Co., New York, pg. 567, 1970.

Vest, C.M., *Holographic Interferometry*, Wiley, New York, 1979.

Weast, R.C., *CRC Handbook of Chemistry and Physics*, CRC Press, Cleveland, pg. 2388, 1977.

Windes, S.L., Physical Properties of Mine Rock: Part II, *U.S. Bur.Mines, Invest.Rept.*, **4727**, pp. 37, 1950.

Chapter 2.

SHOCK TEMPERATURES IN SILICA GLASS

ABSTRACT

Greybody temperatures and emittances of silica glass under shock compression between 10 and 30 GPa are determined. Observed radiative temperatures are higher than computed continuum temperatures for shock compressed fused quartz; however, below $\sim$ 26 GPa observed emittances are $<$ 0.02. This suggests that fused quartz deforms heterogeneously in this shock pressure range, as has been observed in other minerals. Between 10 and 16 GPa, radiative temperatures decrease from 4400 K to 3200 K, above 16 GPa to 30 GPa greybody temperatures of $\sim$ 3000 K with low emittances are observed. The emittances increase with pressure from 0.02 to 0.9. The pressure range from 10 to 16 GPa coincides with the permanent densification region while the 16 to 30 GPa range coincides with the mixed phase region along the fused quartz Hugoniot. The differing radiative behaviors relate to these modes of deformation. Based upon shock recovery experiments and a proposed model of heterogeneous deformation under shock compression, the temperatures associated with low emittances in the mixed phase region probably represents the melting temperature of the high pressure phase. Above 20 GPa to 30 GPa the melting temperature of stishovite would therefore be 3000 K $\pm$ 200 K and almost independent of pressure. The effect of pressure on melting relations for the system SiO_2-Mg_2SiO_4 are considered together with the proposed stishovite melting curve

and suggest that the maximum solidus temperature within the mantle is $\sim$ 2370 K at 12.5 GPa and $\sim$ 2530 K on 20.0 GPa. Using the proposed stishovite melting temperatures (T_m) and reasonable upper mantle temperatures (T), the effective viscosity, which is a function of the homologous temperature: T_m / T, appears to remain nearly constant from 600 to 200 km depth in the Earth.

INTRODUCTION

The temperatures of silica glass subject to shock pressures between 10 and 30 GPa were investigated by observation of shock induced radiative thermal emissions. In this pressure range brittle materials deform heterogeneously under shock compression with the formation of localized zones of intense deformation and high temperatures surrounded by relatively undamaged cooler material. The study of these zones which are referred to as hot spots, shear bands, or microfaults is important because they play a role in the shock deformation process in minerals and particularly in shock production of glassy and high pressure polymorphs. Spectra of light emitted from silica glass in this pressure range reveal the temperature, and to some extent, the density of these microfaults. Observed temperatures relate to the deformation occurring and, based on models of heterogeneous deformation, constrain the melting curve of minerals with pressure.

Quartz was chosen as a candidate for study for two major reasons. The first is the importance of quartz as both a crustal and a model mantle mineral. High pressure phases of quartz have been discovered at sites of large meteorite impacts and of explosive volcanism, these phases are

presumably produced by the action of shock waves. Knowledge of the shock effects in quartz provide information for deducing the effects of large impacts on the Earth.

Although, estimates of whole Earth composition based upon cosmochemical abundances suggest that approximately 35% by weight of the entire Earth, core included, is SiO_2. In the mantle, free SiO_2 most likely does not exist as it is incorporated into the high pressure phases of pyroxene, olivine, and garnet. However, since the lower mantle is ofter described in terms of high pressure phase oxide mixtures (Al'tshuler et al., (1965)), a better understanding of the high pressure properties of SiO_2 yields information pertinent to the study of mantle constitution and dynamics.

Secondly, SiO_2 has been extensively studied in both high pressure static and dynamic experiments with high pressure polymorphs coesite (Coes (1953)) and stishovite (Stishov and Popova (1961)) having room pressure densities of 2.92 Mg/m^3 and 4.29 Mg/m^3 (Kuskov and Fabrichnaya (1987)), respectively. Except for the discovery of coesite in kimberlites and deep-seated metamorphic rocks, the only natural occurrances of these minerals are at the sites of major impacts on the Earth's surface, suggesting formation from quartz by shock wave. Evidence (reviewed by Stoffler (1972,1974)) demonstrate that shock damage in quartz is nonuniformly distributed; shock compression in quartz below 35 GPa is a heterogeneous process. Observation of the radiative temperatures of fused SiO_2 under shock compression will aid in further understanding of shock processes in brittle minerals.

BACKGROUND

We consider the microscopic effects of the passage of a shock wave through a solid brittle medium with emphasis on silica glass. Covalently bonded minerals of geophysical interest undergo brittle deformation according to Grady (1980). Shock deformation of partially covalently minerals, such as SiO_2, MgO, Al_2O_3, and $CaCO_3$, is characterized by all or some of the following features: 1) the existence of large Hugoniot elastic limits, 2) fluid-like release from high pressure, 3) nonequilibrium Hugoniot in the mixed phase region for minerals with a primary co-ordination phase change, and 4) the observation of heterogeneities in minerals recovered from a shock wave experiment.

The Hugoniot elastic limit (HEL) is the shock pressure at which dynamic yielding occurs; shock compression below the HEL is an elastic process, plastic deformation occurs above the HEL (Davison and Graham (1979)). This results in a first shock propagating slightly faster than the longitudinal sound speed (elastic precursor) with magnitude equal to the HEL followed by a slower second shock described as a plastic wave with amplitude of the final shock pressure. Two wave shock structures have been reported in shock compression experiments on both alpha and fused quartz to 75 GPa (Wackerle (1962), Fowles (1967), Sugiura et al., (1981)). They attribute the two-wave structure, observed over a wide pressure range, to anomalously high HEL in quartz which has been measured by a variety of methods to range from 5.5 to 15 GPa for differing crystal orientations (Fowles (1967), Graham (1973)). Similarly the HEL of fused quartz ranges from 8.8 to 9.8 GPa (Wackerle (1962), Barker and Hollenbach (1970),

Sugiura et al., (1981)).

In contrast to metals which retain a finite shear strength above the HEL, evidence was presented in the above studies indicating that silica loses its rigidity above the elastic limit, i.e., the Hugoniot of quartz collapses to predicted static compression curves. Silica compressed above the elastic limit may be characterized as fluid-like. Graham (1973) demonstrated a substantial loss of strength within 10 ns after passage of the shock wave for stresses well above the HEL. Thus quartz shocked above the HEL behaves hydrostatically.

This fluid-like behavior is best observed during the release of a shock compressed quartz crystal from high pressure. Grady et al., (1975) measured sound velocities from rarefaction wave profiles on the Hugoniot for a quartz rock (novaculite). The observed low sound velocities implied a fluid-like response behind the shock front. From these results and the work of others, they suggested that dynamic yielding in quartz involved adiabatic shear processes accompanied by partial melting behind the shock front.

The Hugoniot of alpha quartz (Figure 1, filled symbols) supplies evidence for the quartz to stishovite phase transition. In the shock wave velocity-particle wave velocity plot of figure 1b, shock velocities remain constant over a range in U_p of 1.4 to 2.25 km/s. Although Wackerle (1962) and Fowles (1967) reported data for both the elastic precursor and the plastic shock, figure 1 shows results for only the second or plastic wave. Trunin et al., (1970) supplies information on one arrival only which may lead to the discrepancy between the data sets at

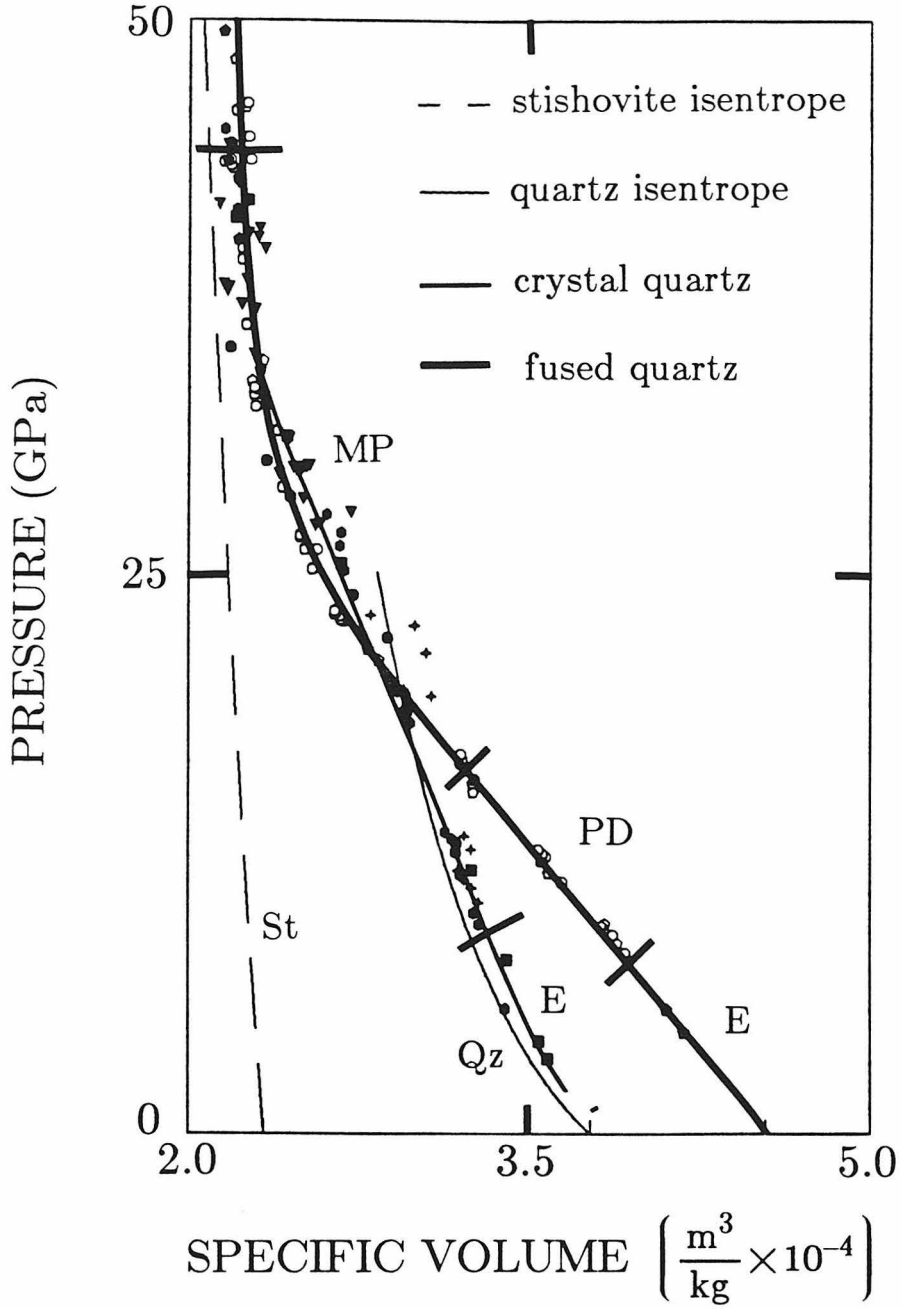

Figure 1a) Shock pressure vs volume data for crystalline (filled symbols) and fused (open symbols) quartz. Static compression curves for alpha quartz (Qz) (intital density = 2.65 g/cm^3, bulk modulus = 37.1 GPa, bulk modulus pressure derivative = 6.0) and stishovite (St) (initial density = 4.288 g/cm^3, bulk modulus = 305 GPa, bulk modulus pressure derivative = 4.5) (Kuskov and Fabrichnaya (1987))calculated with Birch-Murnahan finite stain theory are shown for comparison. The fused quartz and crystalline quartz Hugoniots co-incide above 30 GPa suggesting that they are in the same phase state. Key to regions along Hugoniot: E - elastic deformation below HEL, PD - permanent densification of fused quartz, MP - mixed phase, St - stishovite, T - stishovite to melt transition under homogeneous shock melting, HM - homogeneous shock melting.

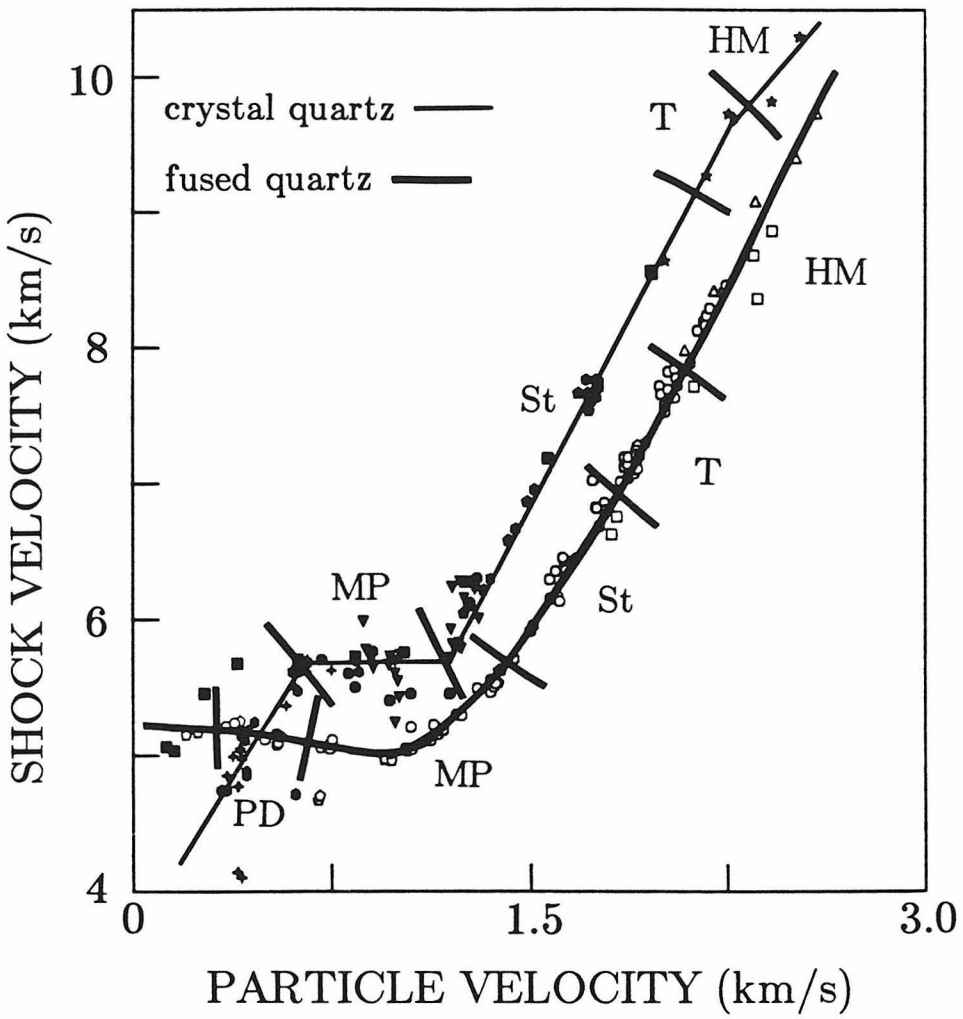

Figure 1b) Shock wave velocity vs particle velocity for crystalline and fused quartz. Symbols have same meaning as in a). Fused quartz data from Lyzenga et al. (1983) - (open triangles), Jackson and Ahrens (1979) - (open squares), Wackerle (1962) - (open pentagons), and Marsh (1980) - (open circles). Crystal quartz data from Lyzenga et al. (1983) - (filled 5 point star), Ahrens and Rosenberg (1968) - (filled inverted triangle), Grady et al. (1974) - (filled circle), Fowles (1967) - (filled 4 point star), Marsh (1980) - (filled pentagon), Trunin et al. (1971) - (filled square), and Wackerle (1962) - (filled hexagon).

Up $<$ 1.4 km/s. All data sets display a region of constant shock velocity characteristic of a phase change in alpha quartz as labelled in figure 1. This range of particle velocity is equivalent to the pressure range of 14.4 GPa to approximately 38 GPa and is hereafter referred to as the mixed phase region of the Hugoniot of alpha quartz. Within this range the incompressibility of quartz increases dramatically as is seen in figure 1a of shock pressure vs. specific volume.

Wackerle (1962) first suggested that the produced high pressure phase was stishovite, or a like-co-ordinated liquid. Stishovite, with a six-fold co-ordination structure similar to rutile, was first reported at 16 GPa and 1473 K (Stishov and Popova (1961)). Based on the comparable large density increase found in both the static and shock wave experiments, and on the fact that the shock wave and static pressures of phase initiation were similar (approximately 14 GPa) McQueen et al., (1963) suggested shock production of stishovite occurred. They further suggested that the short time scale of the shock experiments prohibited large stishovite crystal growth and that instead a fluid with a short order stishovite-like structure was created.

Between the HEL ($\sim$ 8.8 to 9.8 GPa) and approximately 16.0 GPa, fused silica undergoes a permanent densification as evidenced by shock recovery (Wackerle (1962), Arndt et al., (1971)), and profiles in time of particle velocity (Sugiura et al., (1981)). Gibbons and Ahrens (1971), however, find increased refractive index, indicative of permanent densification, in recovered fused quartz shocked between 10 and 30 GPa. This permanent densification has been studied in static

compression experiments on fused quartz (Bridgman and Simon, (1953)) and is attributed to a rearrangement and tilting of the SiO_2 tetrahedra (Cohen and Roy (1961), MacKenzie (1963), Arndt and Stofller (1969), Grimsditch (1984), and Hemley et al., (1986)). This densification is observed to reverse upon annealing of both shock and statically compressed fused quartz to pressures in excess of 10 GPa.

Above 16 GPa the Hugoniot of fused quartz passes through a region in which the material may be in a mixed phase with stishovite. The inherent properties of shocked fused quartz have not yet been determined. Note that at approximately 30 GPa and above the Hugoniots of both crystalline and fused quartz converge providing compelling evidence that both are at the same phase state at higher shock pressures. This suggests the fused quartz mixed phase region may contain some stishovite. Sugiura et al., (1981) suggest compression above 16 GPa is that of a high-density silica glass, they find little evidence for production of stishovite below 22 GPa. However, in recent reshock and release experiments on fused quartz (Chhabildas and Grady (1983)) at 13 GPa and 21 GPa stishovite transformation was found to initiate at 13 GPa and to progress to a more fully mixed phase state at 20 GPa.

A release wave defines the thermodynamic path taken by a shock compressed material upon isentropic decompression. The release wave path in the pressure-volume plane yields estimates of the zero pressure density of the high pressure phase. Experiments on crystal quartz (Ahrens and Rosenberg (1968), Grady et al., (1974), Chhabildas and Grady (1984), Chhabildas and Miller (1985), and Podurets et al., (1976))

indicate: 1) The transformation to the high pressure phase occurs within the shock front, little further transformation occurs during the remainder of the compression, 2) the release path for quartz shocked to less than 10 to 15 GPa returns to the initial density, 3) the release path of quartz shocked into the mixed-phase region (15 to 34 GPa) follows a path indicative of mixed quartz-stishovite, the ratio of stishovite increasing proportionally with pressure, and upon release to less than 8 GPa, reversion to a lower density approximately that of crystal quartz, and 4) above 50 GPa the release path is essentially that of the high pressure phase until a released pressure of 5 to 8 GPa is reached whereupon a reversion to a lower pressure phase with a density of $\sim 2.2\ Mg/m^3$ occurs.

The most compelling evidence for the transformation to the high pressure phase are the recovered phases from both natural impact craters and laboratory shock experiments. Abundant coesite and smaller amounts of stishovite have been detected in rocks subjected to high shock pressures during meteorite impacts (Chao (1960,1962), Kieffer (1971)). Shock laboratory production of stishovite from quartz in single crystals, novaculite, and sandstone was reported by DeCarli and Milton (1965). The lack of coesite in their recovered samples is not understood. Kleeman and Ahrens (1973) pointed out that the direct transformation from quartz to stishovite should occur at a pressure of ~7.5 GPa and not 14 GPa and identified stishovite from quartz shocked above 9.0 GPa; increasing quantity was found with increasing pressure until at pressures above 23.4 GPa the production of stishovite decreased with more glass produced. A single shot with fused quartz at 16.6 GPa yielded the largest

percentage of stishovite. Most recently, Ashworth and Schneider (1985) report bands of polycrystalline stishovite, producing rings in electron diffraction, associated with densified glass in shock recovered quartz.

Mashimo et al., (1980) suggest that stishovite is not readily observed in shock recovered material due to its rapid annealing to fused quartz at the elevated residual temperatures upon shock release. Above 600 K stishovite readily transforms to fused quartz at standard pressure (Dachille et al., (1963)).

MODEL OF HETEROGENEOUS DEFORMATION IN QUARTZ

Anan'in et al., (1974a) examined recovered crystal quartz and found the material in a plane perpendicular to the direction of shock propagation was broken up into 5-20 micron blocks separated by layers of quartz glass. The plane parallel to the shock front revealed larger (100-200 micron) blocks. Anan'in et al., (1974a) suggested that above the HEL compression occurs by fragmentation into blocks which then move relative to one another. A consequence of this movement is frictional heating and melting at the surfaces of the blocks. They further speculated that increases in atomic co-ordination can occur rapidly within the melt and therefore the melted component, which increases with increasing pressure, accounts for the mixed phase region of the quartz Hugoniot.

Anan'in et al., (1974b) in shock recovery experiments on fused quartz found that it undergoes deformation similar to that of crystalline quartz. As in crystal quartz, they note that at shock pressures above the HEL, the fused quartz splits into blocks separated by layers of melt.

The blocks are thus subjected to hydrostatic compression and are permanently densified. The melt takes on the characteristics of a high pressure phase. Moreover, Wackerle (1962) found that fused quartz shocked to 25 GPa transformed to fine particles with densities in the 2.4-2.5 Mg/m^3 range whereas material shocked to higher pressures had the normal 2.2 Mg/m^3 density in agreement with earlier results (Gibbons and Ahrens (1971), Arndt et al., (1971)).

Gratz (1984), consistent with an earlier study (Schall and Horz (1977)), observed planar microfaults of thickness of $\sim$1 to 10 microns oriented at 45 to 55 degrees to the shock wave propagation direction in approximate agreement with the orientation of the maximum resolved shear stress with respect to the shock propagation direction (Jones and Graham (1971)). These microfaults are filled with glass; displacement across these microfaults is seen by offset of broken rutile needles separated by a microfault. The observations of steps emerging from the surface perpendicular to the shock direction in scanning electron micrographs (Ashworth and Schneider (1985)) are consistent with the production of microfaults characterized by relative displacements.

The microfaults are to be distinguished from shock lamellae (Stoffler (1972,1974)), the latter occur in sets of 4 to 12 and are narrow planes of lengths to 50 microns and thicknesses of 0.5 to 500 nm (Gratz (1984)). Additionally, the shock lamellae have an orientation nearly perpendicular to the shock propagation direction and appear to be crystallographically controlled. Lamellae are apparently formed at the same time as the microfaults.

Alternatively, a series of tensile cracks, also filled with glass, and oriented perpendicular to the shock propagation direction are observed. These are features of the release of the material from high pressure. These tensile remnants of the shock recovery experiment are smaller than the microfaults and the glass they contain appears to have originated in the microfaults and then migrated into the connected tensile cracks upon release (Gratz, personal communication).

Wackerle (1962) found that fused quartz shocked to near 50 GPa were recovered in single pieces. Furthermore, samples composed of several initially divided pieces of fused quartz were recovered as a continuous mass.

Ashworth and Schneider (1985) shock loaded quartz along the **a** axis to pressures of 30 GPa and although they make no mention of microfaults (Anan'in et al., (1974), Gratz (1984)) they note regions of patchy glass which could be microfaults when the differences in magnification of the studies are considered. Numerous glass filled lamellae of thicknesses less than 1 micrometer and a crystallographically controlled orientation, as seen by Gratz (1984), parallel to the shock direction were noted. The amorphous material within the lamellae is similar to that produced by the irradiation of quartz (metamictization).

The above observations are compelling evidence for the proposed model of heterogeneous deformation as shown in figure 2a. In the figure, a shock wave is shown propagating towards the right in a brittle material. The shock compressed region on the left has experienced a heterogeneous compression and is comprised of blocks of solid material separated by layers of melt.

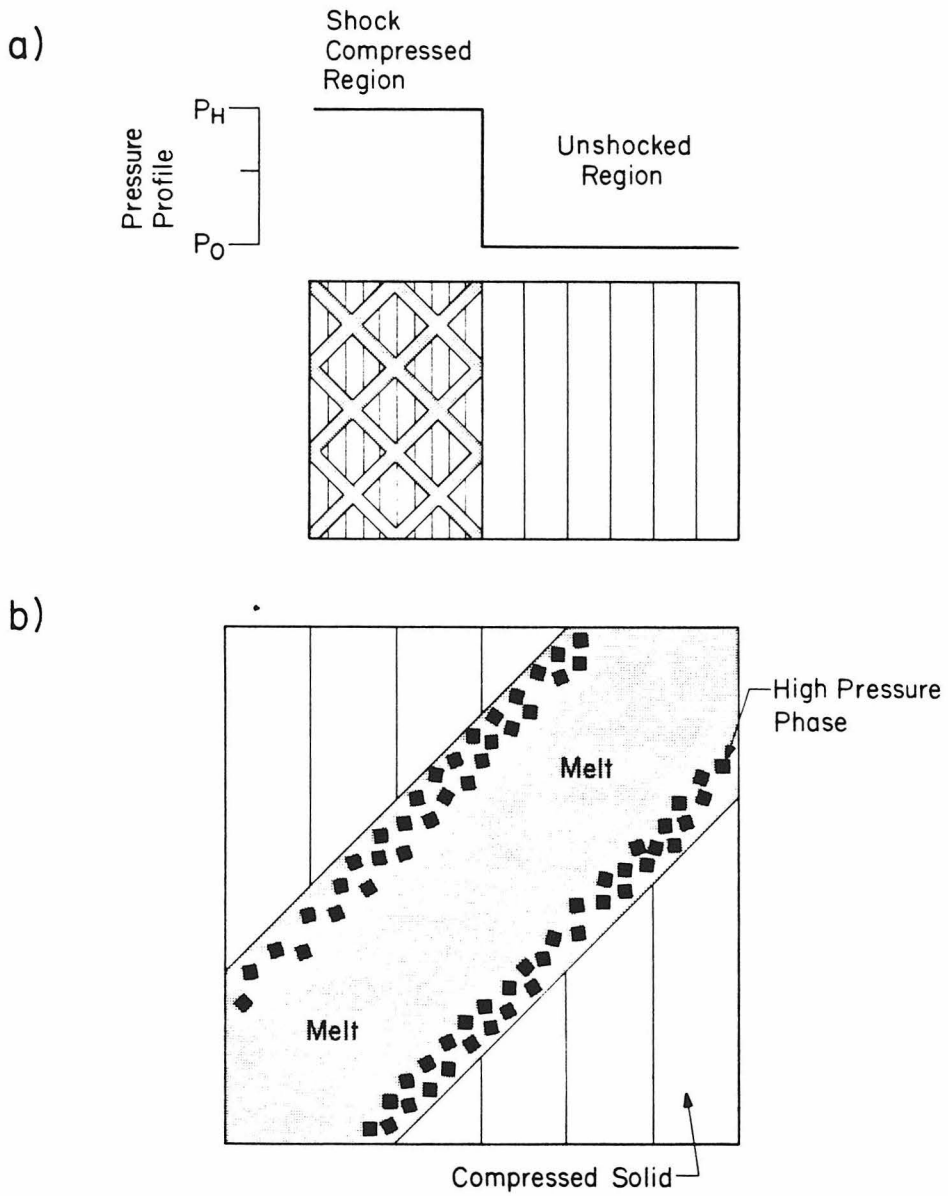

Figure 2) Schematic of model of heterogeneous shock compression in brittle materials, after Grady (1980, 1975). a) Large scale view with shock wave of magnitude P_h propagating towards the right in a sample. Behind the shock wave material is compressed and heterogeneous yeilding has occured on planes at 45 degrees to the direction of shock propagation. b) Microfault containing melt and surrounded by undamaged material. Upon cooling high pressure solid phase nucleates.

The melt layers are oriented at 45 degrees to the direction of shock propagation (i.e., the direction of maximum shear stress) The solid blocks are subjected to volumetric compression due application of a hydrostatic stress via the regions of melt.

Figure 2b displays an enlarged view of a microfault. Most of the material within the confines of the microfault is melt of pressure dependent co-ordination. As cooling of the microfault occurs, high pressure phase begins to nucleate (black squares) within the region of melt (light grey region) reminiscent of the observations of Ashworth and Schneider (1985). In quartz, a change in co-ordination from 4 to 6 would most easily and rapidly be accomplished in a melt. Further, this nucleation of high pressure solid phase in equilibrium with the melt may constrain the temperature of the microfault to that of the fusion curve. The observed temperatures from mixed phase regions along the Hugoniot would be the melting or liquidus temperature of the equilibrium solid phase.

At a high enough shock pressure the volumetric density of these melted or sheared zones becomes large relative to the volume of the undamaged blocks such than rapid equilibration of the shocked material takes place on a time scale much less than the shock wave experiment. At this point the deformation would appear much more homogeneous (Grady (1977,1980)).

This model explains the loss of shear strength behind the shock front, and the phase transformation by shock wave in quartz.

EXPERIMENTAL

Experiments were conducted on the 40 mm powder gun at the Seismological Laboratory of the California Institute of Technology in a configuration similar to that of Kondo and Ahrens (1983). Planar shock waves were generated within the samples by impact of metal flyer plates (table 1, figure 3) with velocities of up to 2.5 km/s. The sample shock compression resulted in heating such that significant visible light was emitted. This light propagates through the unshocked portion of the sample and is directed outside of the experimental chamber to a spectrometer whose output is recorded using a charge coupled device (EG&G Princton Applied Research optical multichannel analyzer, model 1257) to give a visible spectrum. This digitally recorded spectrum is then used to determine a greybody temperature for the material while it is under shock compression. In addition to the spectrometer a photodiode, which supplies a record of intensity vs. time and a framing camera (Schmitt et al. (1986)), to supply short exposure images of the sample under shock compression, are used.

Cylindrical fused silica samples (T12 Optosil 1, Amersil Corp.) of 2.54 cm diameter and 0.6 cm thickness were purchased prepolished to an optical grade flatness. The specific gravity of the samples was measured to an accuracy of 0.02% by the Archimedean method. Silver was vacuum-deposited on one face to mask light flashes on arrival of the shock wave at the driver-sample interface due to gaps (Kondo and Ahrens (1983)). The silver-coated sample face was mounted to a metal driver plate (table 1) (polished to a mirror finish with a final corundum grit of 0.3 micron),

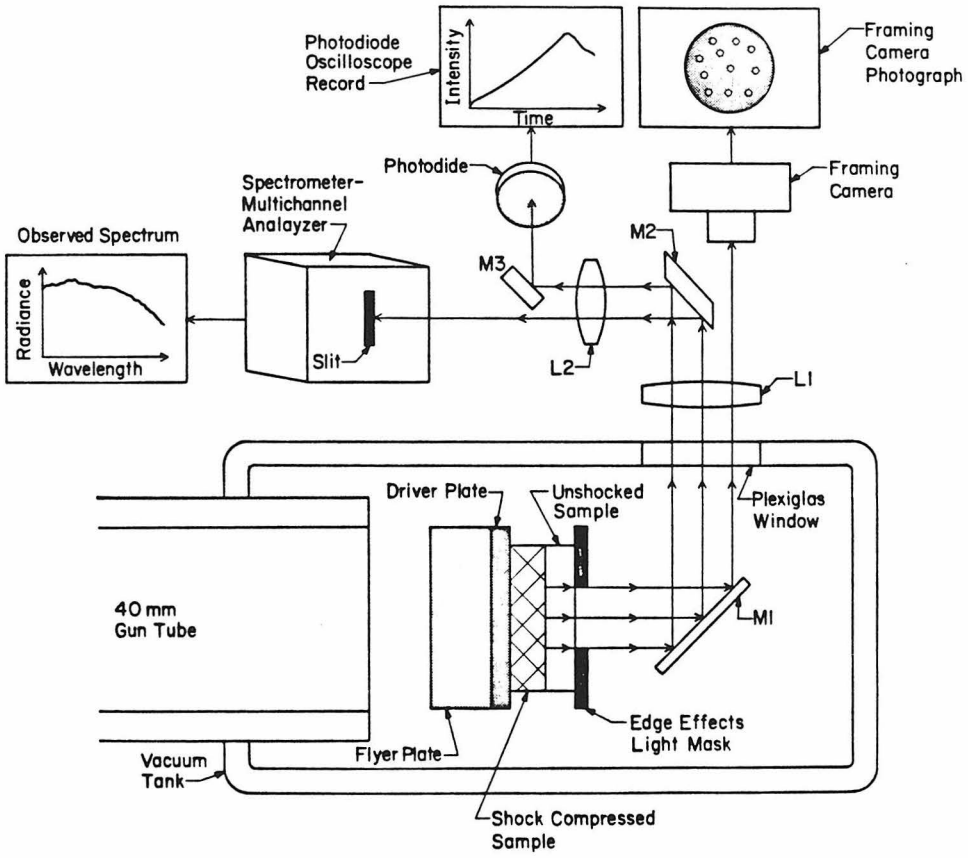

Figure 3) Shock radiation experimental configuration.

Table 1: Experimetal Parameters

Shot #	Flyer	Driver	Flyer Vel. (km/s)	Pressure (GPa)	Temp. (°K)	Emittance	I.F.E.	Field
634	Al_a	Al	1.44 ± 0.02	9.8±0.2	4390±500	0.012±0.004	none	1
635	W	W	1.543 ± 0.02	15.2±0.3	3590±200	0.0047±0.0005	small	1
684	W	Mg	2.471 ± 0.05	25.7±0.7	2190±200	0.056±0.006	small	3
685	W	Mg	1.995 ± 0.03	20.0±0.4	2950±200	0.0058±0.0006	severe?	2
686	W	Mg	1.750 ± 0.02	17.4±0.4	[b]	-	-	-
687	W	Mg	1.400 ± 0.02	13.7±0.3	3240±200	0.0025±0.0003	moderate	1
688	Al	Mg	1.488 ± 0.02	10.0±0.2	4210±200	0.0064±0.0006	severe	1
689	W	Mg	2.492 ± 0.05	25.8±0.6	2930±200	0.055±0.006	small	2
691	W	Mg	2.295 ± 0.04	22.2±0.6	3270±200	0.0035±0.0004	small	2
695	W	Mg	2.086 ± 0.03	21.0±0.5	2620±200	0.0023±0.0002	small	2
708	W	Al	2.455 ± 0.05	29.3±0.7	2030±200	0.780±0.08	moderate	3
709	W	Al	2.346 ± 0.04	27.5±0.6	2400±200	0.041±0.004	none	2
710	W	Cu	2.492 ± 0.05	29.6±1.0	2930±200	0.030±0.003	severe	2
711	W	Al	2.507 ± 0.04	30.2±0.5	2883±200	0.022±0.002	small	2

I.F.E. : Interface Flash Effect

[a] : W = Tungsten, Al = Aluminum, Cu = Copper, Mg = Magnesium.

[b] : No detected light emitted

with epoxy or phenyl salicylate. An opaque mask with an hole of inside diameter of 13.0 mm was centered on the sample free surface to eliminate light emissions from regions near the edges of the sample.

Shock pressures were determined with the impedance match method (Duvall and Fowles (1963)) and using the Hugoniot data for fused quartz, magnesium, aluminum, copper, and tungsten in Marsh (1980) and the experimentally determined projectile velocities.

Light recorded by the optical multichannel analyzer passes through a series of photocathode intensifiers which are controlled by a high voltage pulse; the detector may thus be gated to record spectra on time scales as short as 100 ns. Gate times during an experiment are typically 300 to 500 ns and normally occur while the shock wave is near the center of the sample.

A portion of the beam is focused by a series of lenses into a TRW framing camera which images the sample during shock propagation. The framing camera allows up to three 100 to 500 ns exposures to be taken during propagation of the shock wave in the sample.

During setup of each experiment, the image of the fused silica sample is focused on the spectrometer slit (figure 4). Magnification of the image was approximately 1:1, however this varied due to movement of the experiment chamber between successive experiments resulting in slightly different light paths which changed the focus. The image of the unmasked region of the sample was $\sim$15 mm in diameter and covered the slit with a 13 mm height.

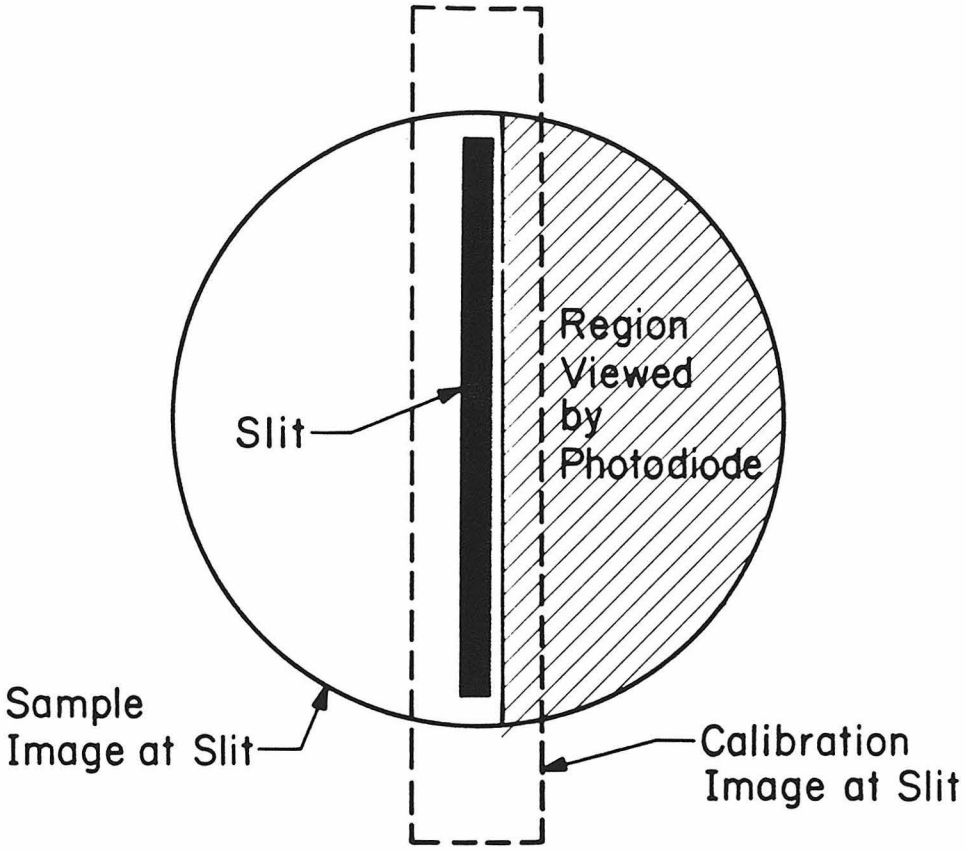

Figure 4) View of spectrometer slit. Images of fused quartz sample and filament of calibration ribbon lamp shown. Light accumulated by spectometer during experiment originates only within the region of the sample which is focused directly over the slit. Region of sample to right of slit is reflected by a mirror to the photodiode.

Calibration of the spectrometer was accomplished before each experiment with a standard of spectral radiance (Optronics model number 550, lamps IR-30 and IR-159). As small variations in current affect the radiance of the lamp considerably, current to the lamp was monitored to ± 0.03 %.

Values of the calibration lamp spectral radiance were supplied by the manufacturer (Figure 5). However, the spectrometer required a value of spectral radiance over each of the 500 channels representing a different wavelength. Appropriate values were supplied by a fit of the given calibration lamp radiances to the linearized Planck greybody radiation law. The curves through the known radiances represent the equivalent grey-body function for the lamp, this function was used in the reduction of the spectrometer data. Although the maximum error introduced by use of the fits shown is below 2% over the most sensitive spectrometer wavelengths (550 to 750 nm).

During calibration, all controllable variables (light path, spectrometer delay (200 to 700 ns), and spectrometer gate (300 to 500 ns)) were identical to those of the experiment in order to reduce errors. A camera shutter set at 1/500 second exposure was used to trigger the system and to limit the amount of dark current into the spectrometer. Based upon tests using longer shutter open times it was found dark current radiance errors are less than 5% of the magnitude and independent of wavelength.

Light levels from the fused quartz samples during an experiment were less than 25% the level of light emitted by the calibration lamp. Since the CCD spectrometer had a limited light level sensitivity range, low

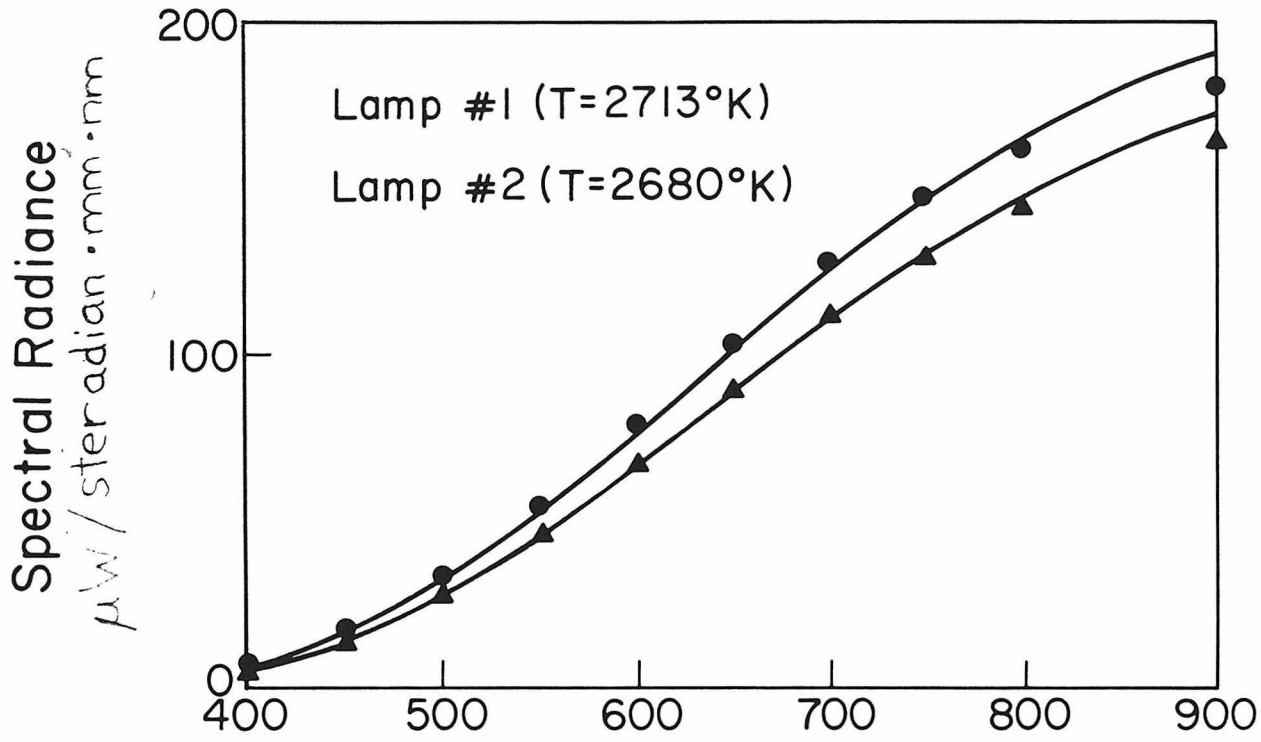

Figure 5) Spectral radiances of calibration lamps (triangles: lamp #1 (2680 K), circles: lamp #2 (2713 K).

light levels resulted in large signal to noise problems, whereas high light levels could saturate the detector. Co-ordination of the calibrated light level with the expected light level for an experiment involved maximizing the amount of light arriving at the spectrometer during calibration with neutral density filters. The spectral characteristics of the neutral density filters were carefully accounted for by taking a number of tests through various light paths through the system.

The wavelength function of the spectrometer was determined by use of common spectral lines (Weast (1982)) of hydrogen (656.2 nm), helium (587.6 nm, 667.8 nm, 706.5 nm), oxygen (777.3 nm, 844.6 nm) and mercury (578.6 nm, 546.1 nm) . Low intensities from the standard gas lamps made calibration at experimental gating times ($\sim$ 300 ns) difficult, several tests were conducted for each lamp to reduce the signal to noise ratio. The accuracy of the wavelength function changed with wavelength and was inversely proportional to the density of standard lamp lines used in a given region of the spectrum; the maximum uncertainty encountered in the positioning of the spectral lines was approximately 3 nm. Curvature of the vidicon intensifiers results in a variation of the wavelength interval per spectrometer channel, on average, the range was $\sim$ 0.8 nm/channel.

A single photodiode was used to obtain a record of light intensity vs. time during the shock wave experiments. Output of this photodiode was simultaneously recorded with on oscilloscopes and a LeCroy transient recorder which samples data every 10 ns. The photodiode and the spectrometer view different but adjacent areas of the sample (figure 4).

DATA REDUCTION

The observed number of counts at each spectrometer channel is proportional to the time-integrated intensity of the emitted radiation at the given wavelength. To obtain a spectra, the raw data in counts were multiplied by a conversion factor relating spectral radiance intensity to number of counts derived from the calibration procedure (figure 6). The temperatures of the standard lamps are approximately 2700 K, calibration factor thus is very sensitive to errors towards the red and violet ends of the observed spectral range.

The determination of shock temperatures from the observed spectra assumes: 1) the material radiates as a Planck greybody, 2) the emissivity of the material under shock compression is independent of wavelength, 3) the temperature range of the experiment is such that a Wien's law spectral radiance distribution may be used. Assumptions 1) and 2) are based on the shape of the observed fused quartz spectra which, in general, are indicative of a thermal radiation: no line or band emissions are noted and the spectra monotonically decrease from the infrared to the ultraviolet. The complete Planck greybody function is given by:

$$(1)\quad R = \frac{\epsilon c_1}{\lambda^5(exp\,(c_2/\lambda T) - 1)}$$

where R is the spectral radiance, ϵ is the emittance, T is the temperature of the emitting body, λ is the given wavelength, and c_1 and c_2 are constants with values of $1.191 \cdot 10^{-16} Wm^2/steradian$ and 0.01438 mK, respectively. For assumption (3) it is presumed that the simplification of equation (1), given by the Wien's greybody function:

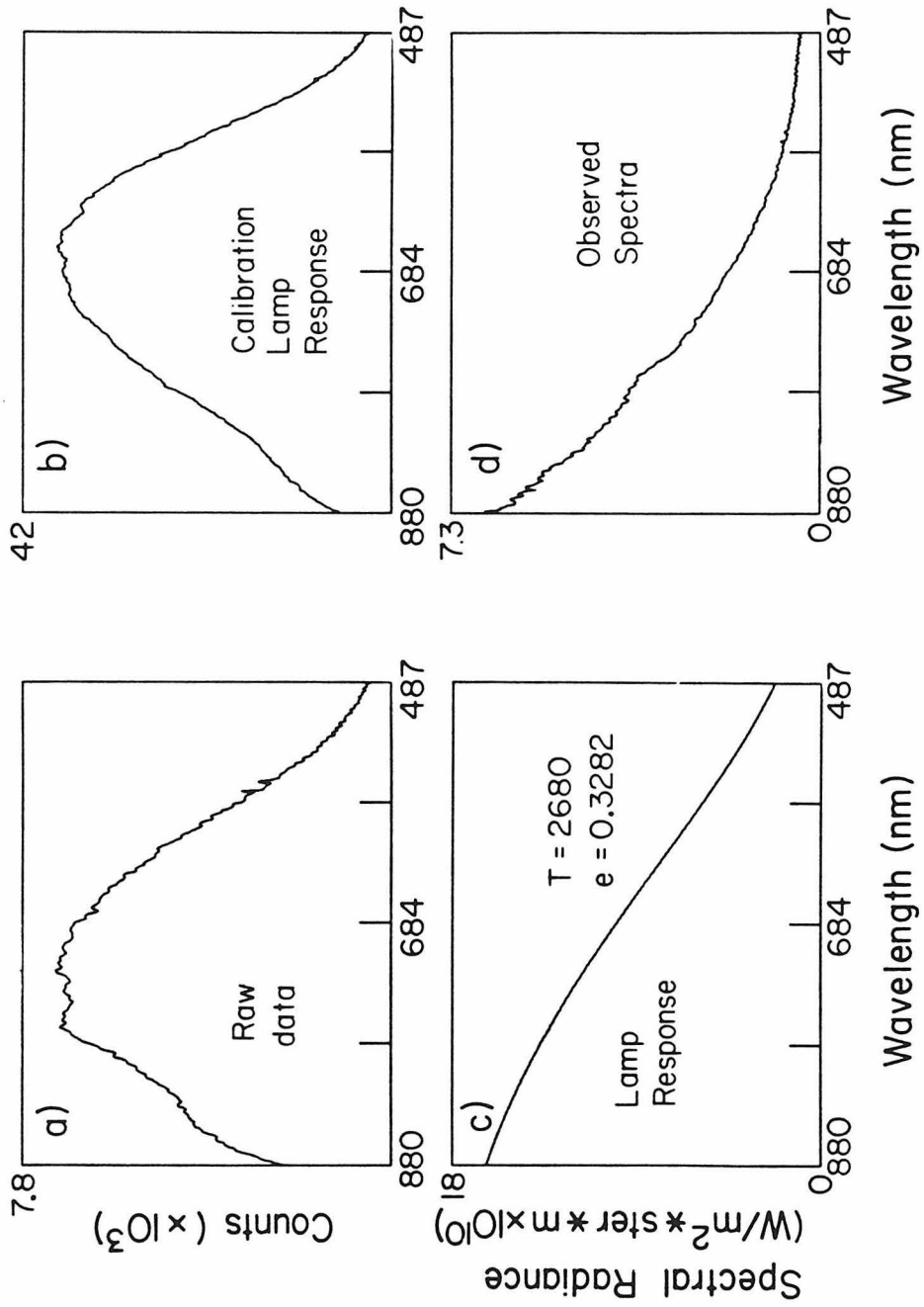

Figure 6) a) Raw data: response of spectrometer during experiment. b) Spectrometer response to calibration lamp. c) Output of spectral radiance lamp. d) Observed spectra derived from a), b), and c).

$$(2)\quad R = \frac{\epsilon c_1}{\lambda^5 exp\,(c_2/\lambda T)}$$

in order to facilitate linearization of the formula is justified. Errors introduced by use of this formula are larger for higher temperatures and longer wavelengths; however, for the temperature range encountered in the experiments (2000 K to 4500K) and for the range in wavelengths (450 nm to 880 nm) the maximum error is less than 2% and for most cases many orders of magnitude smaller. As a check on the validity of the linearized results, an iterative least squares routine was implemented with the full Planck grey-body formula; results were always within 50 K of the linearized version.

The linearized Wien's law is given by:

$$(3)\quad ln\,(\frac{c_1}{R\,\lambda^5}) = \frac{c_2}{\lambda}\frac{1}{T} - ln\,(\epsilon).$$

where $ln\,(c_1/(R\,\lambda^5)$ and c_2/λ are the dependent and independent variables and a standard linear regression is then applied to find the slope 1/T and intercept $-ln\,(\epsilon)$ which yield temperature and emittance, respectively.

Since data at either wavelength range extreme has a larger uncertainty due to the reasons mentioned above, each datum is relatively weighted by its corresponding raw data count (see figure 6). The raw data function supplies a reasonable weighting scheme as it inherently accounts for both sensitivity of the system and spectral regions of maximum emission (i.e., lowest signal to noise ratio).

Standard deviations derived from the least squares routine yield temperature uncertainties on the order of $\pm$ 30 K. This is unrealistically small and on the basis of experience with the data suggest an

uncertainty of ± 200 K is more appropriate for the observed temperatures.

RESULTS

Figure 7 shows the spectra observed for x-cut crystalline shots #611 and #615 at shock pressures of 10.6 and 7.6 GPa respectively. The shape of the spectra are greatly influenced by a non-thermal emission centered at approximately 500 nm and cannot be fit to a greybody curve. The shape of the spectra, however, is indicative of broadened line emission superimposed upon a greybody spectra. Since the determination of shock temperatures was the primary motivation for this study and X-cut quartz does not lend itself, in this pressure range, to accurate temperature determinations due to the large non-thermal component of the spectra, further experiments on crystalline quartz were discontinued.

Brannon et al., (1983) reported spectral and imaging data for shocked crystalline quartz from 6 to 26 GPa. They also observed a nonthermal bandlike spectral feature with peaks at 400 and 600 nm. Present observations displayed an emission at 500 nm, the difference in data may be due to the higher wavelength resolution of this study. The source of this nonthermal radiation in unclear and may be related to photoluminescence or cathodoluminescence (Brannon et al., (1983)). Since no nonthermal component was observed from fused quartz, the 500 nm emission of crystalline quartz may be tied to breaking of long range order within the crystal or the inherent piezeoelectricity of quartz.

Another proposed explanation may be related to the production of the shock lamellae in crystalline quartz. Because fused quartz is a

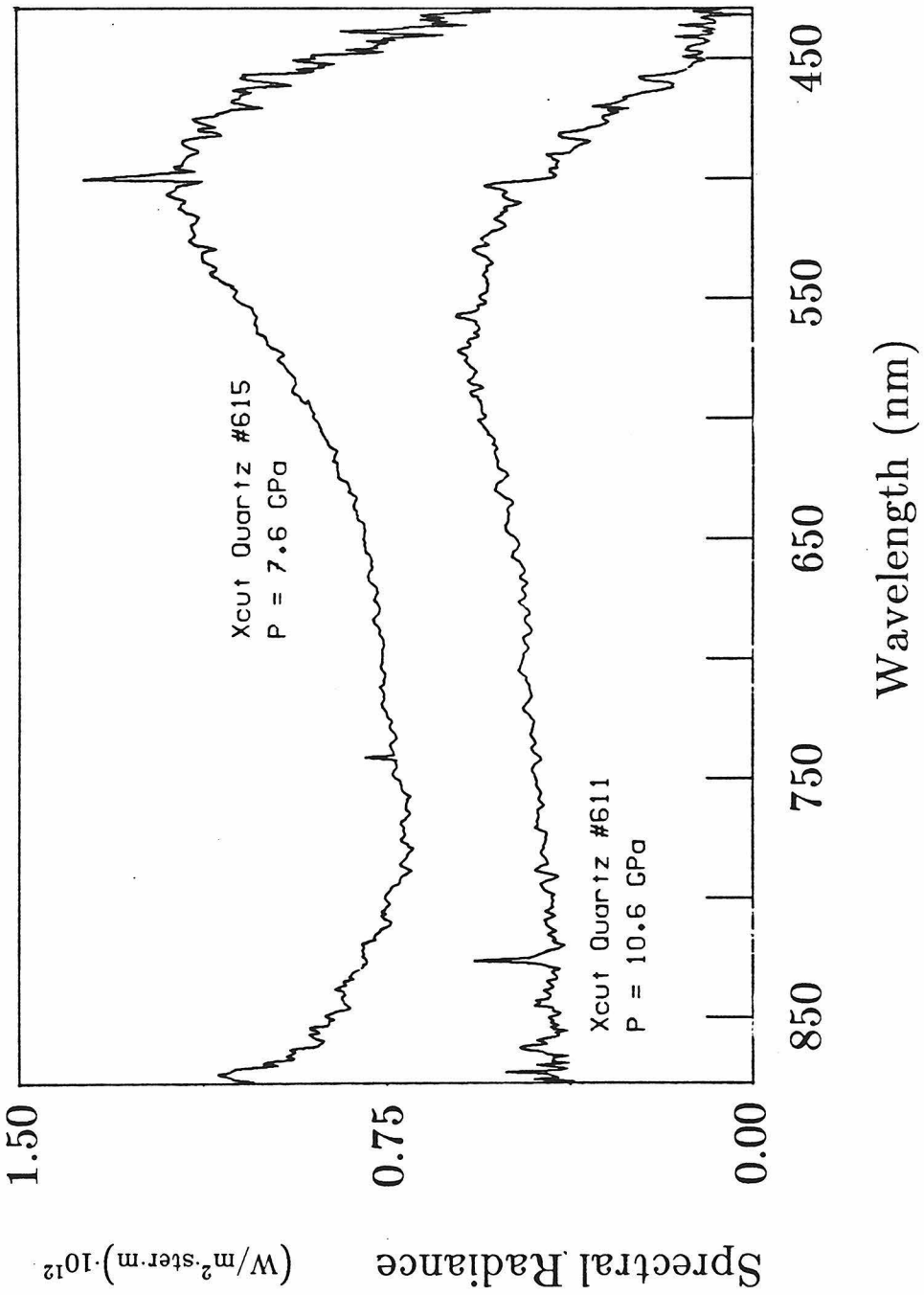

Figure 7) Spectra observed for shots #611 and #615 for x-cut crystalline quartz. A large non-thermal component to the spectra centered near 500 nm makes temperature determination infeasible.

homogeneous, isotropic, amorphous material, it has no structural preferences and perhaps no shock lamellae are produced in fused quartz. Conceivably, thermal radiation may be associated with the shear heating within microfaults (in both fused and crystal quartz) and nonthermal radiation could arise from the formation of the diaplectic glass within the shock lamellae (in crystal quartz only).

The framing camera photograph consists of two exposures of shot #634 under shock compression, each of 100 ns duration and separated by 300 ns. The first exposure was initiated 50 ns after entry of the shock wave into the sample. The corresponding photodiode record for #634 (Figure 8) commences with zero intensity at the entry of the shock wave into the fused quartz sample and builds in a linear fashion with time. This furnishes convincing evidence that the bright spots observed in the photograph originated within the compressed fused quartz and not at the driver-sample interface.

Figures 9, 10, and 11 and table 1 present the spectra and related data for the present experiments on fused quartz. These spectra are indicative of thermal radiation, no line or band emissions are observed as in crystalline quartz. The best fit Planck greybody function is plotted through each spectrum.

Figure 9 are the spectra obtained in the pressure range from 10 to 16 GPa which is the region of permanent densification along the fused quartz Hugoniot. Unexpectedly, the temperatures are highest in this lowest of pressure ranges studied. Shots #688 and #634 display a marked drop in intensity at lower wavelengths (less than 450 nm). This is attributed to the poor

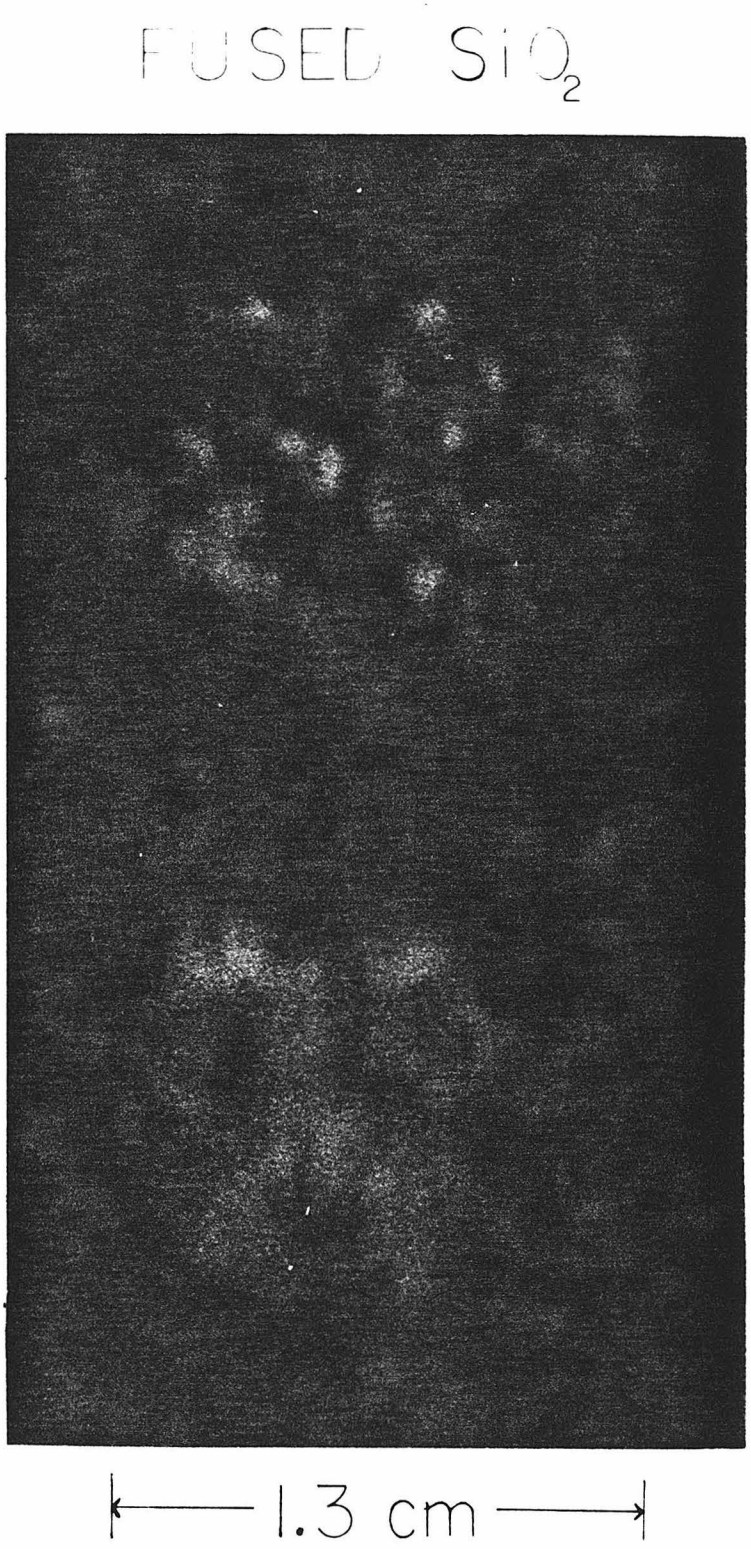

Figure 8) Framing camera photograph for fused quartz shot #634 at 9.8 GPa. Two exposures each of 100 ns duration and separated by 300 ns are shown.

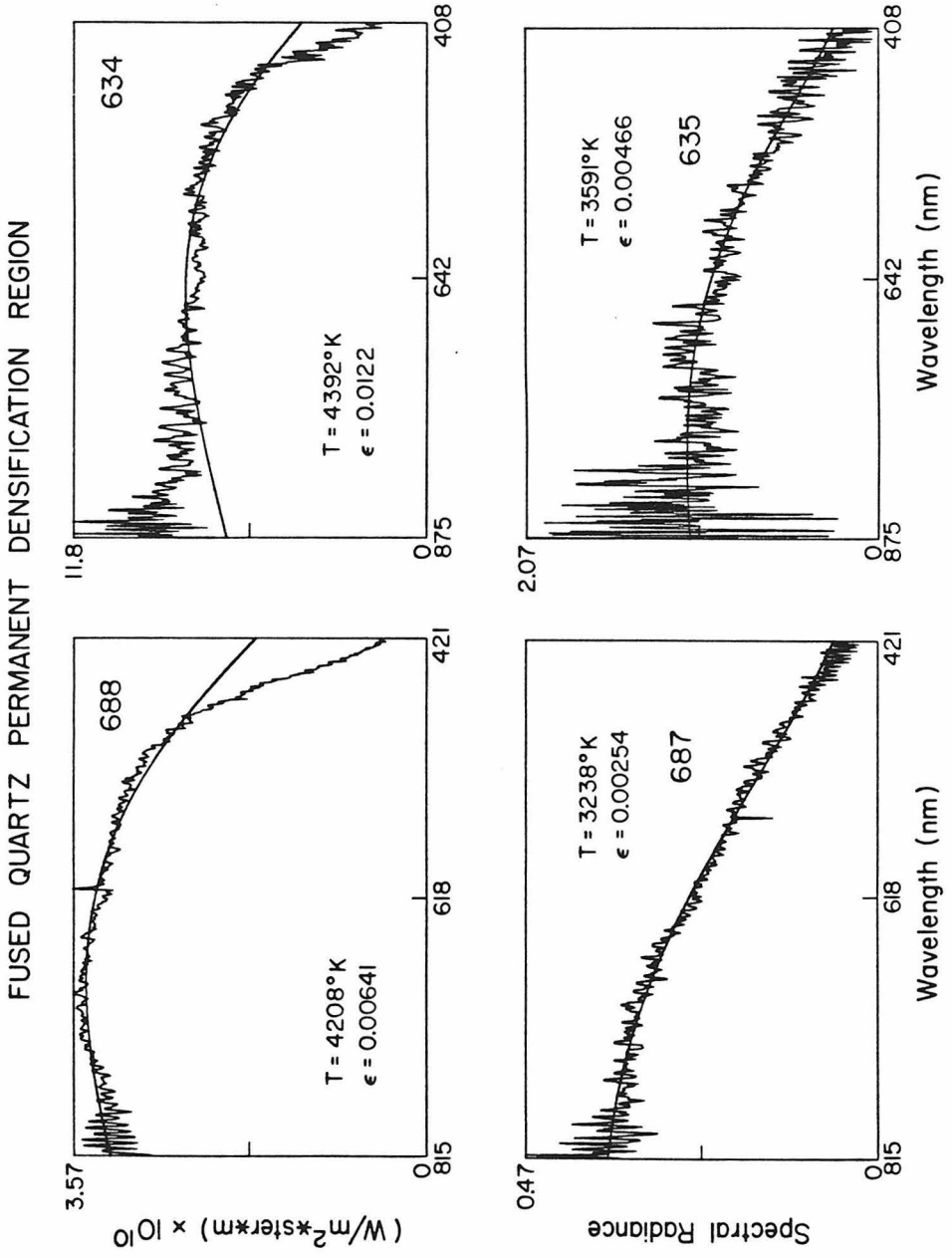

Figure 9) Observed spectra from fused quartz shocked between 9.8 and 16 GPa (Field #1 in figure 13a and figure 14).

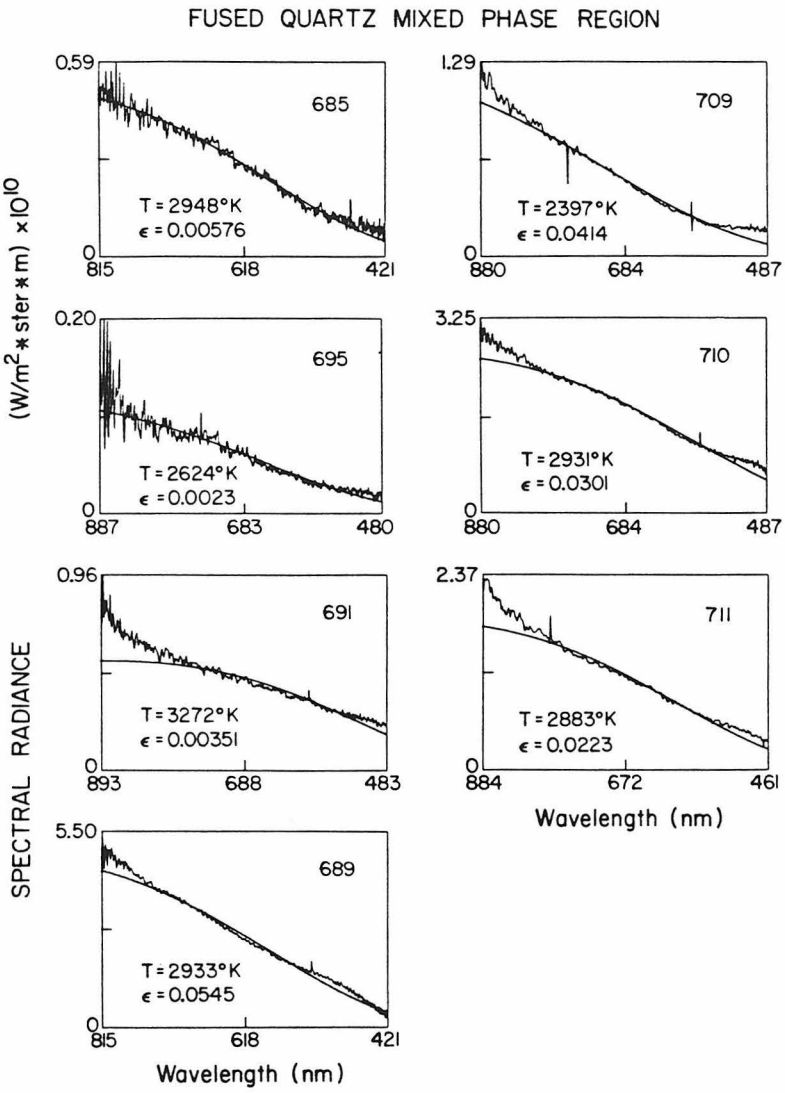

Figure 10) Observed spectra from fused quartz shocked in the mixed phase region (20 to 30 GPa) (Field #2 in figure 13a and figure 14).

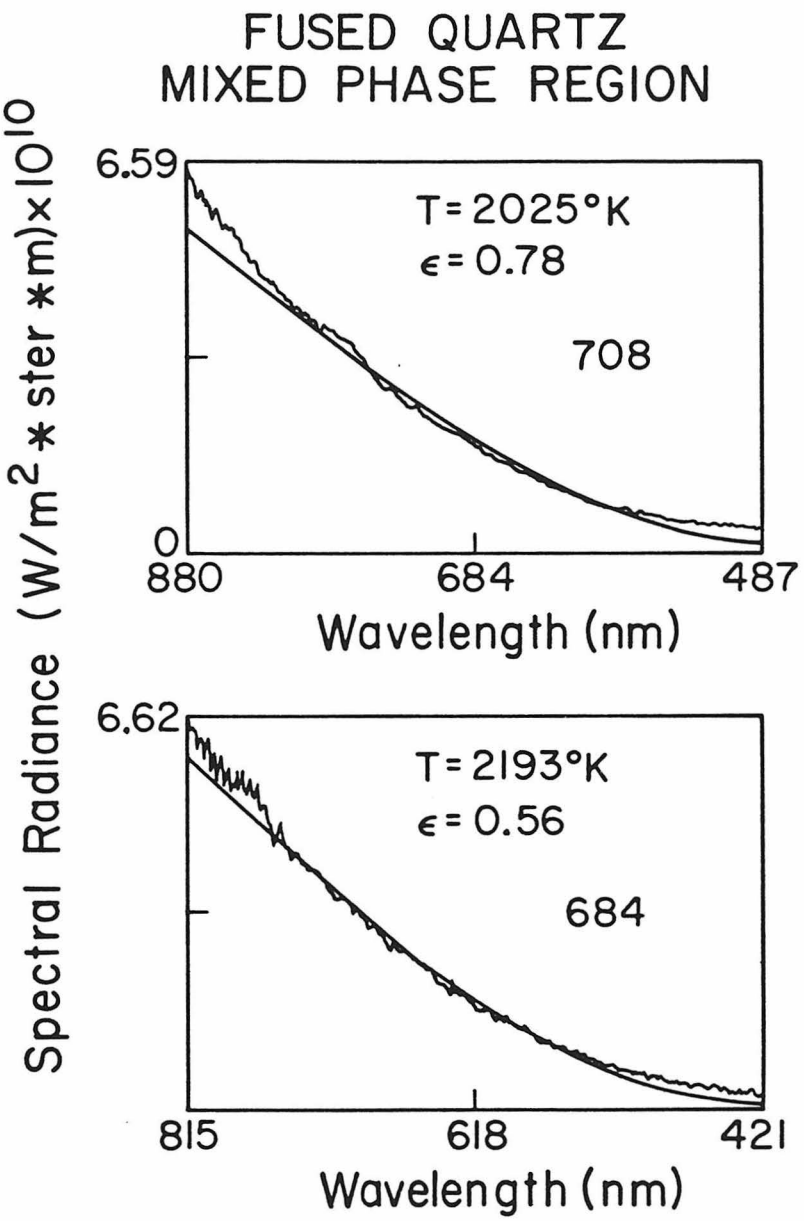

Figure 11) Observed spectra from fused quartz undergoing homogeneous shock deformation based upon low temperatures and high emittances (Field #3 in figure 13a and figure 14).

sensitivity of the spectrometer in this wavelength region and further points out the importance of weighting the data in least squares fits. This effect may also be seen at the high wavelengths where there is a noticeable increase in the signal to noise ratio. The level of noise for shot #635 is particularly high as in this experiment most of the light was routed to the TRW framing camera.

Figure 10 displays spectra over the pressure range of 16 to 30 GPa , the spectra in this figure are included on the basis of their emittance and their shock pressure within the mixed phase region of fused quartz. The two spectra in figure 11 for shots #708 and #684 are within the same pressure range but both had much lower temperatures and emittances an order of magnitude larger than the spectra of figure 10.

Photodiode records for this series of experiments are shown in figure 12. These are the combined results from both the oscilloscope and transient recorder data. Since the photodiode supplies only a qualitative response, all intensities have been normalized. The response of the photodiode is dependent upon the amount of light allowed to reach the spectrometer, the calibration lamp therefore gives a response of 200 mV to 700 mV and the typical peak amplitude during an experiment ranges from 100 mV to 300 mV. It should be noted that the photodiode and the spectrometer view different but adjacent regions of the sample during an experiment (figure 4). The photodiode records are discussed below.

It should also be noted that shot #686 at 17.4 GPa had no observable light emitted during the accumulation time of the spectrometer. Additionally, the photodiode recorded essentially no intensity until 500 ns

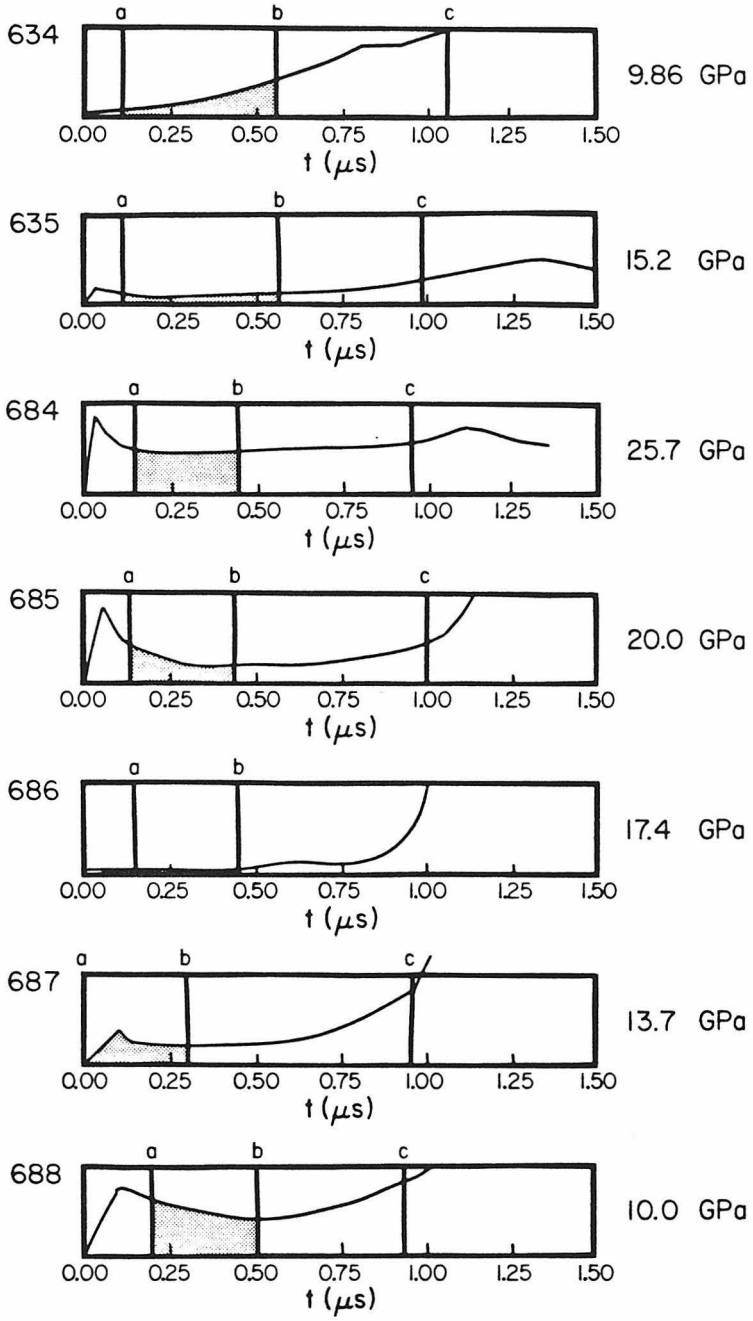

Figure 12) Normalized intensity vs time, fused quartz. Fiducials a,b, and c represent times of initiation of spectrometer light accumultation, end of accumulation, and first shock wave arrival at sample free surface.

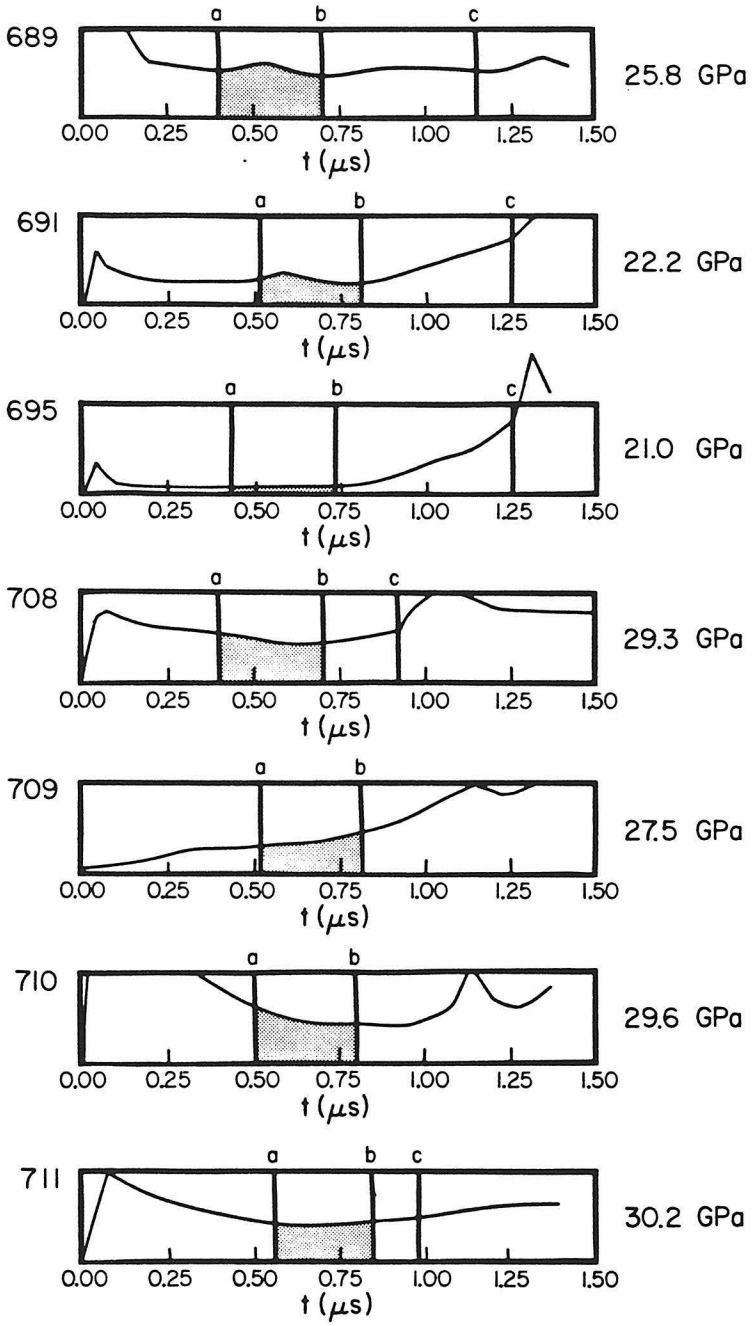

Figure 12) Normalized intensity vs time, fused quartz. Fiducials a,b, and c represent times of initiation of spectrometer light accumultation, end of accumulation, and first shock wave arrival at sample free surface.

after entry of the shock wave into the sample. This is followed by a large flash when the shock wave reaches the free surface of the sample at approximately 1 microsecond.

Least square temperatures fit to equation (3) for the above spectra are plotted in figure 13 and the corresponding emittances vs pressure are plotted in figure 14 and given in Table 1.

The range of the estimated Hugoniot temperatures of fused quartz is shown in figure 13. The high estimate is that of Kondo et al., (1981b) and the low estimate is that of Wackerle (1962). We believe these estimates to be extreme. It is difficult to calculate the continuum shock temperature of fused quartz under shock compression by the method of Ahrens et al. (1969) because of the lack of knowledge of an accurate isentropic equation of state of fused quartz above 3 GPa and of the correct thermodynamic parameters. For example, fused quartz has an extremely low thermal Gruneisen parameter of 0.012 at 1 bar pressure due to its small coefficient of thermal expansion. This may not remain small with increasing pressure. Another complicating factor is the anomalous compression of fused quartz; the bulk modulus of fused quartz is known to decrease to approximately 2.3 GPa (Kondo et al., (1980)) and is not well known above this pressure.

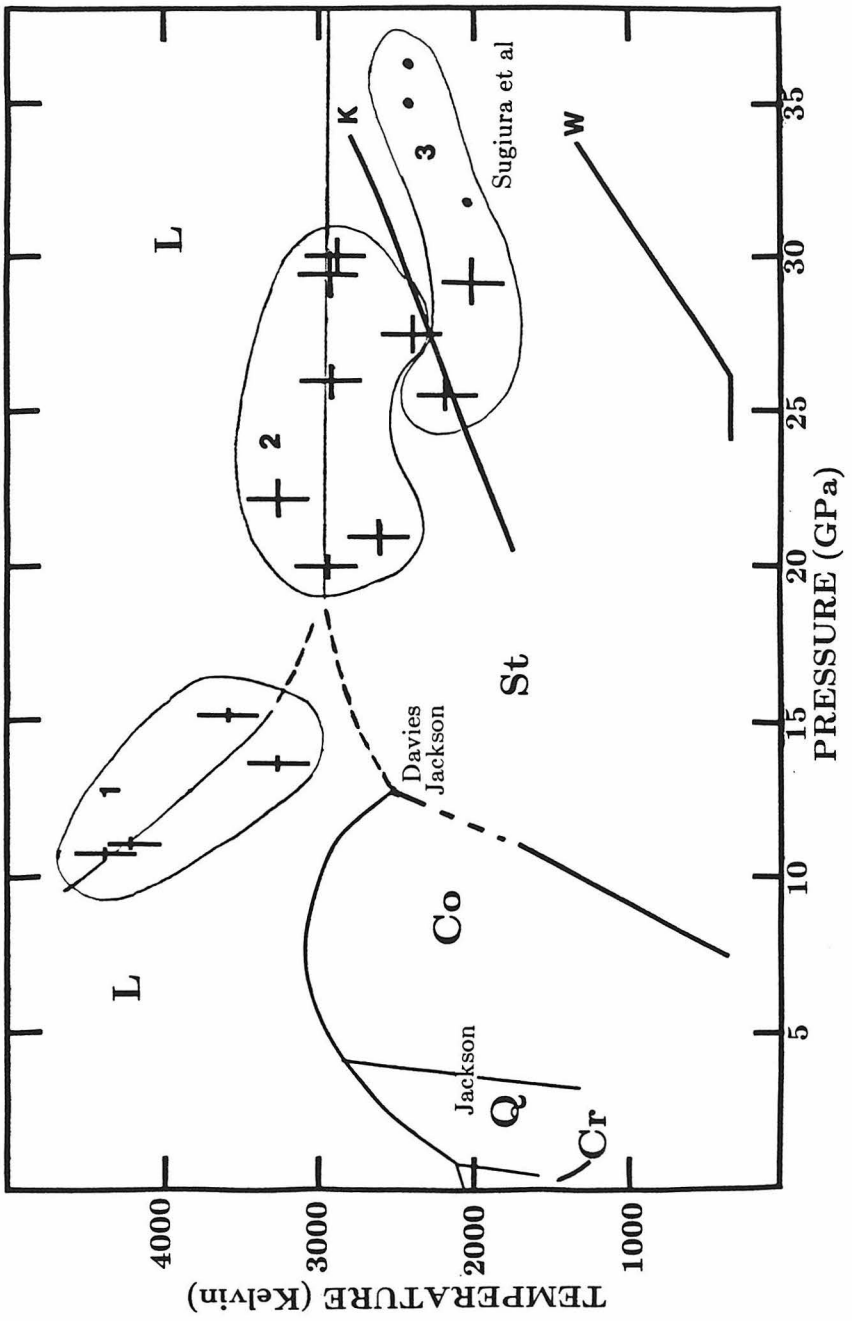

Figure 13a) Fused quartz temperatures vs pressure. Data is separated into three fields: 1,2,3, as in figure 14. Coesite-Stishovite-liquid triple point based on calculations of Davies (1972) and Jackson (1976). Quartz-Coesite line based on data of Holm et al (1967). Coesite- Stishovite phase line from Jeanloz and Thompson (1983). Estimated shock temperatures of Kondo et al (1981) (K) and Wackerle (1962) (W). Estimated stability fields of silica melt (L), stishovite (St), coesite (Co), crystalline quartz (Q), and cristobalite (Cr) are shown.

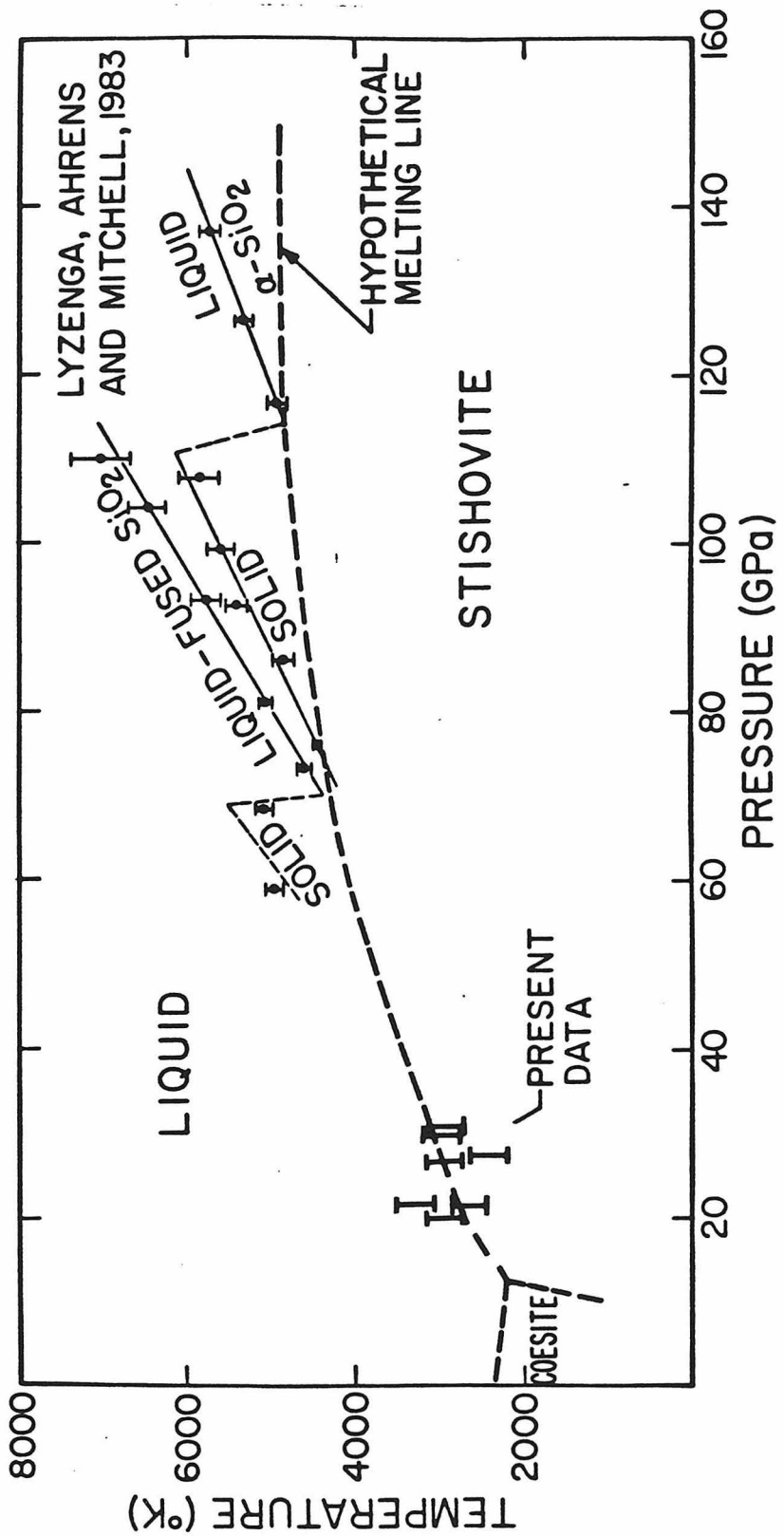

Figure 13b) Temperature vs pressure plot to include the data of Lyzenga et al (1983) and their proposed melting line. Plot contains only data from field #2.

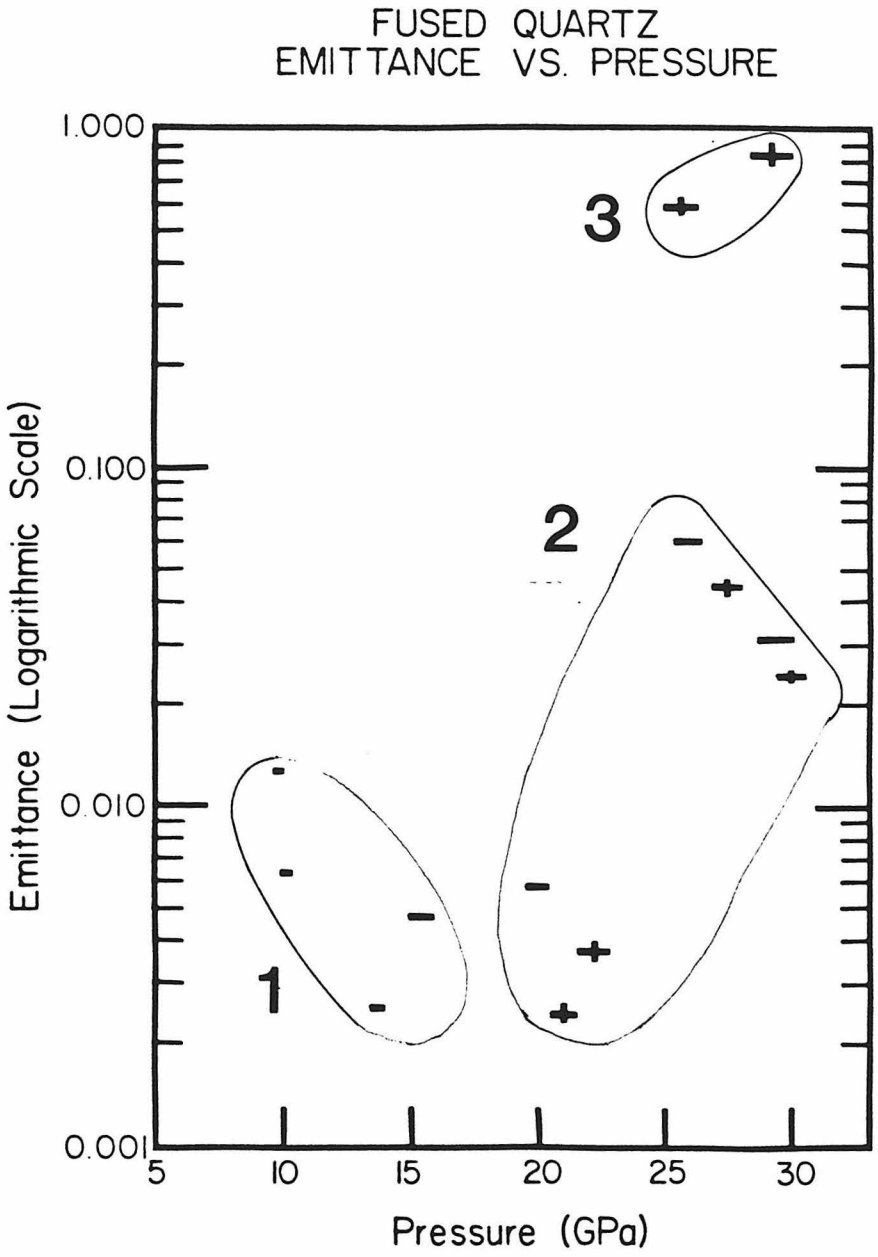

Figure 14) Log(greybody emittance) vs pressure. Field numbers are the same as in figure 13a.

DISCUSSION

HETEROGENEOUS DEFORMATION IN FUSED QUARTZ

New evidence for the heterogeneous deformation of fused quartz under shock compression is supplied by the framing camera photograph of shot #634 (figure 8) in which is seen a pattern of bright regions or hot spots in agreement with earlier studies (Brooks (1965), Brannon et al., (1983)). The number of regions grows with time, i.e., with the distance the shock wave has propagated into the fused quartz. Additionally, these regions persist and grow for at least 500 ns: the time spanning this set of exposures. Further, that these localized hot zones originate in the fused quartz is proven by the simultaneously recorded photodiode record (figure 12). No sample-driver interface flash is seen; light intensity commences at zero when the shock wave enters the fused quartz and grows linearly with time suggesting a constant production of hot spots with increasing propagation of the shock wave into the sample.

INTERPRETATION OF TEMPERATURES AND EMITTANCES

Figure 13a displays the observed shock temperatures vs. pressure. The estimated fields of silica melt (L), stishovite (St), coesite (Co), crystalline quartz (Q), and cristobalite (Cr) are shown. The stability fields below 5 GPa are from Jackson (1976) and the inferred coesite-liquid and coesite-stishovite phase boundaries are from Davies (1972) and Jeanloz and Thompson (1983). Temperature measurements above 30 GPa of Sugiura et al., (1982) are also included as well as the calculated fused quartz

shock continuum temperatures (Kondo et al., (1981), Wackerle (1962)) as discussed above.

The following observations are made from this plot:

1) Temperature appears to decrease with pressure from over 4400 K at 10 GPa to approximately 3000 K at 30 GPa. This decrease levels off above 16 GPa.

2) Observed color temperatures exceed those calculated for the continuum by nearly 1000 K.

3) three anomalous shots above 25 GPa exhibit lower temperatures.

There is an approximate dependence on emittance on pressure (figure 14). Below 25 GPa all emittances are less than 0.02. A threshold pressure appears to be reached above 25 GPa where the emittance increases by at least an order of magnitude. Finally, two shots have emittances which are almost those of a blackbody. The emittance may be an approximate measure of the areal density of the localized zones of deformation; the density of the features of heterogeneous deformation increases with pressure (Ashworth and Schneider (1985)). The approach of emittance towards unity at the higher pressures may signal the onset of a regime of a more homogeneous shock deformation reached when the density of microfaults becomes high.

The observation of temperatures greatly in excess of the estimated continuum temperatures and corresponding low emittances suggest that fused quartz undergoes a process of heterogeneous shock deformation (as also suggested by similar shock wave experiments of crystalline

halite, calcite, and gypsum (Kondo and Ahrens, (1983)), and potassium chloride, lithium fluoride, and periclase (Schmitt et al., (1986), Schmitt and Ahrens (1983))).

Based upon observations of the observed temperatures and emittances the data has been divided between three fields, each of which is characterized by the type of shock deformation occurring, and the magnitude of the emittance.

The first field is within the pressure range of 10 to 16 GPa which is the range of permanent densification of fused quartz (Sugiura et al., (1981)). The spectra within this field have low emittances (less than 0.015) and the highest temperatures (3200 K to 4400 K) which decrease with increasing pressure. This anomalous behavior is not understood but appears to be related to the transformation to stishovite which commences near 7.5 GPa at low temperatures as noted earlier. The high temperatures may be characteristic of the transformation at the initiation of the mixed phase region. This phenomenon has been more fully observed in crystalline NaCl over the B1-B2 solid phase transition region (see chapter 3). However, the phase relations of NaCl are much simpler than those of SiO_2 with the high pressure phases of coesite and stishovite; a direct analogy between NaCl and SiO_2 may not be justified.

On a speculative note, these high temperatures may be related to the large activation energy or energy barrier ($\sim 3.5 \cdot 10^6$J/kg of SiO_2) to the reconstructive quartz to stishovite transformation (Grady (1980)) which dictates the amount of energy required to initiate the transformation. Deposition of insufficient energy by the shock wave to activate the transformation

must result in a rise in temperature of the material. The maximum temperature rise (ΔT) may be estimated by the amount of energy required to activate the process (A) divided by the heat capacity (C_p) of the material or:

$$(4)\quad \Delta T = \frac{A}{C_p}.$$

Using the values of activation energy and the heat capacity of table 2 the maximum temperature rise before activation of the transformation is estimated to be approximately 4700 K; this figure is consistent with the observed radiative temperatures of ~4400 K near 10 GPa. If the observed emittances (~ 0.01) near 10 GPa yield the relative volume of material undergoing the phase transformation, then the process mentioned above requires approximately 10 to 15% of the total energy available in shock compressed fused quartz by the Rankine-Hugoniot energy equation:

$$(5)\quad \Delta E = \frac{1}{2}(V_o - V_1)P_h .$$

where ΔE is the internal energy change upon shock compression, V_o and V_1 are the initial and final specific volumes, respectively, and P_h is the shock pressure.

Field #2 contains the shots which have low emittances (less than 0.1) and are within the mixed phase region of the fused quartz Hugoniot. The high temperatures and low emittances indicate a heterogeneous deposition of thermal energy within the fused quartz. These temperatures would represent the melting temperature of stishovite at high pressure. The melting temperature of stishovite between 20 and 30 GPa is estimated to be 3000 K ± 200 K. To the degree of precision available in this experiment,

Table 2: Thermal Parameters used in Calculations

Symbol	Definition	Value	Reference
C_p	Heat Capacity	753 J/°Kkg	Weast (1977)
ρ	Density	2204 kg/m^3	Measured
L	Latent Heat of Fusion	2.37×10^5J/kg	Weast (1977)
k	Thermal Conductivity	1.38W/m °K	Weast (1977)
κ	Thermal Diffusivity($k/\rho C_p$)	8.33×10^{-7}m^{2}s^{-1}	Calculated
A	Activation Energy of α - quartz to stishovite reconstructive transformation	3.5×10^6J/kg	Grady (1980)

this melting temperature is independent of pressure.

Lyzenga et al., (1983) measured shock temperatures in both fused and crystalline quartz between 60 and 140 GPa. At these pressures silica is believed to be well into the stishovite phase (see earlier discussion of phase transformation in quartz). Based on their temperature measurements, Lyzenga and co-workers provided evidence for the melting of stishovite and obtained an hypothetical melting curve at high pressure (Figure 13b). The present data lie on or close to the proposed melting line of Lyzenga et al., (1983) supporting to the present hypothesis.

Field #3 contains the two high emittance - lower temperature data indicative of the onset of a more homogeneous deformation. These temperatures are close to those observed by Sugiura et al., (1982) by a similar technique above 30 GPa. Higher emittances appear to indicate more homogeneous shock deformation according to Lyzenga and Ahrens (1980) who report emittances > 0.75 and in most cases near unity for fused quartz shocked to pressures in excess of 70 GPa. Lyzenga et al., (1983) further demonstrate the homogeneity of the deformation at these pressures in a streak camera record of alpha quartz at 106.5 GPa which displays uniform emittance.

The reason for the overlap of the pressure ranges of fields #2 and #3 is not known and may be related to differences in sample preparation or due to the inherent difference in fused quartz samples. Within a given sample of fused quartz the variation of the index of refraction, which is a measure of density, can be as high as $5.0 \cdot 10^{-6}$ (Heraeus-Amersil Specifications). Also, small bubbles and inclusions do exist within the fused

quartz; differences in their density may result in the observed shot to shot variations.

PHOTODIODE RECORDS

Ideally, the present experiments are designed to prevent light generation at the driver-fused quartz interface. Because of the opaque silver film detected light originates only within the shocked fused quartz. The production of hot shear deformation zones appears to be nearly constant with time. The hot zones persist for a timescale on the order of the transit time of the material (Grady (1980)), and the absorption characteristics of the shock compressed material appear to be nearly identical to the as yet unshocked material. This results in a linear increase in the emitted intensity with time (Boslough (1985)); the ideal photodiode record would therefore have a nearly linear increase in intensity with the propagation of the shock wave into the sample. Such behavior is displayed by shots #634 and #709 at pressures of 9.8 and 27.5 GPa, respectively.

However, many of the experimental photodiode records (figure 12) display a more complicated structure which includes evidence of some fused quartz sample-driver interface heating (coinciding with entry of the shock wave into the sample). This problem has been addressed by Urtiew and Grover (1974), Grover and Urtiew (1974), Boslough (1985), and Svendsen et al., (1987), who demonstrate this is a potential problem with measurements of shock temperatures in clear or translucent materials. Briefly, their model involves deposition of a quantity of heat at the interface due to collapse of micron scale gaps between the driver and sample. This heat results in the

production of high temperatures at the interface which decay inversely with $(\kappa t)^{1/2}$, where κ is the thermal diffusivity of the metal driver which is assumed to have a higher thermal conductivity with respect to the sample. The observed photodiode records display this behavior. Note that the rise time of the photodiode due to its amplification is approximately 50 ns. Thus because of the finite rise time of the photodiode electronics, the peaks signal is nearly coincident with the entry of the shock wave into the sample.

Some photodiode signals are thus a superposition of the interface gap flash and the light produced within the fused quartz (Boslough et al., (1986)) (figure 15, table 1). Contamination occurs when spectrometer accumulation occurs primarily during the time of decreasing photodiode intensity due to interface cooling. Moderate contamination occurs when the gap flash is low amplitude and part of the accumulation time overlaps with decreasing photodiode intensity. Contamination is considered to be small when accumulation time occurs in an increasing or almost level portion of the light intensity signal observed after the interface temperature has decayed to the continuum temperature of the shocked sample. In table 1, none refers to no gap flash contamination.

Although we expected that the potential effect of gap flashes on the measured temperatures might be very deleterious, we found surprisingly that shots at nearly the same pressure yield similar temperatures regardless of the degree of gap flash contamination. For example, shot #634 at 9.8 GPa (with no gap flash) and shot #688 at 10.0 GPa (severe gap flash) gave temperatures in excess of 4000 K and similar emittances. Additionally, shots #710 and #711 at pressure of 29.6 and 30.2 GPa with severe and small gap flashes

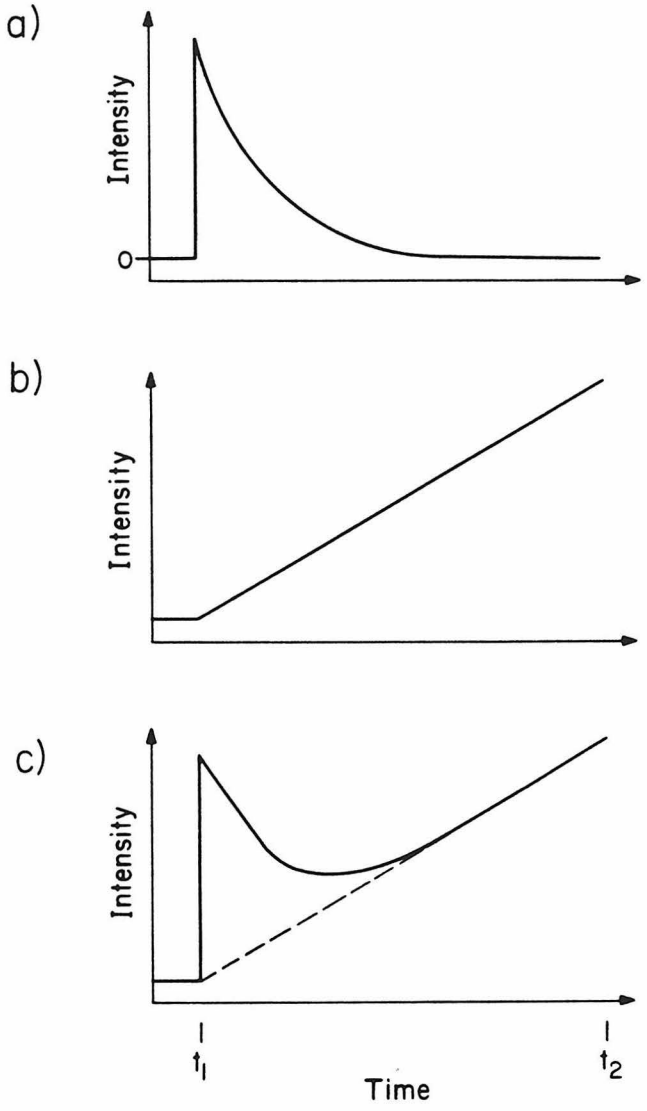

Figure 15) a)Hypothetical photodiode record assuming light originates only at driver - sample interface due to heating. b) Photodiode record assuming light originates only from features of heterogeneous deformation within the sample, c) Photodiode record similar to that observed, this is a superposition of records a) and b).

both gave temperatures near 2900 K and emittances between 0.2 and 0.3. A buffering of the gap temperatures to the melting point of the compressed silica (via mechanisms similar to those operating within the microfaults may be occurring). Another explanation may be related to the evolution of the shock wave with increasing penetration into the sample. Hayes and Graham (1978) calculate stress-time histories for an impact of quartz on quartz and assume dependent shear stress relaxation occurs. The energy density dissipated at a given depth within the sample decreases monotonically until a stable shock wave is formed. Higher temperatures and densities of deformation features occur near the interface.

VARIATION OF TEMPERATURE WITHIN MICROFAULTS WITH TIME

The observed temperatures, which we here suggest to be at the temperature of the melt in the microfaults, could be dependent on the scale of the deformation features on account of heat conduction. In melting experments within high pressure diamond cells Heinz (1986) noted the effect of spatial variations in temperature upon measured radiative temperatures. We now examine the conditions where the observed radiative temperatures will not represent the melting temperature in the microfault.

We use the theory for solidification of a dike emplaced in a body of cooler country rock (Turcotte and Schubert (1982)). Consider the microfault as a layer of thickness d of molten silica, at the melting temperature at a given pressure, created within the shock wave front zone. Initially, material within the shear band is assumed to be totally molten and at the melting temperature: T_m. Material outside of the shear band is

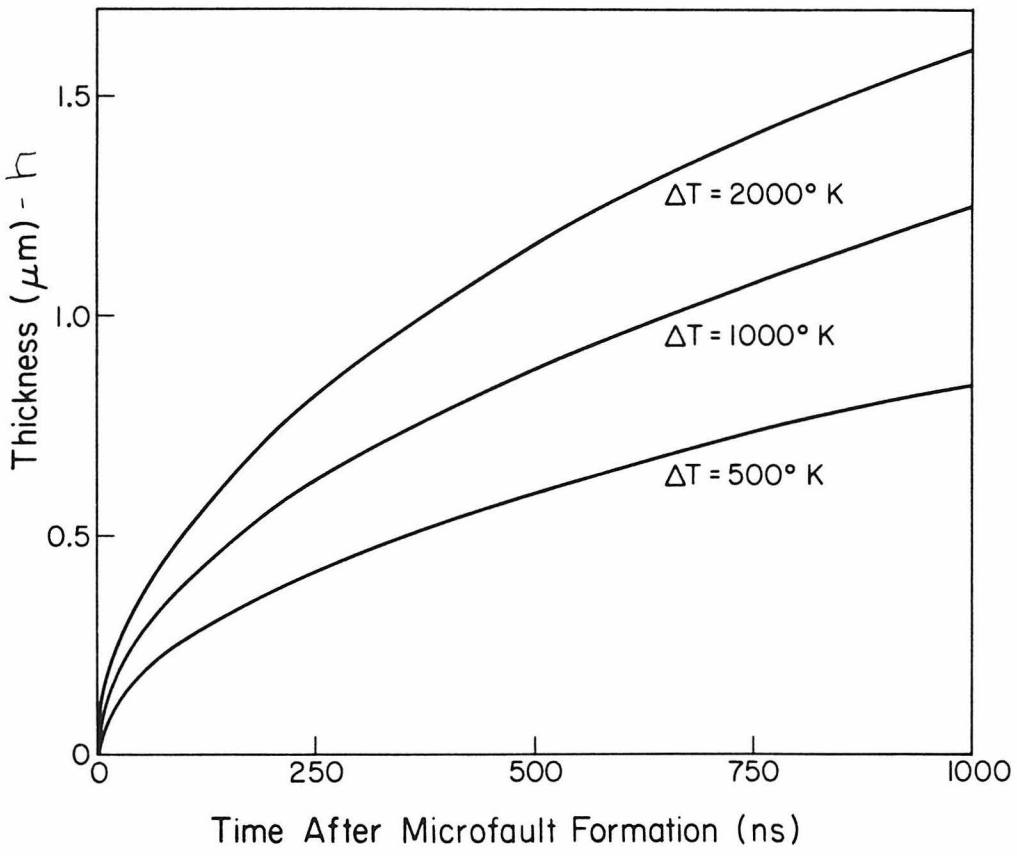

Figure 16a) Solidified zone thickness vs. time after formation of microfault. $\Delta T = T_m - T_o$.

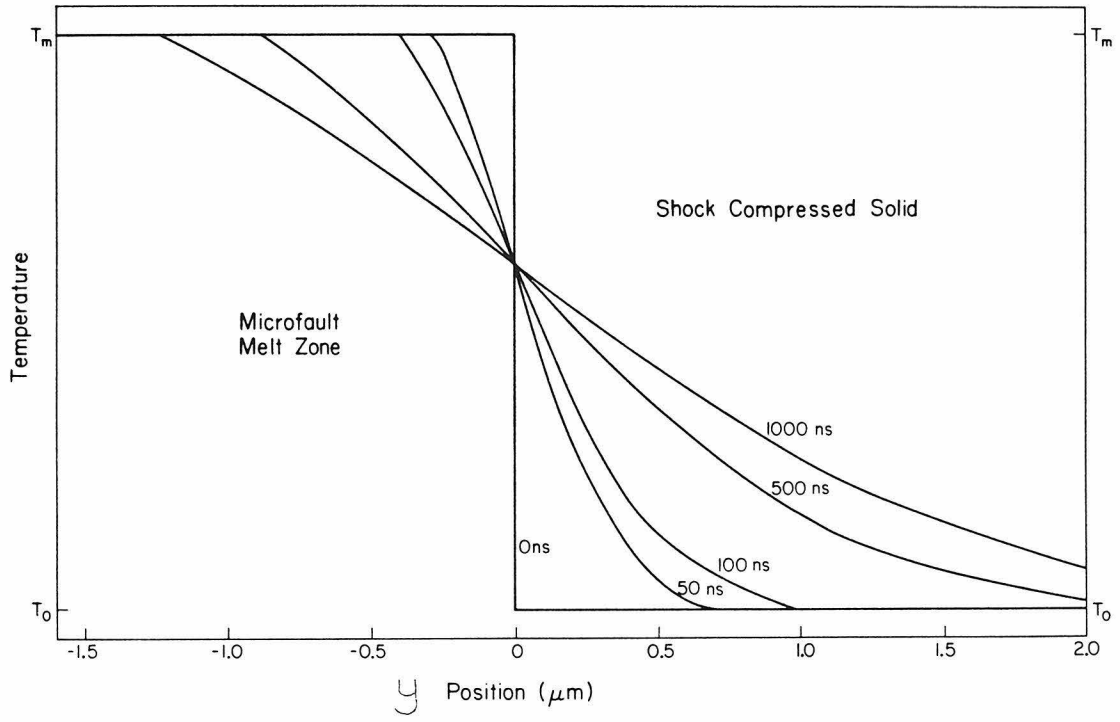

Figure 16b) Temperature distribution in the region of the initial microfault boundary at various times.

shock

compressed solid at the cooler temperature T_o which is nearly equal to the continuum temperature. In most cases $T_m >> T_o$. However, heat flow from the microfault zone at T_m and the compressed solid at T_o must occur via phonon or radiative conduction. thus cooling of the shear band and the release of the latent heat of fusion during freezing occurs.

The temperature, T, in the solid is given as a function of y, the distance away from the interface and time, t as:

$$(6)\quad \frac{(T - T_o)}{(T_m - T_o)} = \frac{erfc(\nu)}{erfc(-\lambda)}$$

where

$$(7)\quad \nu = \frac{y}{(2(\kappa t)^{1/2})}$$

and the constant λ for a given set of thermal parameters must be determined by numerical calculation in the transcendental equation:

$$(8)\quad \frac{L(\pi)^{1/2}}{(C_p(T_m - T_o))} = \frac{e^{-\lambda^2}}{\lambda(1 + erf\ \lambda)}$$

T is the temperature as a function of time t and position y from the microfault. The liquid-solid shear band boundary is at y = 0 for t = 0. κ is the thermal diffussivity which is a function of the heat capacity of the material: C_p, the coefficient of thermal expansion: α, and the density of the material. L is the latent heat of fusion of silica, and erf and erfc are the error function and $1 - erf$, respectively.

The above equations have been solved using thermodynamic parameters for fused silica (Table 2) and for differences between the melt in the shear band and the surrounding solid of 500K, 1000K and 2000K. Figure 16a illustrates the growth of a frozen layer of solid with time for varied temperature differences. The figure illustrates that for an extreme temperature difference of 2000K the thickness of the solidified zone is approximately 1.6 microns 1 microsecond after creation of the microfault. Figure 16b displays the temperatures profile with time for an initial temperature difference of 1000K. Radiation emitted from these cooler regions will have an effect on the spectra of the observed light. The magnitude of this effect is dependent on the ratio of the volume of the cooled temperature material to the volume of the initial melted material. At maximum, the timescale for these experiments is 1 microsecond. Figures 16a and 16b therefore suggest that for a microfault of thickness of 10 microns, which is expected on the basis of shock recovery work on quartz (Gratz (1984)), this cooling by conduction and freezing will have little effect upon the observed temperatures. However, if the thickness of the microfault is 5 microns or less the cooling will have a much greater effect on the observed spectra. A microfault of 5 or less microns created early on in the shock experiment may freeze solid by the end of the experiment (figure 17). The effect of this cooling on measured temperatures, however, is offset by the constant production of microfaults with time as the shock wave propagates through the sample. Spectra are obtained from light accumulated not more than 800 ns after entry of the shock wave into the sample. The cooling effect would result in a shift of

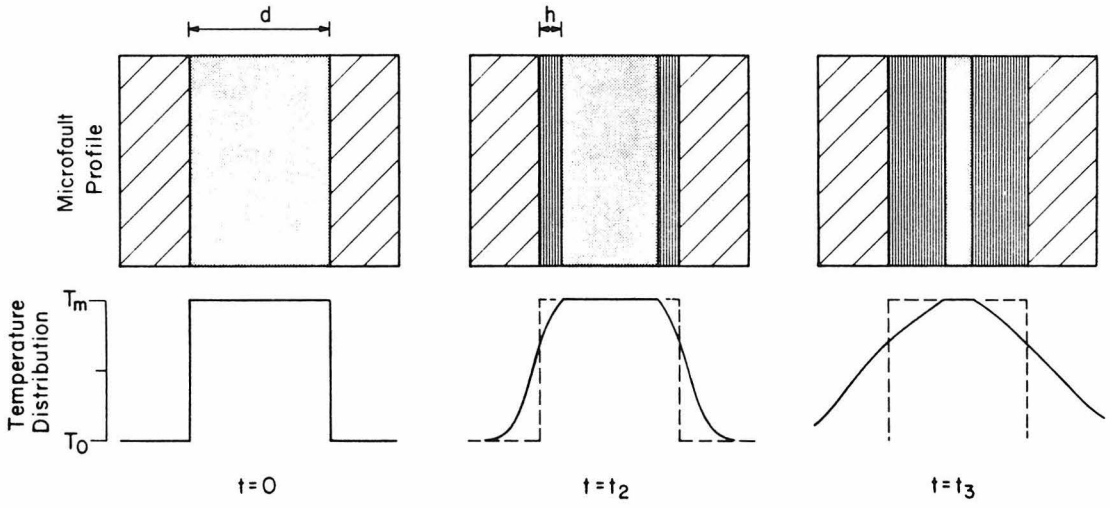

Figure 17) Evolution and cooling history of a microfault for various times. At t = 0, microfault is a layer of melt at T_m surrounded by solid compressed material at T_o, while t_2 and t_3 indicate patial and complete crystallization.

the peak in the greybody curve towards the infrared resulting in excess signal in the infrared and deficient signal in the ultraviolet and resulting in slight lowering of the observed greybody temperature.

The above modelling of microfault cooling should not be considered as the true history of a microfault. Shock recovery work favors the nucleation of small particle of solid stishovite as depicted in figure 2b (Ashworth and Schneider (1985)). Additionally, the present model does not take into account the kinetics of crystallization. It appears that only small amounts of a silicate can nucleate from the melt on the time scale of a shock experiment (Rigden et al., (1987)) The rate of crystallization of quartz from a melt as a function of pressure is not yet well understood, however, recent experimental work on the crystallization of quartz from fused quartz suggests (Fratello et al., (1980)) that crystallization rate increases with pressure up to 4 GPa.

COMPARISON OF NEW MELTING DATA WITH EARLIER RESULTS

The proposed estimates (figure 13a, table 1) for the melting temperature of silica between 20 and 30 GPa (stippled area of figure 18) are compared to melting data for Mg_2SiO_4 to 15 GPa (Ohtani and Kumazawa (1981)), $MgSiO_3$ to 4.6 GPa (Boyd et al., (1964)), $(Mg_{0.9},Fe_{0.1})SiO_3$ from 18 to 60 GPa (Heinz (1986)), and SiO_2 to 2.5 GPa (Jackson (1976)). According to figure 18, both SiO_2 and $(Mg_{0.9}Fe_{0.1})_2SiO_4$, as well as the extrapolation of the melting data for Mg_2SiO_4 are nearly the same temperature.

Using the melting temperatures of figure 18 and phase diagrams at the pressures of 1 atmosphere and 2.5 GPa the solidus temperatures in the system

--

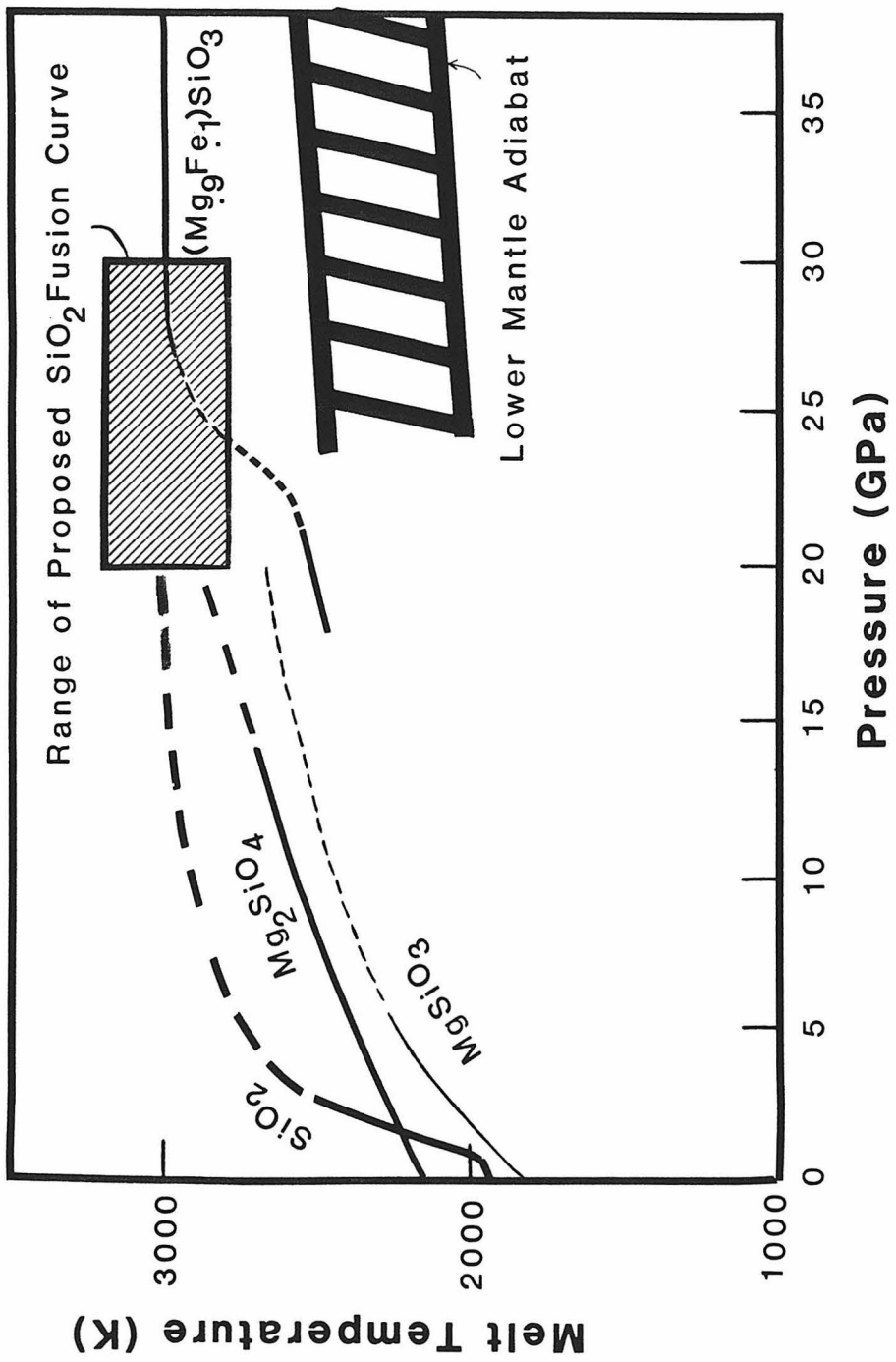

Figure 18). Comparison of proposed SiO_2 fusion curve (stippled region) with measured and inferred melting data for SiO_2 to 2.5 GPa (Jackson (1976)), $MgSiO_3$ to 5.0 GPa (Boyd et al. (1964)), Mg_2SiO_4 to 15 GPa (Ohtani and Kumazawa (1981)), and $(Mg_{0.9}Fe_{0.1})SiO_3$ from 18 to 38 GPa (Heinz (1986)). Inferred lower mantle adiabats from Jeanloz and Richter (1979).

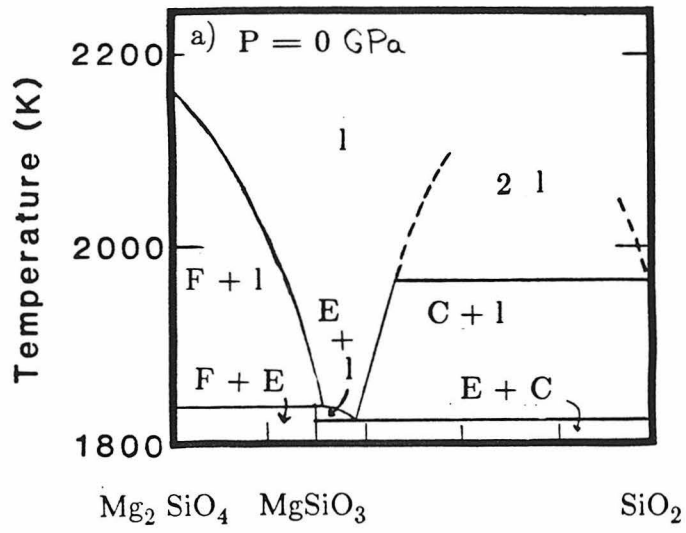

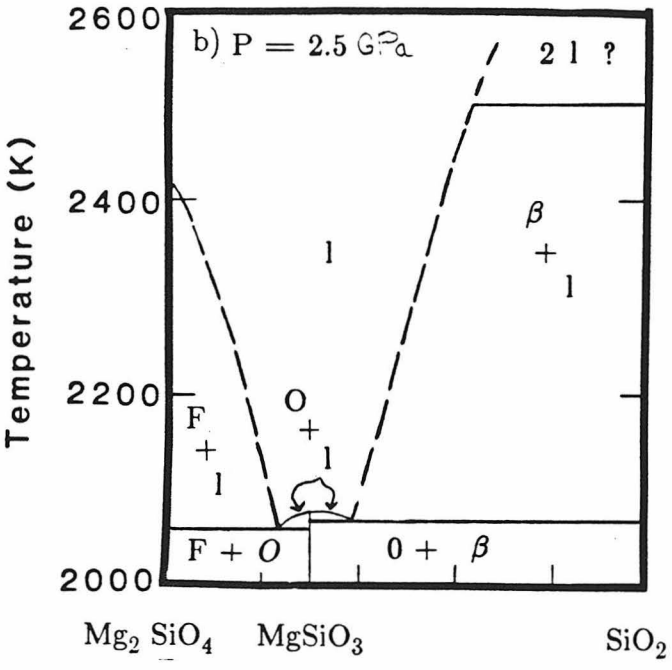

Figure 19a). Measured Mg_2SiO_4-SiO_2 phase diagram at 1 atmosphere. E: $MgSiO_3$ protoenstatite, F: Mg_2SiO_4 forsterite, C: SiO_2 cristobalite, l: liquid. **19b).** Mg_2SiO_4-SiO_2 phase diagram at 2.5 GPa. O: $MgSiO_3$ orthoenstatite, F: Mg_2SiO_4 forsterite, β: SiO_2, l: liquid.

Mg_2SiO_4-SiO_2 are estimated. The room pressure diagram (figure 19a) of Chen and Presnall (1975) displays a peritetic point at a composition of 60.6 weight % SiO_2. With increasing pressure, the composition of $MgSiO_3$ becomes an endmember component (figure 19b) (Chen and Presnall (1975)). Based on studies of two phase systems (Kennedy and Higgins (1972) and Newton et al., (1962)),the depth of the eutectic trough is expected to increase with increasing pressure, i.e., the minimum difference between the melting temperatures of a pure endmember component and the eutectic composition is observed at low pressure. In the extrapolations to higher pressures, the depth of the eutectic troughs are assumed to be the same as in figure 19b, thus the eutectic temperatures at higher pressures represent a maximum value. Additionally, it is assumed in the extrapolations that the composition of the two eutectics of figure 19b is constant, this assumption appears to be valid for the $MgSiO_3$-SiO_2 eutectic (Chen and Presnall (1975)) but may be in error by $\sim$ 3% for the other eutectic as the hydrous Mg_2SiO_4-$MgSiO_3$ system has a eutectic composition near 53 weight % SiO_2 (Kato and Kumazawa (1986)). Using the depth of the eutectic well from the $MgSiO_3$ melting temperature as determined by Chen and Presnall (1975) at 2.5 GPa (figure 19b) and extrapolating to higher pressures with the melting temperatures of figure 18, we infer the maximum solidus temperatures in the Mg_2SiO_4–SiO_2 system would be $\sim$ 2500 K at 12.5 GPa and 2650 K at 20.0 GPa. Inclusion of the component FeO would further depress the solidus temperatures; for an estimated mantle Fe/(Fe + Mg) ratio of 10% (Jeanloz and Thompson (1983)), the solidus temperature may be further depressed by $\sim$ 130 K as estimated from the drop in the solidus temperature in the system Mg_2SiO_4–Fe_2SiO_4 at one atmosphere

(Bowen and Schairer (1935)). The maximum solidus temperatures within the mantle may thus be $\sim$ 2370 K at 12.5 GPa and 2520 K at 20.0 GPa.

Weertman (1970) suggests that the effective viscosity of a solid at a constant creep rate is given by:

$$(9)\quad \eta = C exp\,(g\frac{T_m}{T})$$

where η is the effective viscosity, C is a constant, T_m is the melting temperature, T is the temperature of the material, and g is a dimensionless constant empirically found to be $\sim$ 18.0 for most metals. The ratio of T_m / T for the proposed melting curve of SiO_2 (T_m) (figure 18) and an upper mantle geotherm (T) (Turcotte and Schubert (1982)) is given in figure 20. At pressures between 6.5 and 20 GPa, T_m / T is nearly constant, ranging from 1.74 ot 1.64 and suggesting little variation in the effective viscosity from 200 to 600 km at depth within the Earth.

CONCLUSIONS

The major findings of this study are:

1) Fused quartz, like other brittle minerals subject shock compression, undergoes heterogeneous shock deformation characterized by localized zones of melting between 16 and 30 GPa. Evidence for this is supplied by the framing camera photographs that show hot regions which persist and grow during shock compression and the high temperature-low emittance greybody spectra observed between 16 and 30 GPa.

2) The observed temperatures reflect the temperature of the localized zones of deformation. Shock recovery and release wave studies suggest that

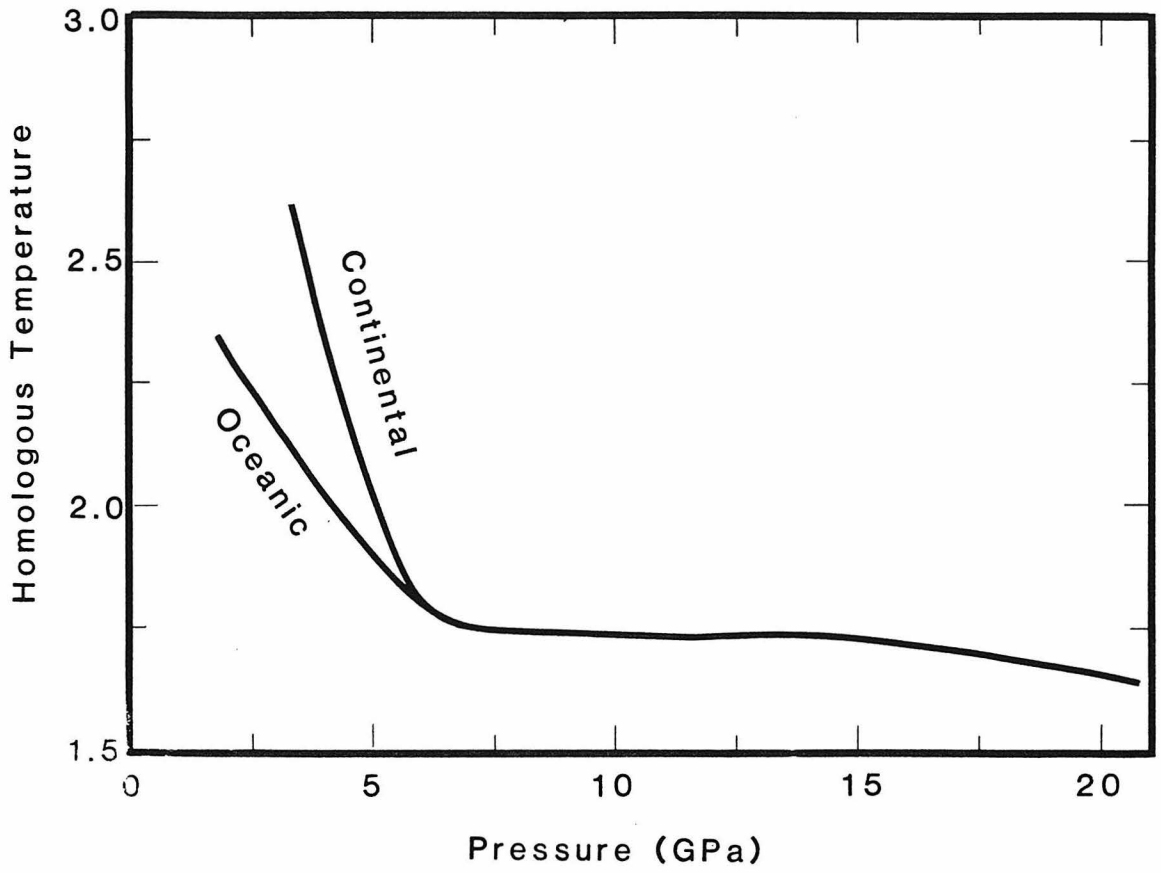

Figure 20). Homologous temperature: T_m / T where T_m is the melting temperature chosen from the proposed melting curve of SiO_2 with pressure and T is the temperature of the material here chosen as temperatures along the upper mantle oceanic and continental geotherms of Jeanloz and Richter (1979) and Turcotte and Schubert (1982).

these zones are molten during shock compression. Shock recovery work and the Hugoniot of fused quartz suggest that the high pressure solid phase (stishovite) is produced within these shear bands or microfaults.

3) The melt temperature within these microfaults may be buffered by the production of the high pressure phase and as such may reflect the liquidus temperature of stishovite at high pressure. This suggests that this temperature is approximately 3000 K in the pressure range of 20 to 30 GPa and is independent of pressure.

4) Shock compression becomes more homogeneous with increasing pressure as evidenced by the general increase in emittance with pressure.

5) Shock temperatures observed in the pressure range of 10 to 16 GPa are up to 2000 K higher than temperatures at increased shock pressure and appears to be related to the onset of the fused quartz- stishovite phase transformation. These high temperatures and subsequent decrease in temperature with increasing pressure are not understood. Similar behavior is seen in NaCl over the B1-B2 phase transition region.

6) Solidus temperatures for Mg_2SiO_4-SiO_2 system inferred from the present proposed melting curve for SiO_2 at high pressure together with other melting data suggest that the maximum solidus temperatures within the mantle are close to 2370 K at 12.5 GPa and 2520 K at 20.0 GPa. Comparison of the proposed SiO_2 melting curve with reasonable predicted geotherm temperatures suggests that the effective viscosity between 200 and 600 km within the mantle is nearly constant.

--

REFERENCES

Ahrens, T.J., Anderson, D.L., and Ringwood, A.E., Equations of State and Crystal Structures of High-Pressure Phases of Shocked Silicates and Oxides, *Rev.Geophy.*, **7**, pp. 667-707. 1969.

Ahrens, T.J. and Rosenberg, J.T.,Shock Metamorphism Experiments on Quartz and Plagioclase, in *Shock Metamomorphism in Natural Materials*, ed. French, B.M. and Short, N.M., pp. 59-81, 1968.

Al'tshuler, L.V., Trunin, R.F., and Simakov, G.V., Shock Wave Compression of Periclase and Quartz na the Composition of the Earth's Lower Mantle, *Izv.Phys.Solid Earth*, **10**, pp. 657-660, 1965.

Anan'in, A.V., Breusov, O.N., Dremin, A.N., Pershin, S.V., and Tatsii, V.F., The Effect of Shock Waves on Silicon Dioxide. I. Quartz, *Combustion Explos. Shock Waves*, **10**, pp. 372-379, 1974a.

Anan'in, A.V., Breusov, O.N., Dremin,A.N., Pershin, S.V., Rogacheva, A.I., and Tatsii, V.F., Action of Shock Waves of Silicon Dioxide, II. Quartz Glass, *Combustion Explos. Shock Waves*, **10**, pp. 504-508, 1974b.

Arndt, J., Hornemann, U., and Muller, W.F., Shock-Wave Densification of Silica Glass, *Phys.Chem.Glasses*, **12**, pp. 1-7, 1971.

Arndt, J., and Stofller, D., Anomalous Changes in Some Properties *Phys.Chem.Glasses*, **10**, pp. 117-124, 1969.

Ashworth, J.R., and Schneider, H., Deformation and Transformation in Experimentally Shock-Loaded Quartz, *Phys.Chem.Minerals*, **11**, 241-249, 1985.

Barker, L.M. and Hollenbach, R.E., Shock-Wave Studies of PMMA, Fused Silica, and Sapphire, *J.Appl.Phys.*, **41**, pp. 4208-4226, 1970.

Boslough, M.B., Ahrens, T.J., and Mitchell, A.C., Shock Temperatures in Anorthite Glass, *Geoph.J.R.astr.Soc.*, **84**, pp. 475-489, 1986.

Boslough, M.B., A Model for Time Dependence in Shock-Induced Thermal Radiation of Light, *J.Appl.Phys.*, **58**, pp. 3394-3399, 1985.

Bowen, N.L., and Schairer, J.F., The System $MgO-FeO-SiO_2$, *Amer.J.Sci., 5 th Ser.*, **29**, pp. 151-217, 1935.

Boyd, F.R., England, J.L., and Davies, B.T.C., Effect of Pressure on the Melting and Polymorphism of Enstatite, $MgSiO_3$, *J.Geoph.Res.*, **69**, pp. 2101-2109, 1964.

Bridgman, P.W. and Simon, I., Effects of Very High Pressure on Glass, *J.Appl.Phys.*, **24**, pp. 405-413, 1953.

Brannon, P.J., Morris, R.W.,and Asay, J.R., Shock-Induced Luminescence from Z-cut Lithium Niobate, *J.Appl.Phys.*, **57**, pp. 1676-1679, 1985.

Brannon, P.J., Konrad, C., Morris, R.W., Jones, E.D., and Asay, J.R., Studies of the Spectral an Spatial Characteristics of Shock-Induced Luminescence from X-cut Quartz, *J.Appl.Phys.*, **54**, pp. 6374-6381, 1983a.

Brannon, P.J, Konrad, C.H., Morris, R.W., Jones, E.D., and Asay, J.R., Spectral and Spatial Studies of Shock-Induced Luminescence from Quartz, *Sandia Report*, **#SAND82-2469**, 84 p., Sandia National Laboratories, Albuquerque, New Mexico, 1983b.

Brooks, W.P., Shock-Induced Luminescence in Quartz, *J.Appl.Phys.*, **36**, pp. 2788-2790, 1965.

Chao, E.C.T., Shoemaker, E.M., and Madsen, B.M., First Natural Occurance of Coesite, *Science*, **132**, pp. 220-222, 1960.

Chao, E.C.T., Fahey, J.J, Littler, J., and Milton, D.J., Stishovite, SiO_2, a Very High Pressure New Mineral from Meteor Crater, Arizona , *J.Geoph.Res.*, **67**, pp. 419-421, 1962.

Chen, C., and Presnall, D.C., The System $Mg_2SiO_{4-SiO_2}$ at Pressures Up to 25 Kilobars, *Amer.Miner.*, **60**, pp.398-406, 1975.

Chhabildas, L.C., and Grady, D.E., Dynamic Material Response of Quartz at High Strain Rates, *Mat.Res.Soc.Symp.Proc.*, Vol **22**, pp. 147-150, 1984.

Chhabildas, L.C. and Grady, D.E., Shock Loading Behavior of Fused Quartz, *Shock Waves in Condensed Matter - 1983*, ed. Asay,J.R., Graham,R.A., and Straub,G.K., Elsevier Science Publishers, pp. 175-178, 1984.

--

Chhabildas, L.C. and Miller, J.M., Release-Adiabat Measurements in Quartz, *Sandia Report,* **SAND85-1092**, p. 25, 1985.

Coes, L., A New Dense Crystalline Silica, *Science*, **118**, pp. 131- 132, 1953.

Cohen, H.M. and Roy, R., Effects of Ultrahigh Pressure on Glasss, *J.Am.Ceram.Soc.*, **44**, pp. 523-524, 1961.

Dachille, J., Zeto, R.J., Roy, R., Coesite and Stishovite: Stepwise Reversal Transformation, *Science*, **131**, pp. 1675-1676, 1963.

Davies, G.F., Equations of State and Phase Equilibria of Stishovite and a Coesitelike Phase from Shock-Wave and Other Data, *J.Geoph.Res.*, **77**, pp. 4920-4933, 1972.

Davison, L., and Graham, R.A., Shock Compression of Solids, *Phys. Rept.*, **55**, pp. 255-379, 1979.

DeCarli, P.S. and Milton, D.J., Stishovite: Synthesis by Shock Wave, *Science*, **147**, pp. 144-145, 1965.

Deer, W.A., Howie, R.A., and Zussman,J., *An Introduction to the Rock Forming Minerals*, John Wiley and Sons, New York, 528 pg., 1966.

Duvall, G.E., and Graham, R.A., Phase Transitions Under Shock Loading, *Rev.Mod.Phys.*, **49**, pp.523-579, 1977.

Duvall, G.E. and Fowles, R., Shock Waves, in *High Pressure Physics and Chemistry*, R.S.Bradley ed., Academic Press, N.Y., vol. **2**, pp. 209-291, 1963.

Fowles, R., Dynamic Compression of Quartz, *J.Geoph.Res.*, **72**, pp. 5729-5742, 1967.

Fratello, V.J., Hays, J.F., and Turnbull, D., Dependence of Growth Rate of Quartz in Fused Silica on Pressure and Impurity Content, *J.Appl.Phys.*, **51**, pp. 4718-4728, 1980.

Gibbons, R.V., and Ahrens, T.J., Shock Metamoprphism of Silicate Glasses, *J.Geoph.Res.*, **76**, pp. 5489-5498, 1971.

Grady, D.E., Shock Deformation of Brittle Solids, *J. Geoph. Res.*, **85**, pp. 913-924, 1980.

Grady, D.E., Processes Occurring in Shock Wave Compression of Rocks and Minerals, in *High Pressure Research, Applications in Geophysics*, Academic Press, N.Y., pp., 1977.

Grady, D.E., Murri, W.J., and DeCarli, P.S., Hugoniot Sound Velocities and Phase Transformations in Two Silicates, *J.Geoph.Res*, **80**, pp. 4857-4861, 1975.

Grady, D.E., Murri, W.J., and Fowles, G.R., Quartz to Stishovite: Wave Propagation in the Mixed Phase Region, *J.Geoph.Res.*, **79**, pp. 332-338, 1974.

Graham, R.A.,Shock-wave Compression of x-Cut Quartz as Determined by Electrical Response Measurements, *J.Phys.Chem. Solids*, **35**, pp. 355-372, 1974.

Gratz, A., Deformation in Laboratory-Shocked Quartz, *J.Non-Crystalline Solids*, **67**, pp.543-558, 1984.

Grimsditch, M., Polymorphism in Amorphous SiO_2, *Phys.Rev.Lett.*, **52**, pp. 2379-2381, 1984.

Hayes, D.B. and Graham, R.A., Yielding of Shock-Loaded X-Cut Quartz, *Bull.Amer.Phys.Soc.*, **23**, pp. 71, 1978.

Heinz, D.L., *Experimental Determination of the Melting Curve of Magnesium Silicate Perovskite at Lower Mantle Conditions, and its Geophysical Implications*, Ph.D. thesis, University of California, Berkeley, 76 pp., 1986

Hemley, R.J., Mao, H.K., Bell, P.M., and Mysen, B.O., Raman Spectroscopy of SiO_2 Glass at High Pressure, *Phys.Rev.Lett.*, **57**, pp. 747-750, 1986.

Jackson, I., and Ahrens,T.J.,Shock Wave Compression of Single-Crystal Forsterite, *J.Geoph.Res.*, **84**, pp. 3039-3048, 1979.

Jackson, I., Melting of the Silica Isotypes SiO_2, BeF_2, and GeO_2 at Elevated Pressures, *Phys.Earth.Planet.Int.*, **13**, pp. 218-231, 1976.

Jeanloz, R., and Richter, F.M., Convection, Composition and the Thermal State of the Lower Mantle, *J.Geoph.Res.*, **84**, pp. 5497-5504, 1979.

Jeanloz, R., and Thompson, A.B., Phase Transitions and Mantle Discontinuities, *Rev.Geoph.Space.Phys.*, **21**, pp.51-74, 1983.

Jones, O.E., and Graham, R.A., Shear Strength Effects on Phase Transition Pressures Determined from Shock-Compression Experiments, in *Accurate Characterization of the High Pressure Environment*, ed. Lloyd,E.C., Nat.Bur.Stand.(U.S.)Spec.Publ. **326**, pp. 229-237, 1971.

Kato, T., and Kumazawa, M., Melting and Phase Relations in the System Mg_2SiO_4–$MgSiO_3$ at 20 GPa under Hydrous Conditions, *J.Geoph.Res.*, **91**, pp. 9351-9355, 1986.

Kieffer, S.W., Shock Metamorphism of the Coconino Sandstone at Meteor Crater, Arizona, *J.Geoph.Res.*, **76**, pp. 5449-5473, 1971.

Kennedy, G.C. and Higgins, G.H., Melting Temperatures in the Earth's Mantle, *Tectonophysics*, **13**, pp. 221-232, 1972.

Kleeman, J.D. and Ahrens, T.J., Shock-Induced Transition of Quartz to Stishovite, *J.Geoph.Res.*, **78**, pp. 5954-5960, 1973.

Kondo, K. and Ahrens, T.J., Shock-induced Spectra of Fused Quartz, *J.Appl.Phys.*, **54**, pp. 4382-4385,1983.

Kondo, K., Satoshi, I., and Sawaoka, A., Nonlinear Pressure Dependence of the Elastic Moduli of Fused Quartz Up to 3 GPa, *J.Appl.Phys.*, **52**, pp. 2826-2831, 1981.

Kondo, K. and Ahrens, T.J., Heterogeneous Shock-Induced Thermal Radiation in Minerals, *Phys.Chem.Minerals*, **9**, pp. 173-181, 1983.

Kuskov, O.L. and Fabrichnaya, O.B., The SiO_2 Polymorphs: The Equations of State and Thermodynamic Properties of Phase Transformations, *Phys.Chem.Minerals*, **14**, pp. 58-66, 1987.

Lyzenga, G.A., and Ahrens, T.J., Shock Temperatures of SiO_2 and their Geophysical Implications, *J.Geoph.Res.*, **88**, pp. 2431-2444, 1983.

Lyzenga, G.A. and Ahrens, T.J., Shock Temperature Measurements in Mg_2SiO_4 and SiO_2 at High Pressures, *Geoph.Res.Lett.*, **7**, pp. 141-144, 1980.

MacKenzie, J.D., High Pressure Effects on Oxide Glasses: I: Densification in the Rigid State, *J.Am.Ceram.Soc.*, **46**, pp. 461-470, 1963.

Marsh, S.P., *LASL Shock Hugoniot Data*, University of California Press, Berkeley, 658 pp.,1980.

--

Mashimo, T., Nishii, K., Soma, T., and Sawaoka, A., Some Physical Properites of Amorphous SiO_2 Synthesized by Shock Compression of Alpha Quartz, *Phys.Chem.Minerals*, **5**, pp. 367-377, 1980.

McQueen, R.G., Fritz, J.N., and Marsh, S.P., On the Equation of State of Stishovite, *J.Geoph.Res.*, **68**, pp. 2319-2322, 1963.

Newton, R.C., Jayaraman, A., and Kennedy, G.C., The Fusion Curves of the Alkali Metals up to 50 Kbars, *J.Geoph.Res.*, **67**, pp. 2559-2556, 1963.

Podurets, M.A., Simakov, G.V., and Trunin, R.F., On the Phase Equilibrium in Shock-Compressed Quartz and the Kinetics of Phase Transitions, *Physics of the Solid Earth*, **12**, pp. 419-424, 1976.

Rigden, S.M., Ahrens, T.J., and Stolper, E.M., Shock Compression of Molten Silicate: Results for a Model Basaltic Composition, submitted *J.Geoph.Res.*, 1987.

Schaal, R.B. and Horz, F., Shocked Rutilated Quartz, *Abstract in EOS*, **58**, pp. 1180, 1977.

Schmitt, D.R., Svendsen, B., and Ahrens, T.J., Shock Induced Radiation from Minerals, in *Shock Waves in Condensed Matter*, Gupta, Y.M., ed, Plenum Publishing Corporation, pp. 261-265, 1986.

Schmitt, D.R. and Ahrens, T.J., Temperatures of Shock-Induced Shear Instabilities and Their Relationship to Fusion Curves, *Geoph.Res.Lett.*, **10**, pp. 1077-1080, 1983.

Stishov, S.M. and Popova, S.V., New Dense Polymorphic Modification of Silica, *Geokhimiya*, **10**, 837-839, 1961.

Stoffler, D., Deformation and Transformation of Rock-Forming Minerals by Natural and Experimental Shock Processes, I. Behavior of Minerals Under Shock Compression, *Fortschr.Miner.*, **49**, pp. 50-113, 1972.

Stofller, D., Coesite and Stishovite in Shocked Crystalline Rocks, *J.Geoph.Res.*, **76**, pp. 5474-5488, 1971.

Sugiura, H., Kondo, K., and Sawaoka, A., Shock Temperatures in Fused Silica Measured by Optical Technique, *J.Appl.Phys.*, **53**, pp. 4512-4514, 1982.

Sugiura, H., Kondo, K., and Sawaoka, A., Dynamic Response of Fused Quartz in the Permanent Densification Region, *J.Appl.Phys.*, **52**, pp. 3375-3382, 1981.

Svendsen, B., Bass, J.D., and Ahrens, T.J., Optical Radiation from Shock Compressed Interfaces, in *U.S. - Japan Research Seminar on High-Pressure Research*, January 13-17, Kahuku, Hawaii, 1986.

Trunin, R.F., Simakov, G.V., Podurets, M.A., Moiseyev, B.N., and Popov, L.V., Dynamic Compressibilty of Quartz and Quartzite at High Pressure, *Izv.Acad.Sci., USSR, Phys.Solid Earth*, Eng. Trans. **No. 1**, 1971.

Turcotte, D.L. and Schubert, S., *Geodynamics, Applications of Continuum Physics to Geological Problems*, John Wiley and Sons, pp. 450, 1982.

Urtiew, P.A. and Grover, R., Temperature Deposition caused by Shock Interactions with Material Interfaces, *J.Appl.Phys.*, **45**, pp. 140-145, 1974.

Wackerle, J., Shock-Wave Compression of Quartz, *J.Appl.Phys.*, **33**, pp. 922-937, 1962.

Weast, R.C., *CRC Handbook of Chemistry and Physics*, CRC Press, Cleveland, 1982.

Weertman, J., The Creep Strength of the Earth's Mantle, *Rev.Geoph.Space Phys.*, **8**, pp. 145-168, 1970.

Chapter 3.

SHOCK INDUCED MELTING AND MICROFAULTING IN SINGLE CRYSTAL NaCl

ABSTRACT

Radiative color temperatures were measured in single crystal sodium chloride under shock compression parallel to [100] over a pressure range from 20 to 35 GPa. Color temperatures from 2500 to 4500 K and emittances from 0.003 to 0.3 were determined by fitting observed spectra (450 to 850 nm) to the Planck greybody radiation law. These data support a heterogeneous shock deformation model of shocked halite in this pressure range. A 2500 K temperature rise ,of unknown origin, is observed over the B1-B2 mixed phase region from 25 to 30 GPa. Assuming that shock deformation occurs via yielding in localized planar zones which become melt and the melting temperature at high pressure controls the temperature, we infer that the temperature of the B2 fusion curve from 30 to 35 GPa rises from 3200 to 3300 K. The B1-B2-liquid triple point is predicted to be at a temperature of 2250 K and 23.5 GPa.

INTRODUCTION

Halite is an important mineral as it is the proving ground of solid state theory, especially the equation of state and the B1 (NaCl crystal structure) to B2 (CsCl crystal structure) solid phase transformation (e.g., Jeanloz (1982), Cohen and Gordon (1975), Hemley and Gordon (1985), Froyen and

Cohn (1993), and Bukowinski and Aidun (1985)). Theories of melting of NaCl, especially under pressure (reviewed by Stishov (1974)), are limited but suggest that melting in NaCl may be predicted from a first principles approach (Boyer (1980,1981)). High pressure experiments constrain these models and aid in their application to more complex molecular structures.

NaCl has been extensively studied under both static and dynamic loading conditions.

Early compression work on NaCl, summarized by Fritz et al., (1968), centered on reports of the B1-B2 phase transition occurring at a pressure of less than 3 GPa, the conclusive discovery at 30 GPa and 298 $^{\circ}K$ of this transition was finally reported in a paper by Bassett et al., (1968). Additional data on the B1-B2 transition and compression data for the B2 phase are reported in Liu and Bassett (1973), Sato-Sorenson (1983), Heinz and Jeanloz (1984), and Li and Jeanloz (1987). The latter mapped the NaCl B1-B2 phase line to 670 $^{\circ}K$.

High Pressure melting data for the B1 phase are reported by Clark (1959), Pistorius (1966) and Akella et al., (1969) to 6.5 GPa.

Shock wave pressure-volume measurements for material initially in the B1 phase are reported by Fritz et al., (1968), Alder (1963), Christian (1957), Al'tshuler et al., (1961), Kormer et al., (1965b) and Marsh (1980) (figure 1). The B1 to B2 phase transition is most notable in the plot of U_s vs U_p (Figure 1b). Although the Hugoniots for different crystal orientations are identical at lower pressures, shock waves propagating parallel to the [100] and [111] orientations initiate the B1-B2 phase transformation at 26.4 and 23.1 GPa (Alder (1963), Fritz et al., (1968)), respectively.

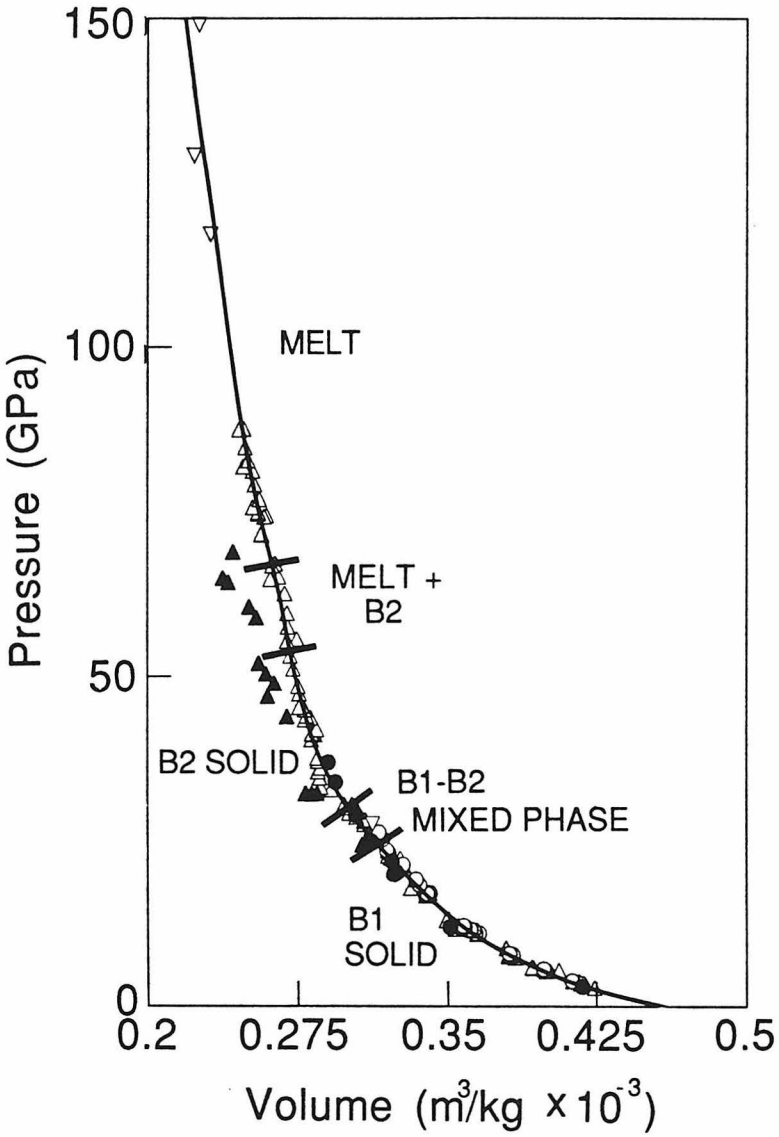

Figure 1) Hugoniot relations for NaCl. **1a)** Pressure- Volume Hugoniot of NaCl. Plot includes diamond cell measurements for the B1 phase of Sato-Sorenson (1983) (filled circles) and the B2 phase of Heinz and Jeanloz (1984) (filled triangles). Hugoniot data included are from Marsh (1980)(open triangles), Fritz et al., (1968)(open circles) for NaCl with shock propagation perpendicular to [100], and for randomly oriented crystals of Kormer et al.,(1965b) (open inverted triangles).

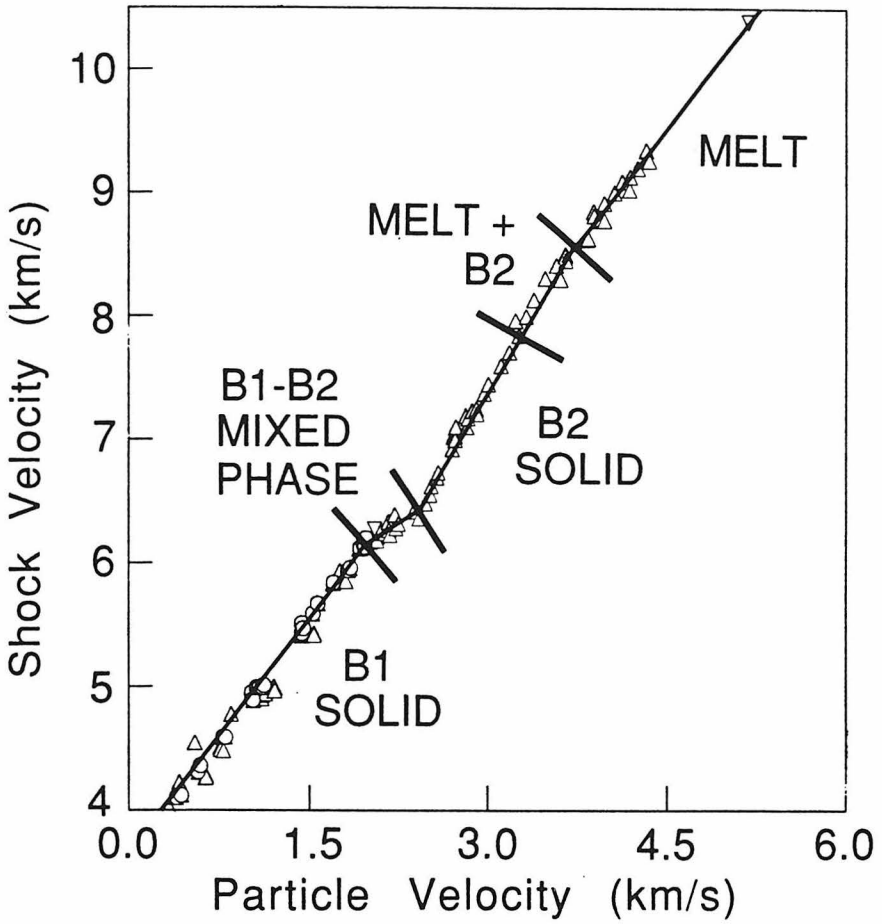

1b) Shock wave velocity vs material particle velocity Hugoniot data for NaCl, same symbol index as for 1a). B1-B2 phase transformation evident over the range of particle velocity of approximately 2.0 to 2.5 km/s. Homogeneous melting of NaCl under shock conditions evident by change in slope for particle velocities $>$ 3.5 km/s.

A pressure-volume relationship for a material is determined in most shock wave measurements; however, a full understanding of the equation of state requires knowledge of the temperature. Temperature measurements under shock compression are difficult given the short timescale of the experiments (usually less than 1 microsecond); optical pyrometry has been applied to the measurement of temperature in transparent minerals (Kormer et al., (1965a), Lyzenga and Ahrens (1980a), Lyzenga et al., (1983), Ahrens et al., (1982), Brannon et al., (1983), Brannon et al., (1984), Holmes et al., (1984), Radousky et al., (1985), Boslough et al., (1986), and Svendsen and Ahrens (1987)).

Recent interest has focused upon improving the spectral resolution of the light emitted during shock propagation through transparent crystals using multichannel optical analyzers (Sugiura et al., (1980), Kondo and Ahrens (1983), Kondo et al., (1983), Schmitt and Ahrens (1983), Hasegawa et al., (1984), and Schmitt et al., (1986)). To present, exploratory studies have included crystalline and fused SiO_2, NaCl, KCl, anorthite glass ($CaAl_2Si_2O_8$), periclase (MgO), gypsum ($CaSO_4.2H_2O$), calcite ($CaCO_3$), fluorite (CaF_2), and corundum (Al_2O_3). In general, the minerals known to undergo shock induced phase transformations displayed color temperatures higher ($>$ 1000 K) than those expected for a shocked continuum and low emittances suggestive of localized heterogeneous shock deformation referred to as shear banding (Grady (1980)) or microfaulting (Gratz (1984)). Low emittances roughly gauge the degree of heterogeneity within a sample (Kondo and Ahrens (1982)) and the observed radiative temperatures may yield high pressure fusion curves (Schmitt and Ahrens (1983)).

--

The exploratory studies above were not of sufficient resolution in pressure to make detailed inferences of the effects of shock pressure on shock temperatures in this pressure range. In the present study, the results of ten shock temperature experiments on NaCl over the pressure range of 20 to 35 GPa are reported. The present data shows that the temperatures are dependent upon the proximity in pressure of the shock compression to a phase transition region.

EXPERIMENTAL

Experimental details are discussed in Kondo and Ahrens (1983) and Schmitt et al., (1987). Briefly, planar shock waves are produced in NaCl samples by impact of Tungsten flyer plates, launched to velocities up to 2.5 km/s by a 40 mm powder gun, with metal driver plates. (figure 2). Thermal radiation is emitted by shock compressed NaCl sample; the radiation propagates through the unshocked sample portion and directed to a diffraction grating spectrometer, a photodiode, and a framing camera. The resulting spectrum is recorded by a intensified vidicon charge coupled detector (EG&G Princeton Applied Research PARC-1257) which counts photons as a function of wavelength. The vidicon is gated to integrate radiation only when the shock wave is near the sample center; gate durations are typically 300 ns to 500 ns. The photodiode provides a record of the intensity of the emitted light vs time and the framing camera obtains several images of the light emitting regions of the unmasked regions of the sample during the time the shock wave propagates through the sample.

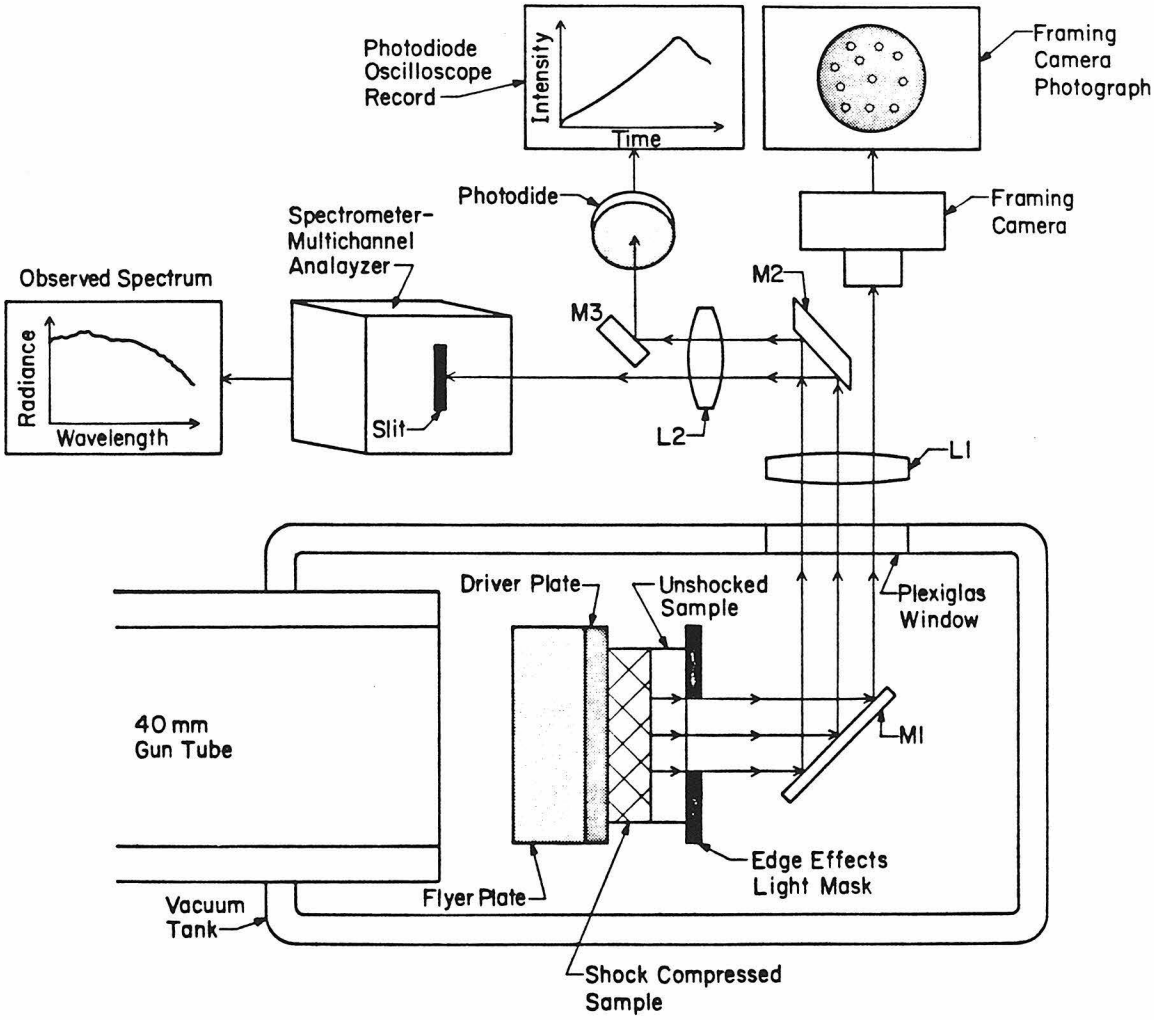

Figure 2) Schematic of experimental setup as shock wave propagates through sample after impact of flyer and driver. M1, M2, and M3 are front surface mirrors. L1 and L2 are focusing lenses.

NaCl samples (5mm thick by 25.4 mm diameter, Harshaw Chemical Co. and Janos Optical Co.) were obtained from large crystals separated along the excellent [100] NaCl cleavage. Bulk densities, determined by measurement of mass and sample dimensions (Table 1), agreed with the published halite single crystal value of 2165 kg/m^3 (Weast (1976)). Both faces of the sample were polished to an optical finish and had a flatness of 1/40 of a wavelength of 10.6 μm light. A silver layer ($\sim$ 3 A) was vacuum deposited on one face to reduce light emissions from the sample-driver interface (Kondo et al., (1983)). An opaque mask (2.54 cm diameter with a 1.25 cm circular hole) was mounted on the sample free surface to eliminate light originating near the sample edges.

Raw data consist of photon counts on each of the 500 vidicon target channels from 450 to 880 nm. The vidicon response was calibrated with a tungsten ribbon lamp (Optronics model #550) of calibrated spectral radiance under conditions (e.g., lamp position and vidicon delay and gate) identical to those of the actual experiment. For each channel, counts are converted to spectral radiances using the calibration response and the supplier provided lamp radiance by the formula:

$$(1)\quad R_i = C_i L_i / K_i$$

where i is the channel index, R_i is the determined experimental spectral radiance, C_i is the observed count, L_i is the standard spectral radiance of the lamp, and K_i is calibration lamp count for the experimental gate time. The resulting spectrum is assumed to be Planck greybody radiation defined by:

$$(2)\quad R(\lambda) = \frac{c_1 \epsilon}{\lambda^5 (exp\,(c_2/(\lambda T))-1)}$$

Table 1) Parameters for shock temperature measurements

Sample Number	Flyer Material	Flyer Velocity km/s	Driver Material	Sample[(a)] Density Mg/m^3	Pressure Pressure GPa	Color Temperature K	Emittance
612	W	2.26±0.03	Cu	2.14	30.2±0.9	4890±500	0.012±0.003
613	W	1.98±0.03	Al	2.14	25.1±0.5	3880±200	0.048±0.0048
641	W	2.42±0.05	W	2.15	28.4±0.8	2900±200	0.28±0.028
643	W	2.34±0.04	Cu	2.14	31.4±0.7	2570±200	0.19±0.019
645	W	2.39±0.04	W	2.15	28.0±0.7	3530±200	0.059±0.0059
646	W	1.98±0.04	W	2.14	21.7±0.5	2220±200	0.31±0.031
696	W	2.49±0.05	Mg	2.16	28.8±0.9	2850±200	0.084±0.0084
697	W	2.34±0.04	Mg	2.16	26.4±0.7	4000±200	0.0039±0.0004
698	W	2.16±0.03	Mg	2.16	23.8±0.5	2540±200	0.013±0.0013
699	W	2.48±0.05	Mg	2.16	33.9±1.0	2870±200	0.016±0.0016

(a) Uncertainty of density $\sim$ 1% primarily due to error in sample volume determination.

where R is the spectral radiance at wavelength λ, ϵ is the emittance assumed to be independent of wavelength, T is the temperature, and c_1 and c_2 are constants equal to $1.191 \times 10^{-16} Watts \cdot m^2/steradian$ and $1.438 \times 10^{-2} m \cdot {}^\circ K$, respectively. The Wien's law approximation of equation 2:

$$(3) \quad R(\lambda) = \frac{c_1 \epsilon}{\lambda^5 exp\,(c_2/(\lambda T))}$$

may be written as:

$$(4) \quad ln\,(c_1/(R\,\lambda^5)) = (c_2/\lambda)T^{-1} - ln\,(\epsilon)$$

to facilitate least squares (Bevington (1969)) determination of 1/T the slope, and $-ln\,(\epsilon)$ the intercept of the resulting linear function with $ln\,(c_1/(R\,\lambda^5))$ as the dependent variable, and (c_2/λ) as the independent variable. Although the formal least squares error is less than 50 $^\circ K$ for most experiments, a more conservative uncertainty of $\pm$ 200 $^\circ K$ is given for the radiant temperatures.

RESULTS

Based upon their shape, new spectra and those of Kondo and Ahrens (1982), Schmitt and Ahrens (1983), and Schmitt et al., (1986) are of a thermal nature (figure 3). Shots #641, #643, #645, and #646 (Janos Optical Co.) display a prominent line spectra centered near 750 nm superimposed upon greybody spectra. The effect may be due to impurities in these samples as no non thermal radiation was observed in the remainder of the samples. Shots #612 and #613 both have a low signal to noise ratio; for these shots the amount of light reaching the spectrometer was reduced to maximize light incident to the framing camera. Shot #612 has been eliminated from

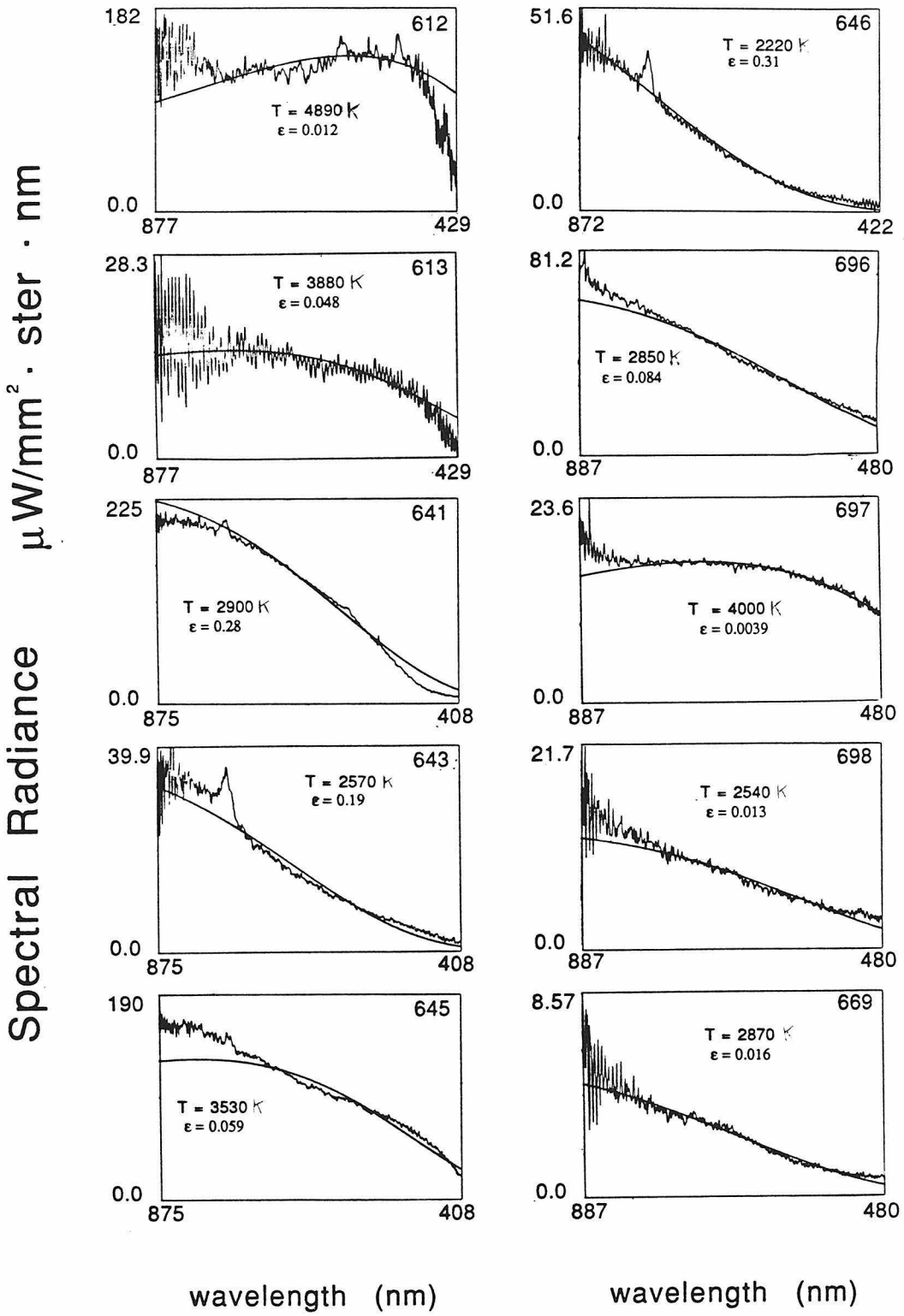

Figure 3) Observed greybody thermal spectra. Intensity in terms of spectral radiance plotted vs wavelength. Data recorded on 500 channels over optical spectral region, shot numbers (Table 1) shown in upper right corner of plots. Temperatures, in Kelvin, and emittances, ϵ, determined from these spectra using Planck greybody formula. Best fit curves are plotted through data.

consideration due to the poor greybody fit (equation 4) of the spectrum.

Available photodiode records are plotted as normalized intensity vs. time (figure 4), photodiode intensity is important to our interpretation of experimental results but is a qualitative measure only. We note here that the photodiode records for shots #612 and #613 have insufficient amplitude to accurately measure from the oscilloscope photographs and are not shown; however, in both cases the light levels increased linearly with time until the shock reached the sample free surface.

DISCUSSION

EVIDENCE FOR HETEROGENEOUS DEFORMATION IN CRYSTALLINE NaCl

Brittle materials undergoing heterogeneous deformation are usually thermal insulators characterized by a fluidlike release from high pressure and the existence of a high pressure phase transformation (Grady (1980)). Thermal energy is non-uniformly deposited in the localized zones which achieve temperatures much higher than predicted for the shock compressed continuum state. The low thermal conductivity allows maintenence of local high temperatures for the shock wave experiment duration as assumed in the models of Vineyard (1983), Svendsen and Ahrens (1986), and Grady and Kipp (1987).

In terms of shock induced shear deformation and heating, quartz is the most studied mineral and serves as an analog to NaCl. The loss of strength upon release from high pressure suggests that partial melting of quartz occurs in the shock front (Grady et al., (1975)). Shock recovered

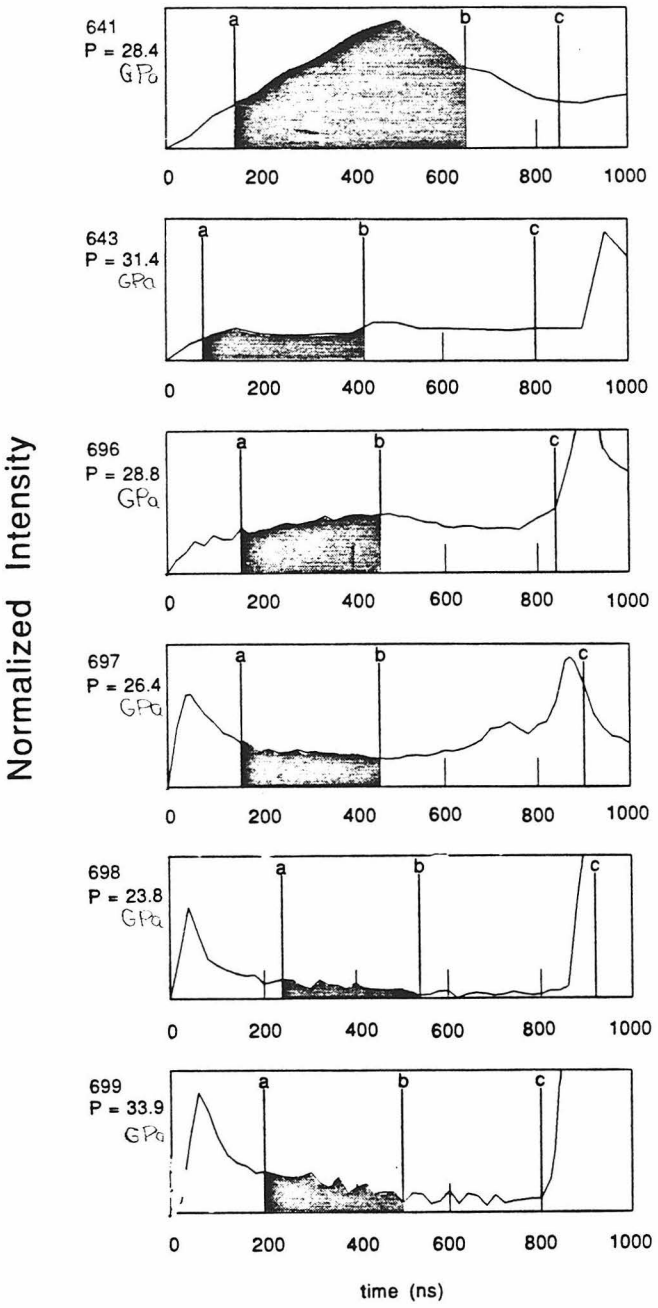

Figure 4) Photodiode records of intensity of emitted light vs time. Time t=0 is time of entry of shock wave into sample. Fiducials a,b, and c are at initiation of spectrometer photon accumulation, end of spectrometer accumulation, and first arrival of shock wave at free surface of sample, respectively. Filled region represents light integrated by spectrometer multichannel analyzer.

quartz displays glass-filled microfaults at approximately 45 ° to the shock front (Gratz (1984)) (figure 8a): the orientation of maximum shear stress (Jones and Graham (1968)). The majority of the shock compressed material remains relatively undamaged and experiences volumetric compression due to the pressure in the shock induced molten material which fills microfault zones (Anan'in et al., (1974)). Also, high pressure solid phase nucleates and grows on the time scale of the high pressure pulse (Ashworth and Schneider (1985)) (figure 8b). The temperature of melt-filled microfaults appears to be at the fusion temperature of the equilibrium solid phase due to the buffering effect of the latent heat of fusion (Schmitt and Ahrens (1983)).

The evidence for shear instability related, heterogeneous shock deformation in crystalline NaCl is not as well documented. However, irregular deformation features are observed in recovered natural and laboratory shocked NaCl. Shock metamorphism has been noted surrounding cavities formed by large chemical and nuclear explosions (Short (1961), Short (1968), Rawson (1963), Kahn et al., (1968)). Additionally, salt from regions near explosion cavity walls is stronger than common mine salt (Short (1968)), this effect could be a result of shock induced stiffening not unlike the observed shock fusion of individual fused silica plates (Wackerle (1962)).

Laue x-ray analysis of NaCl recovered from laboratory shock pressures $>$ 30 GPa (Braznik et al., (1969)) is indicative of a randomly oriented polycrystalline material suggesting recrystallization of both high and low pressure phases behind the shock front. The recrystallization could not

have been the result of total melting and rapid cooling as the continuum temperature of NaCl upon release from 30 GPa is only 390 $^{\circ}K$. The occurrance of heterogeneous deformation in the shock process in NaCl is thus not surprising considering that similar behavior of polycrystalline NaCl under static loading conditions near the phase transformation also occurs; the NaCl B1-B2 phase transformation has been mapped (Li and Jeanloz (1987)) by visual observation of the textural difference of the material within the diamond cell due to the combined presence of both B1 and B2 grains which have differing refractive index.

As in Kondo and Ahrens (1983a) and Schmitt et al., (1986), radiative temperatures $>$ 1000 $^{\circ}K$ higher than those expected for the NaCl continuum under compression and low emittances (Table 1, figures 6 and 7) are observed upon shock compression to stresses in the range of 20 to 35 GPa. This combination of emittances and temperatures are highly suggestive of a nonhomogeneous deformation in the NaCl; i.e., the temperatures are those encountered within the microfaults in the shock compressed crystal. NaCl radiates as a blackbody (ϵ=1) above 46 GPa (Kormer et al., (1965a), Ahrens et al., (1982)) which is in the Hugoniot B2 phase region (figure 1). In this regime deformation is believed to be homogeneous; therefore the emittance appears to be a gauge of the areal fraction of the material subjected to heterogeneous deformation.

The power radiated by by a Stefan-Boltzmann greybody proportional to T^4. The ratio of power radiated for two greybodies at 1000 $^{\circ}K$ and 2000 $^{\circ}K$ is thus 1:16; this ratio rapidly decreases as the relative temperatures rise. However, over the optical bandpass in these

experiments, the ratio of spectral radiances for a given temperature difference is more extreme; for example, the calculated spectral radiances (equation 2) at a wavelength of 600 nm for blackbodies with temperatures of 2000 and 3000 $^{\circ}K$ are 1.6×10^{5} and 8.7×10^{6} times the spectral radiance of a blackbody at 1000 $^{\circ}K$, respectively. Since the differential between observed and continuum temperatures is $>$ 1000 $^{\circ}K$, even with an ϵ near 0.001 the amount of radiation emitted by the shocked NaCl at the continuum temperature is within the noise level of the higher temperature signal from the localized zones of deformation.

Framing camera photographs were obtained from shot #645 at 28.0 GPa (figure 5). This NaCl sample emitted light in an irregular pattern of light and dark zones for both exposures and provides further evidence of a heterogeneous shock deformation of NaCl over the pressure range of these experiments. One large cool region near the sample center persists for the duration of the shock compression. The bright ring in the second exposure (lower photograph) is due to interaction of the sample with the aluminum mask upon shock wave arrival at the sample free surface.

The thermal diffussivity is defined by:

$$(5)\quad \kappa = k/\rho C_p$$

where κ is the thermal diffussivity, k is the thermal conductivity, ρ is the density, and C_p is the heat capacity. An important criterion for the production and persistence of melt, which may fill microfaults in a shock compressed material, is retention, on the time scale of the experiment, of energy deposited in shear related deformation features due to low thermal diffussivity: κ. NaCl is included in a compilation (Table 2, after Grady (1980))

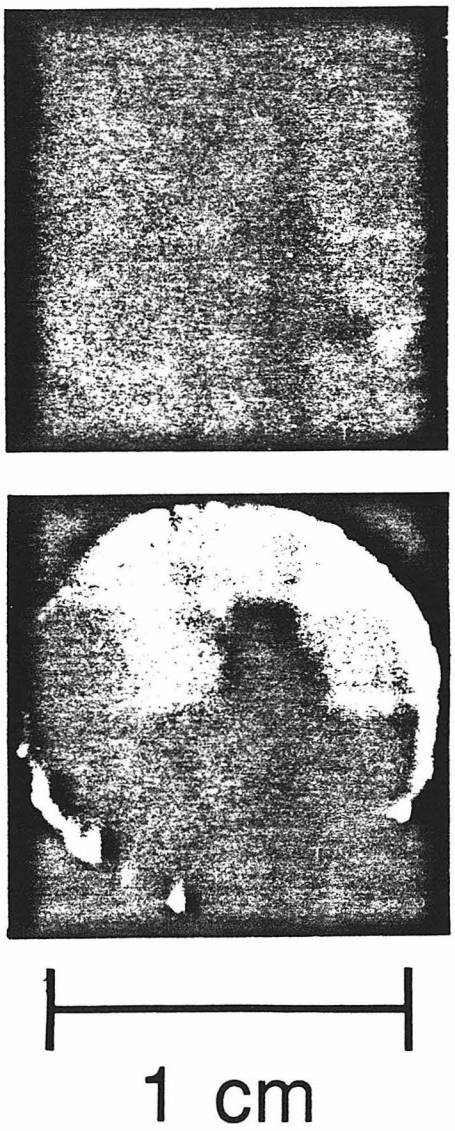

Figure 5) Framing camera images for shot #645, shock pressure = 28.0 GPa. Top image is 200 ns exposure initiated 100 ns after entry of shock wave into sample. Lower image of 500 ns duration initiated 100 ns after first exposure.

Table 2) Comparison of thermodynamic parameters for minerals

Material	k Thermal Conductivity $W/m\ ^\circ K$	C_p Heat Capacity $10^3 J/kg\ ^\circ K$	ρ Density Mg/m^3	κ Thermal Diffusivity $10^{-7} m^2/sec$	Melting Temperature $^\circ K$	Reference
SiO_2	2.5	0.8	2.63	12	1710	1
$CaCO_3$	2.5	0.84	2.70	11	1540	1
NaCl	5.6	0.85	2.16	31	1074	2
Al_2O_3	20.1	0.75	3.99	69.6	2350	1
MgO	33.5	0.88	3.65	104	3100	1

References) 1: Grady (1980), 2: thermal conductivity - Gray(1963), density and melting temperature - Weast(1977), heat capacity is assumed given by: $C_v = 3nR$ (Dulong-Petit high temperature approximation) where n is the number of ions of the molecular formula and R is the gas constant.

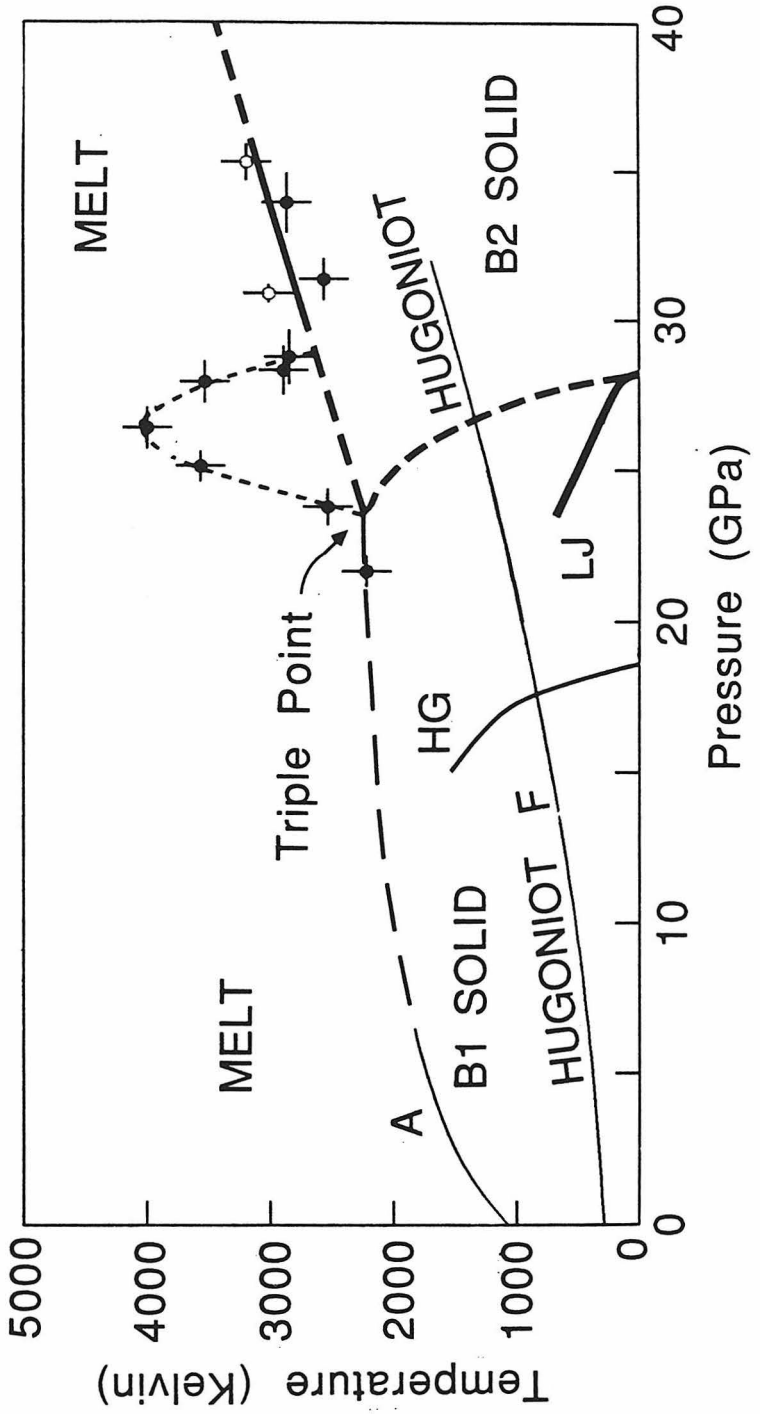

Figure 6). 6a) Plot of observed temperatures vs pressure for NaCl. Filled circles are from present study, open circles from Kondo and Ahrens (1983). (A) - Static melting data to 6.5 GPa (Akella et al., (1969)), (LJ) - diamond cell B1-B2 NaCl equilibrium phase line (Li and Jeanloz (1987)), (HG) - theoretical B1-B2 phase line (Hemley and Gordon (1984)), (F) - calculated Hugoniot continuum temperatures (Fritz et al.,(1968)).

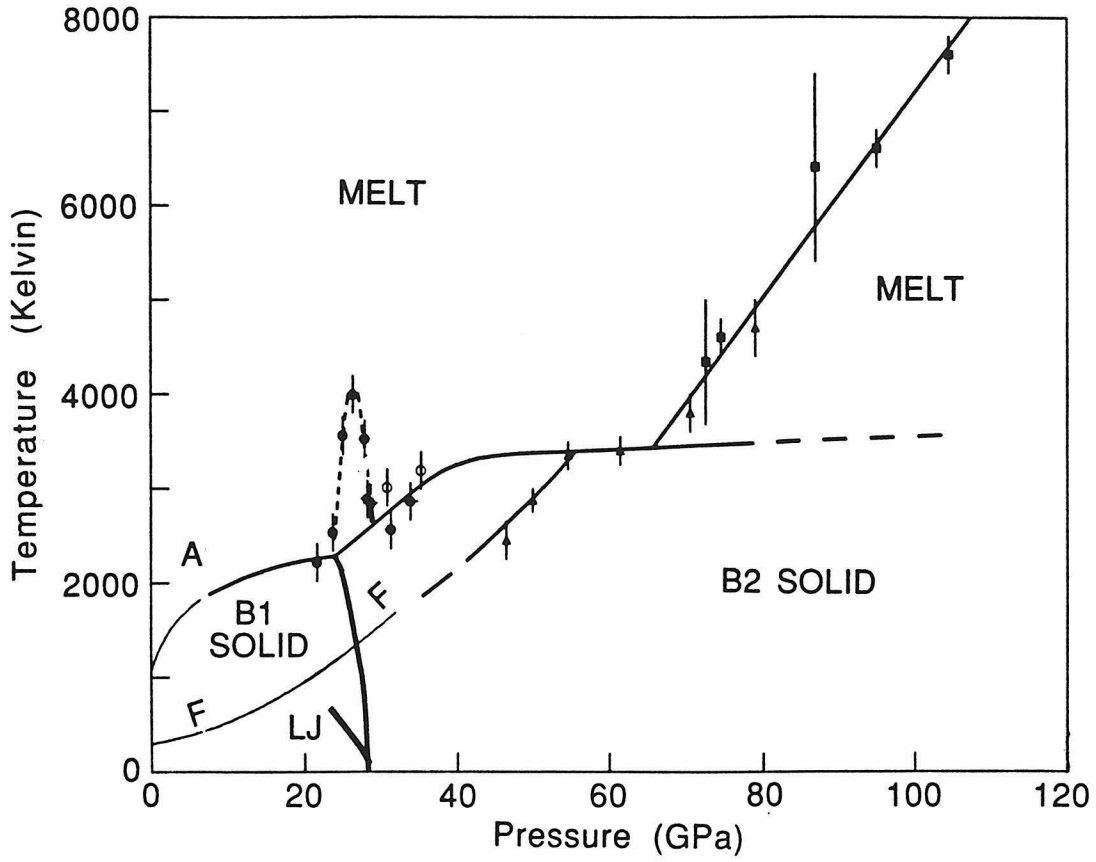

6b) Temperature vs pressure for NaCl including data of Kormer et al., (1965a)(filled triangles) and Ahrens et al., (1982)(filled squares). Data above 47 GPa are indicative of a homogeneous deformation, these are blackbody temperatures. Data above 60 GPa are within melt field.

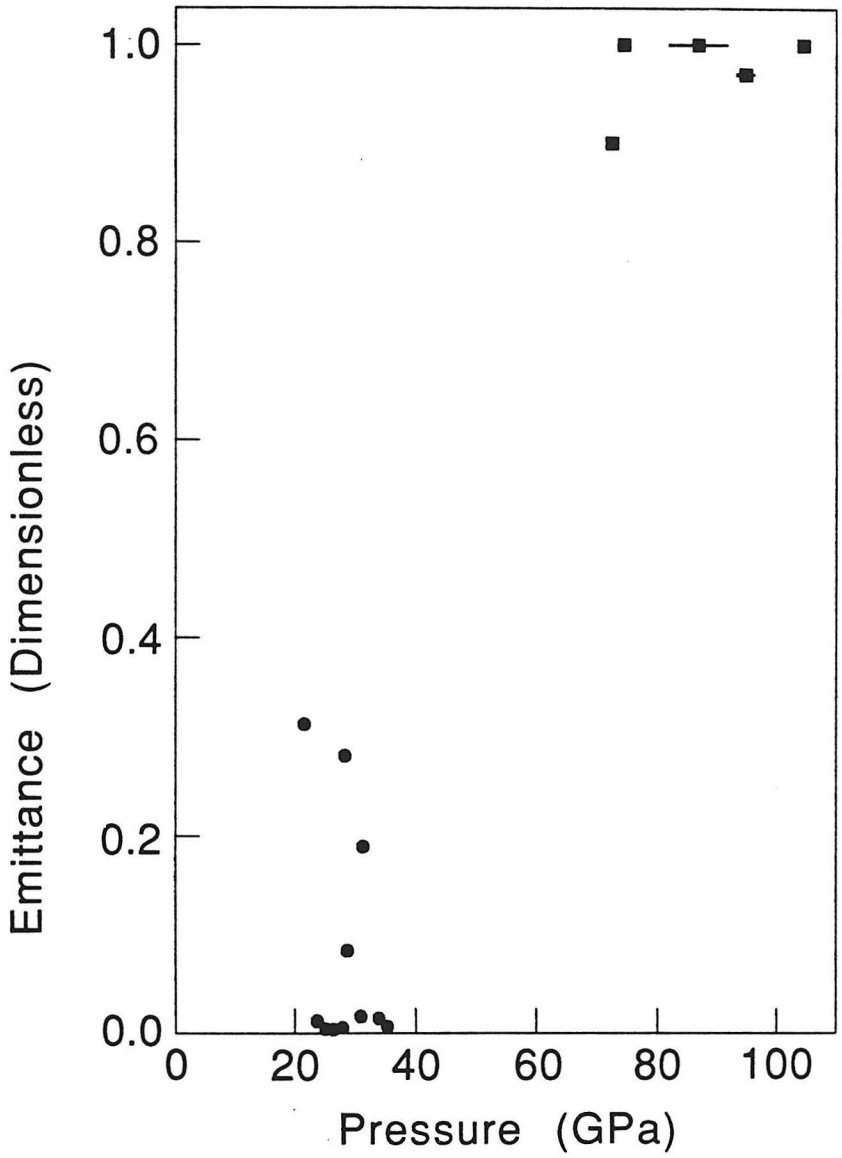

Figure 7) Greybody emittance vs pressure for NaCl. Filled circles present study and Kondo and Ahrens (1983a) in heterogeneous deformation range; filled squares are higher pressure results of Ahrens et al., (1982) in homogeneous deformation range.

of thermal properties of minerals known to undergo microfault melt production (SiO_2, $CaCO_3$) to those which retain shear strength upon release (Al_2O_3, MgO). The low melting temperature of NaCl may in part offset the effects of a κ which is higher than those of SiO_2 and $CaCO_3$, but noticeably smaller than those of Al_2O_3 and MgO, to allow production of microfaults accompanied by melting.

The nature of optical emissions from shocked crystals depend upon the amplitude of shock induced deformation occurring (Schmitt and Ahrens (1983), Schmitt et al., (1986)). For example, calcite displays a well defined thermal spectra upon shock loading. Periclase displays a wide line spectra centered at 700 nm believed to be due to microfracturing during compression, no thermal component is observed. Corundum emits a spectra intermediate to that of calcite and periclase which may be interpreted as the superposition of a broad line spectra upon a greybody. The spectra emitted from shocked fused quartz are thermal. Shocked crystalline quartz is a more complex possibly due to its piezeoelectric properties. Light which is primarily thermal in its spectrum is emitted by NaCl. When compared to the spectra and differing shock deformation in other minerals it appears that shock deformation in NaCl is also heterogeneous and accompanied by the production of melt-filled microfaults.

In summary, the above results are suggestive of a heterogeneous deformation process in NaCl characterized by the production of melt-filed microfaults behind the shock front, interpretation of the results of this study are based on the deformation model sketched in figure 8.

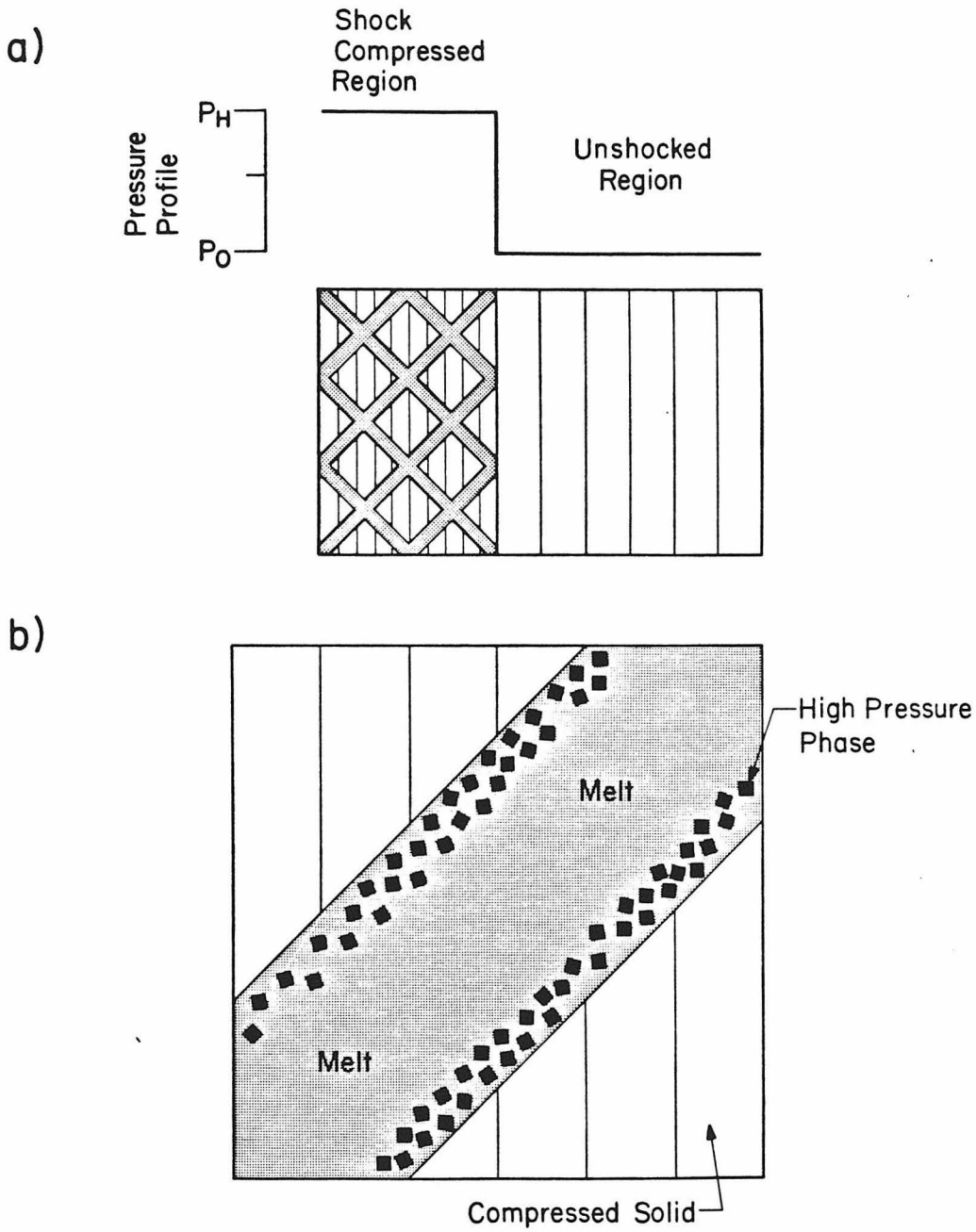

Figure 8) Schematic diagram of inferred microfaulting in NaCl under shock compression. **8a)** View of the production of microfaults at an orientation of 45° to the direction of shock wave propagation along the planes of maximum shear stress in the material. **8b)** Magnified view of microfault filled with melt and with nucleation of high pressure phase.

INFERRED PHASE RELATIONS OF NACL

The present data (figure 6) display a marked rise in temperature above 25 GPa with a maximum near 27 GPa followed by a decrease to 30 GPa; this pressure range coincides with the B1-B2 mixed phase region along the Hugoniot of [100] NaCl (Ahrens et al (1982), see also figure 1). The response of KCl over the B1-B2 phase transition region suggests that after partial transformation immediately behind the shock front, the material is quenched in a metastable state which approaches equilibrium at a rate dependent upon the intial crystal orientation (Hayes (1974)). Since KCl is a good structural and chemical analog to NaCl (Jamieson (1965)), these results suggest the high shock temperatures from 25 to 30 GPa may be related to this metastability over the NaCl Hugoniot mixed phase region. Although the reason for the increased temperatures is not understood, the results for NaCl suggest the high shock temperatures from 25 to 30 GPa may be related to superheating of either melt in microfaults or in the mixed phase solids. Similar behavior is observed in shocked fused quartz in the shock pressure region of 9.8 to 16 GPa which co-incides with the onset of the quartz to stishovite transformation (see chapter 2).

The anomalous photodiode record from shot #641 (figure 4) at 28.4 ($\pm$ 0.8) GPa may place an upper pressure limit to the mixed phase region. Intensity linearly increases with time to 500 ns after entry of the shock wave in the sample whereupon a peak is reached and intensity decays. The proximity in pressure of shot #641 and the end of the mixed phase region of NaCl is more than coincidental. The peculiar photodiode record may display characteristics from both the mixed phase and the B2 region of the NaCl

Hugoniot. Irregular behavior of emissions from shocked materials near Hugoniot phase boundaries are not unknown; for example, Lyzenga et al., (1983) recorded a fluctuating intensity in a photodiode record from fused quartz shocked to 73.3 GPa: the inferred homogeneous melting pressure of shock formed stishovite.

Based upon the above model of the heterogeneous shock deformation (figure 8) believed to dominate in NaCl over the pressure range studied, the observed radiative temperatures above 30 GPa represent the melting temperature of the high pressure B2 phase of NaCl (figure 6). From this assumption, the B2 melting curve is drawn through the four data points above 30 GPa and is consistent with earlier NaCl shock temperature determinations (Kormer et al., (1965a), and Ahrens et al., (1982), figure 6b). In contrast to the greybody temperatures, indicative of the melting only in localized regions, found in this study, the earlier data are blackbody temperatures indicating homogeneous shock deformation at higher pressures above 55 GPa. The shock temperatures above 55 GPa thus represent the equilibrium continuum temperature. The relative flatness of the slope of the data between 55 GPa and 70 GPa is due to the latent heat of fusion and the shape of the curve is as expected for a homogeneous melting transition (Duvall and Graham (1977)), recently, similar results have been observed in CsI (Radousky et al., (1985)). Increasing temperatures above 70 GPa are those of the equilibrium temperature with shock pressure of NaCl melt. The present four data points above 30 GPa, if assumed to represent the melting curve of the B2 NaCl phase, yield a local Clapeyron line with slope $dT_m/dP = 72$ K/GPa (figure 6).

For shot #646 at 21.7 GPa, the observed temperature may define a point on the untransformed B1 melting curve since the experimental pressure was below the onset ot the B1-B2 shock transition for any initial NaCl crystal orientation. This result is consistent with an extrapolation of static melting determinations from 6.5 GPa (Akella et al., (1969)). The phase state of the next highest pressure shot (#698) at 23.8 GPa is more ambiguous; upon consideration of uncertainties in the exact B1-B2 transformation onset pressure, this datum has been included in the metastability region of the NaCl Hugoniot. As noted above for KCl (Hayes (1974)), the region of metastability commmences immediately past the onset of the B1-B2 phase transition; we therefore predict that the B1-B2-melt triple point lies in pressure below the data point of shot #698 near 2250 K and 23.5 GPa. The shape of the inferred phase lines near the triple point are similar to that determined for KCl (Clark (1959)) with an initial increase in slope of the B2-melt phase line.

An inferred B1-B2 solid equilibrium transition line is extrapolated from the predicted triple point to the room temperature static equilibrium measurement (Li and Jeanloz (1987)). Theoretical (Hemley and Gordon (1985) and diamond cell experimental results for NaCl (Li and Jeanloz (1987)) indicate that this phase line has a negative Clapeyron slope with increasing curvature at lower pressures (figure 6). The present inferred triple point and equilibrium B1-B2 phase line lie at higher pressures than would be suggested by extrapolation of the diamond cell equilibrium data (Li and Jeanloz (1987)).

CONCLUSIONS

1) Additional new optical observation of the shock induced optical spectra and framing camera images provide strong evidence for the heterogeneous deformation of single crystal NaCl in the dynamic pressure range of 20 to 35 GPa. Present observations include: a) greybody thermal spectra emitted by the samples during shock compression are fit to color temperatures in excess of the continuum temperature by at least 1000 $^{\circ}K$. This and low values of emittances of 0.3 indicate that zones of localized deformation (microfaults, shear bands) are produced. In analogy with results for SiO_2 we presume melting is occurring in these regions, b) The heterogeneous radiative pattern seen in framing camera photographs. Other arguments (e.g., irregular features in shock recovered NaCl) support the present evidence for heterogeneous deformation.

2) These microfault temperatures display a marked increase and subsequent decrease over the pressure range of 25 to 30 GPa. This pressure range corresponds exactly to the B1-B2 mixed phase region along the Hugoniot of NaCl. These anomalous temperatures are not understood but may be due to superheated microfault melt or mixed phase solid in this regime.

3) Based upon a model of heterogeneous shock compression characterized by the production of hot localized zones of melt (microfaults) in which nucleation of a high pressure phase would be enhanced, the observed temperatures above 30 GPa appear to follow the fusion curve of the B2 phase of NaCl. On this basis, the B1-B2-melt triple point is predicted to be near 2250 $^{\circ}K$ and 23.5 GPa.

REFERENCES

Ahrens, T.J., Lyzenga, G.A., and Mitchell, A.C., Temperatures Induced by Shock Waves in Minerals: Applications to Geophysics, in *Advances in Earth and Planetary Sciences, Volume* **12**, *High Pressure Research in Geophysics*, eds. Akimoto, S. and Manghnani, M.H., pp. 579-594, 1982.

Akella, J, Vaidya, S.N., and Kennedy, G.C., Melting of Sodium Chloride at Pressures to 65 Kbar, *Phys.Rev.*, **185**, pp. 1135-1140, 1969.

Alder, B.J., Physics Experiments with Strong Pressure Pulses, in *Solids Under Pressure*, eds. Paul, W. and Warschauer, D.M., McGraw-Hill, pp. 385-420, 1963.

Al'tshuler, L.V., Kuleshova, L.V., and Pavlosvskii, M.N., The Dynamic Compressibility, Equation of State, and Electrical Conductivity of Sodium Chloride at High Pressures, *Soviet Physics J.E.T.P.*, **12**, pp. 10-15, 1961.

Anan'in, A.V., Breusov, O.N., Dremin, A.N., Pershin, S.V., and Tatsii, V.F., The Effect of Shock Waves on Silicon Dioxide. I. Quartz, *Combust.Explos.Shock Waves*, **10**, pp. 372-379, 1974.

Bassett, W.A., Takahashi, T., Mao, H.K., and Weaver, J.S., Pressure- Induced Phase Transformation in NaCl, *J.Appl.Phys.*, **39**, pp. 319-325, 1968.

Bevington, P.R., *Data Reduction and Error Analysis for the Physical Sciences,* McGraw-Hill, New York, pp. 336, 1969.

Boslough, M.B., Ahrens, T.J.,and Mitchell, A.C., Shock Temperatures in Anorthite Glass, *Geophys.J.R.astr.Soc.*, **84**, pp. 475-489, 1986.

Boslough, M.B., *Shock Wave Properties and High Pressure Equations of State of Geophysically Important Materials*, Ph.D. thesis, California Institute of Technology, 171 pp., 1984.

Boyer, L.L., First-Principles Equation of State Calulations for Alkali Halides, *Phys.Rev.B Condens. Matter*, **23**, pp. 3673-3685, 1981.

Boyer, L.L., Nature of Melting and Superionicity in Alkali and Alkaline-Earth Halides, *Phys.Rev.Lett.*, **45**, pp. 1858-1862, 1980.

Brannon, P.J., Morris, R.W., and Asay, J.R., Shock-induced Luminescence from Z-cut Lithium Niobate, *J.Appl.Phys.*, **57**, pp. 1676-1679, 1984.

Brannon, P.J., Konrad, C., Morris, R.W., Jones, E.D., and Asay, J.R., Studies of the Spectral and Spatial Characteristic of Shock- induced Luminescence from X-cut Quartz, *J.Appl.Phys.*, **54**, pp. 6374-6381, 1983.

Brazhnik, M.I., Al'tshuler, L.V., and Tarasova, L.A., Phase Transformations in Shock-Compressed Rock Salt, *Combust. Explos. Shock Waves*, **5**, pp. 352-355, 1969.

Bukowinski, M.S.T., and Aidun, J., First Principles Versus Spherical Ion Models of the B1 and B2 Phases of NaCl, *J.Geoph.Res.*, **90**, pp. 1794-1800, 1985.

Clark, S.P., Effect of Pressure on the Melting Points of Eight Alkali Halides, *J.Chem.Phys.*, **31**, pp. 1526-1531, 1959.

Christian, R.H., *The Equation of State of the Alkali Halides at High Pressure*, Ph.D. thesis, University of California, 89 p., 1957.

Cohen, A.J., and Gordon, R.G., Theory of the Lattice Energy, Equilibrium Structure, Elastic Constants, and Pressure-Induced Phase Transitions in Alkali-Halide Crystals, *Phys.Rev. B*, **12**, pp. 3228-3241, 1975.

Duvall, G.E., and Graham, R.A., Phase Transitions Under Shock Wave Loading, *Rev.Mod.Phys.*, **49**, pp. 523-579, 1977.

Fritz, J.N., Marsh, S.P., Carter, W.J., and McQueen, R.G., The Hugoniot Equation of State of Sodium Chloride in the Sodium Chloride Structure, in *Accurate Characterization of the High Pressure Environment*, ed. Lloyd, E.C., Nat.Bur.Stand.(U.S.), Spec.Publ. **326**, pp. 201-208, 1968.

Froyen, S., and Cohen, M.L., Structural Properties of NaCl, *Phys.Rev.B Condens.Matter*, **29**, pp. 3770-3772, 1984.

Grady, D.E. and Kipp, M.E., The Growth of Unstable Thermoplastic Shear with Application to Steady-Wave Shock Compression in Solids, *J.Mech.Phys.Solids*, **35**, pp. 95-118, 1987.

Grady, D.E., Shock Deformation of Brittle Solids, *J.Geoph.Res*, **85**, pp. 913-924, 1980.

Grady, D.E., Murri, W.J., and DeCarli, P.S., Hugoniot Sound Velocities and Phase Transformations in Two Silicates, *J.Geoph.Res.*, **80**, pp. 4857-4861, 1975.

Gratz, A., Deformation in Laboratory Shocked Quartz, *J.Non-Crys. Solids*, **67**, pp. 543-558, 1984.

Gray, D.E., *American Institute of Physics Handbook*, American Institute of Physics, Mc-Graw-Hill, pp. 2200, 1963.

Hayes, D.B., Polymorphic Phase Transformation Rates in Shock- Loaded Potassium Chloride, *J.Appl.Phys.*, **45**, pp. 1208- 1217, 1974.

Heinz, D.L. and Jeanloz, R., Compression of the B2 High-Pressure Phase of NaCl, *Phys.Rev.B.*, **30**, pp. 6045-5050, 1984.

Hemley, R.J. and Gordon, R.G., Theoretical Study of Solid NaF and NaCl at High Pressures and Temperatures, *J.Geoph.Res.*, **90**, pp. 7803-7813, 1985.

Holmes, N.C., Radousky, H.B., Moss, M.J., Nellis, W.J., and Henning, S., Silica at Ultrahigh Temperature and Expanded Volume, *Appl.Phys.Lett.*, **45**, pp. 626-628, 1984.

Jamieson, J.C., Structural Transitions in Solids at High Pressures, in *Physics of Solids at High Pressures*, eds. Tomizuka, C.T. and Emirck, R.M., Academic Press, New York, pp. 444-459, 1965.

Jeanloz, R., Coexistence Curves and Equilibrium Boundaries for High-Pressure Phase Transformations, Submitted *J.Geoph.Res.*, 1987.

Jeanloz, R., Mineral and Melt Physics, A Summary of Research in the United States, 1979-1982, *Rev.Geoph.Space.Phys*, **21**, pp. 1487-1503, 1983.

Jones, O.E. and Graham, R.A., Shear Strength Effects on Phase Transition 'Pressures' Determined from Shock-Compression Experiments, in *Accurate Characterization of the High Pressure Environment*, ed. Lloyd, E.C., Nat.Bur.Stand.(U.S.), Spec.Publ. **326**, pp. 229-242, 1968.

Kahn, J.S., Nichols, M.C., and Taylor, R.W., Observations on the Energy Distribution and the Chemical, Petrographic, and Mineralogical Effects of Underground Explosions, in *Shock Metamorphism in Natural Materials*, eds. French, B.M. and Short, N.M., Mono Book Corp, Baltimore, page 625, 1968.

Kondo, K., and Ahrens, T.J., Heterogeneous Shock Induced Thermal Radiation in Minerals, *Phys.Chem.Minerals*, **9**, pp. 173-181, 1983.

Kondo, K., Ahrens, T.J., and Sawaoka, A., Shock-induced Radiation Spectra of Fused Quartz, *J.Appl.Phys.*, **54**, pp. 4382-4385, 1983.

Kormer, S.B., Sinitsyn, M.V., Kirillov, G.A., and Urlin, V.D., Experimental Determination of Temperatures in Shock-Compressed NaCl and KCl and of their Melting Curves at Pressures up to 700 Kbar,

J.Exptl.Theoret.Phys.(U.S.S.R.), **48**, pp.1033-1049, translation, *Soviet Phys. J.E.T.P.*, **21**, pp.689-700], 1965a.

Kormer, S.B., Sinitsyn, M.V., Funtikov, A.I., Urlin, V.D., and Blinov, A.V., Investigation of the Compressibility of Five Ionic Compounds at Pressures up to 5 Mbar, *J.Exptl.Theoret. Phys. (U.S.S.R.), 47, pp. 1202-1213, translation, Sov.Phys. J.E.T.P.*, **20**, pp. 811-819, 1965b.

Li, X., and Jeanoloz, R., Measurement of the B1-B2 Transition Pressure in NaCl at High Temperatures, Submitted to *Phys.Rev.B*, 1987.

Liu, L., and Bassett, W.A., Compression of Ag and Phase Transformation of NaCl, *J.Appl.Phys.*, **44**, pp.1475-1479, 1973.

Lyzenga, G.A., Ahrens, T.J., and Mitchell, A.C., Shock Temperatures of SiO_2 and Their Geophysical Implications, *J.Geoph.Res.*, **88**, pp. 2431-2443, 1983.

Lyzenga, G.A., and Ahrens, T.J., Shock Temperature Measurements in Mg_2SiO_4 and SiO_2 at High Pressures, *Geoph.Res.Lett.*, **7**, pp. 141-144, 1980a.

Lyzenga, G.A., *Shock Temperatures of Materials: Experiments and Applications to the High Pressure Equation of State*, Ph.D. thesis, California Institute of Technology, 208 pp., 1980b.

Marsh, S.P, *LASL Shock Hugoniot Data*, University of California Press, Berkeley, 658 pp., 1980.

Nakagiri, N. and Nomura, M., Theoretical Study of Hysteresis Phenomena of Pressure-Induced Polymorphic Transition in Alkali Halides, *J.Phys.Soc.Japan*, **51**, pp. 2412-2418, 1982.

Pistorius, C.W.F.T., Effect of Pressure on the Melting Points of the Sodium Halides, *J.Chem.Phys.*, **45**, pp. 3513-3519, 1966.

Radousky, H.B., Ross, M., Mitchell, A.C., and Nellis, W.J., Shock Temperatures and Melting in CsI, *Phys.Rev.B*, **31**, pp. 1457- 1462, 1985.

Rawson, D.E., Review and Summary of Some Project Gnome Results, *Trans.Am.Geoph.Union*, **44**, pp. 129-135, 1963.

Sato-Sorenson, Y., Phase Transitions and Equations of State for the Sodium Halides: NaF,NaCl,NaBr, and NaI, *J.Geoph.Res.*, **88**, pp. 3543-3548, 1983.

--

Schmitt, D.R., and Ahrens, T.J., Shock Temperatures in Fused Silica: Relation to Solid Phase State and Melting, *in preparation*, 1987.

Schmitt, D.R., Svendsen, B.,and Ahrens, T.J., Shock Induced Radiation from Minerals, in *Shock Waves in Condensed Matter*, ed. Gupta,Y.M., pp. 261-265, 1986.

Schmitt, D.R. and Ahrens, T.J., Temperatures of Shock Induced Shear Instabilities and Their Relationship to Fusion Curves, *Geoph.Res.Lett.*, **10**, pp. 1077-1080, 1983.

Short, N.M., Nuclear-Explosion-Induced Microdeformation of Rocks: An Aid to the Recognition of Meteorite Impact Structures, in *Shock Metamorphism in Natural Materials*, eds. B.M. French and N.M. Short, pp. 185-210, 1968.

Short, N.M., Fracturing of Rock Salt by a Contained High Explosive, *Colo.Sch.Mines Quart.*, **56**, pp. 221-258, 1961.

Sugiura, H., Kondo, K., and Sawaoka, A., Shock Temperatures in Fused Silica Measured by Optical Technique, *J.Appl.Phys.*, **52** pp. 4512-4514, 1982.

Stishov, S.M., The Thermodynamics of Melting of Simple Substances, *Sov.Phys.-Usp.*, **17**, pp. 625-643, 1975.

Svendsen, B., and Ahrens, T.J., Shock-induced Temperatures of MgO, in press, *Geoph.J.Roy.astr.Soc.*, 1987.

Svendsen, B., and Ahrens, T.J., Thermal History of Shock-Compressed Solids, in *Shock Waves in Condensed Matter*, ed. Gupta,Y.M., pp. 607-611, 1986.

Wackerle, J., Shock Wave Compression of Quartz, *J.Appl.Phys.*, **33**, pp. 922-937, 1962.

Weast, R.C., *Handbook of Chemistry and Physics, 57th Edition*, CRC Press, Cleveland, 1977.

Wallat, R.J., and Holder, J., The Born Model and the Effects of Hydrostatic and Non-Hydrostatic Stresses on Rubidium Halide Structural Phase Transitions, *J.Phys.Chem.Solids*, **39**, pp. 1147-1156, 1978.